
THE UNIVERSITY of ADELAIDE

# Design of g-$C_3N_4$ Based Electrocatalysts for $CO_2$ Reduction to Ethylene by Molecular Modelling

**By Sijia Fu**

School of Chemical Engineering and Advanced Materials

Faculty of Engineering, Computer and Mathematical Science

A Thesis submitted for the degree of Master of Philosophy

The University of Adelaide

Jun 2021

# Table of Contents

## Abstract

Developing efficient and clean energy conversion technologies is of great importance for the sustainability of society. The atmospheric $CO_2$ concentration has risen rapidly due to the increase of human activities and energy consumption, causing serious climate problems. $CO_2$ conversion is regarded as an effective method to mitigate the energy crisis and alleviate the dependence on fossil fuels. Electrochemical $CO_2$ reduction reaction ($CO_2RR$), with water as a hydrogen source, has attracted growing attention recently as it can help achieve anthropogenic carbon cycle and store renewable electricity (from solar, wind, geothermal, hydro, etc.). $C_2$ products are regarded as more preferable than $C_1$ due to their high energy density. However, the generation of $C_2$ generally suffers from high overpotential, low reaction rate, and low selectivity because the C-C bond formation is challenging. Therefore, developing proper electrocatalyst materials for $CO_2$ reduction to $C_2$ products with high activity, selectivity, and durability is significant. Single atom catalysts (SACs) have shown great ability in obtaining $C_1$ products attributing to the high utilization rate of metal atoms as active centers. However, their performance in producing $C_2$ is not satisfactory due to the limitation of one active site. Recently, a Cu-SAC supported on graphitic carbon nitride (g-$C_3N_4$) was detected to generate ethylene, but the complicated reaction networks were not systematically studied. This thesis aims to reveal the possibility to obtain $C_2H_4$ on the surface of metal supported on g-$C_3N_4$ (M-$C_3N_4$), and the underlying reaction mechanisms of $C_2H_4$ formation.

Chapter 1 is the introduction and Chapter 2 presents a literature review. The advances and challenges of $CO_2RR$ are summarized. Then the application of Cu and other SACs in $CO_2RR$ is studied and presented. Chapter 3 focuses on the understanding of mechanisms of $CO_2$ reduction to $C_2H_4$ on the asymmetric framework Cu-$C_3N_4$. 17 reaction pathways and three active sites (Cu, C, and N) are explored to present the whole reaction networks. The synergetic effect of dual sites is extensively studied through analysing the reaction networks. The results

show that Cu and C working as active sites has a better performance than Cu and N. This is because the carbon atom provides a settling center for the first $CO_2$ after reduction by Cu, and leaves Cu vacant for the second $CO_2$ reduction. Chapter 4 extends the study to other metal supported on g-$C_3N_4$, and verifies the reaction mechanisms established based on Cu-$C_3N_4$. 14 metal centres are considered in total. Through using the adsorption energies of CO* on the metal site and that of H* on the nitrogen site, seven metal centres among them are predicted to generate $C_2$ products. The $CO_2$ reduction performance is explored theoretically by analysing the reaction pathways to ethylene through the metal and nitrogen sites (M/N) or the metal and carbon sites (M/C). Moreover, a dual volcano-shaped plot is formed by the CO adsorption energies on metal sites to describe the synergistic effect of dual site. The conclusions are drawn in Chapter 5, following the discussions of challenges and perspectives of M-$C_3N_4$. The novel g-$C_3N_4$ based single atom catalyst provides a new platform for $CO_2$RR. By providing one metal site and another active site from g-$C_3N_4$, $CO_2$RR reduction to $C_2$ products become possible. The insightful reaction mechanisms can serve as a reference for designing more electrocatalysts with dual active sites.

# Declaration

I certify that this work contains no material which has been accepted for the award of any other degree or diploma in my name, in any university or other tertiary institution and, to the best of my knowledge and belief, contains no material previously published or written by another person, except where due reference has been made in the text. In addition, I certify that no part of this work will, in the future, be used in a submission in my name, for any other degree or diploma in any university or other tertiary institution without the prior approval of the University of Adelaide and where applicable, any partner institution responsible for the joint-award of this degree.

I acknowledge that copyright of published works contained within this thesis resides with the copyright holder(s) of those works.

I also give permission for the digital version of my thesis to be made available on the web, via the University's digital research repository, the Library Search and also through web search engines, unless permission has been granted by the University to restrict access for a period of time.

Name of Candidate: Sijia Fu

Signature:

Date: 21/Jun/2021

## Acknowledgments

This thesis would not have come to fruition without the support and help from my supervisors, friends, and families. Here, I would like to express my gratitude to them all.

First, I would like to thank my principle supervisor, Dr. Yan Jiao, for providing me with professional suggestions and support for my research. I stepped into the research field under her patient, generous, and careful guidance. Throughout my MPhil research, I was enlightened by her cautious attitude and enthusiasm. Without her attentive guidance and full support, I would not get these achievements. Moreover, I sincerely appreciate my co-supervisor, Dr. Jinrun Ran, for his continuous encouragement and guidance.

I would also like to thank Prof. Shizhang Qiao, Xin Liu, Xing Zhi, and Ling Chen for their inspiring discussions and generous help.

I would also like to acknowledge the Australian Government, The University of Adelaide for their support.

Finally, I would express my heartfelt appreciation to my family, my parents Xiaoguang Fu and Yuzhen Wang for their forever love and support. Without their unconditional trust and support, I could not have completed my MPhil research. It would be a great pleasure to dedicate this thesis to my family. And also, my sincere gratitude goes to my dear friends in China and Australia for their support.

# Chapter 1: Introduction

## 1.1 Significance of the Project

Because of the excessive carbon dioxide ($CO_2$) emission caused by intensive consumption of fossil fuels, the reduction of $CO_2$ into alternative value-added fuels is a promising method to alleviate greenhouse effect and positively affect the global carbon balance with the input from sustainable energy, such as solar and wind.[1-4] The electrochemical $CO_2$ reduction reaction ($CO_2RR$) has attracted growing attention recently.[5] $CO_2$ can be transformed into value-added chemicals at the cathode, including CO, formic acid (or formate), methane, methanol, ethylene, ethanol, and so on.[6-9] $C_2$ products are generally regarded as more economically valuable than $C_1$ products because of their higher volumetric energy densities and their importance in the synthesis of long-chain hydrocarbon fuels.[10] However, in the catalysis process and the whole reaction, the C–C bond formation process is a critical challenge. This is because it suffers from low selectivity and high overpotential caused by the competition with C–O, C–H bond formations or competitive hydrogen evolution reaction (HER).[11-13] As a result, developing proper electrocatalyst materials which can reduce $CO_2$ to $C_2$ products with high activity, selectivity, and stability is of great importance.[14, 15]

In recent years, single-atom catalysts (SACs) have been applied in many catalytic reactions.[16-18] They showed enhanced activity and selectivity in the application of $CO_2RR$.[19-21] However, most SACs only show activity towards $C_1$ products such as CO and HCOOH during $CO_2RR$ as they only contain one active site.[22, 23] The application of the molecular framework supported SACs is a possible solution to boost $CO_2$ reduction to $C_2$ products by providing a second active site for C–C coupling. Recently, coordinating Cu into the framework of graphitic carbon nitride (g-$C_3N_4$) was found to generate detectable $C_2$ products, including $C_2H_4$, $C_2H_6$, and $C_2H_5OH$.[24] Differing from other traditional nitrogen-doped carbons, the nitrogen species in the g-$C_3N_4$ framework have a strong attraction to $CO_2$ molecules during the electrocatalytic process.[4] In

addition, the adsorption of oxygen-containing reaction intermediates (such as *$OCH_x$, *OH, *O) can be enhanced when using N-doped carbon catalysts because the carbon species in g-$C_3N_4$ show high oxophilicity, benefiting deep reduction production.[24] However, the underlying reaction mechanisms to $CO_2$ reduction to $C_2$ products on the surface of Cu-$C_3N_4$ are still not clear.

Understanding the activity origin such as establishing reaction pathways and analysing the catalytic activity will help develop efficient electrocatalysts.[25] With the considerable improvement in computing power, density functional theory (DFT) calculations can provide a precise description of the electronic structure of catalysts. In addition, it can help explain $CO_2$RR mechanisms on an atomic level by combining the atomic configurations, energy barriers, transition states and so on. Another important application of the DFT method is to validate experimental observations and provide detailed explanations. Correspondingly, through taking advantage of the experimental data, the input parameters can be adjusted to be more reasonable. Nowadays, a large number of studies have successfully identified some active sites and predicted promising novel catalysts via computing methods.[26-28]

The goal of this thesis is to study the reaction mechanisms of $CO_2$ reduction to $C_2H_4$ on metal single atom supported on g-$C_3N_4$. $C_2H_4$ was selected as a representative $C_2$ product during the study because of its essential role in the chemical and fuels industries (*e.g.*, plastic production). It could also serve as a model product to explore the reaction mechanisms and can be expanded to other $C_2$ species formation. Moreover, other metals supported on g-$C_3N_4$ (M-$C_3N_4$) are studied further to evaluate their possibility in generating $C_2$ products. Through unraveling the reaction mechanisms for obtaining $C_2H_4$ based on asymmetrical active sites of metal single atom supported on g-$C_3N_4$, one can gain understanding about the reaction mechanisms for other electrocatalysts with dual active sites. Moreover, it can provide useful guidance for the design of novel electrocatalysts.

## 1.2 Research Objectives

The major goals of this Thesis are to design g-$C_3N_4$ based catalysts for $CO_2$ reduction to $C_2H_4$ by molecular modelling and investigate their reaction mechanisms.

In particular, the objectives of this thesis are:

1.2.1 *To understand* reaction nature and possible $C_2H_4$ product pathways for $CO_2$ reduction at the surface of Cu-$C_3N_4$ and other metal supported on g-$C_3N_4$.

1.2.2 *To discover* the synergetic effect between Cu or other metal and the substrate g-$C_3N_4$

1.2.3 *To evaluate* the performance of different metal supported on g-$C_3N_4$.

## 1.3 Thesis Outline

This thesis is presented in the form of journal publications. The results of the reaction mechanisms studied are included. Specifically, the chapters in the Thesis are presented in the following sequence:

- ***Chapter 1*** presents an introduction for this thesis. It emphasises the significance of this project and outlines the research objectives.
- ***Chapter 2*** reviews the recent progress and challenges of single atom catalysts for $CO_2$ reduction.
- ***Chapter 3*** presents the reaction mechanisms for Cu-$C_3N_4$ with dual active sites for $CO_2$ reduction to ethylene. It focuses on research objective 1.2.1 and 1.2.2.
- ***Chapter 4*** investigates the activity trends for metal single atom catalysts supported on g-$C_3N_4$ for $CO_2$ reduction to $C_2$ products. It focuses on research objective 1.2.1 and 1.2.3.
- ***Chapter 5*** presents the conclusion and perspectives for further work on the design of dual active sites electrocatalyst for $CO_2$RR.

## 1.4 References


1. E. E. Benson, C. P. Kubiak, A. J. Sathrum and J. M. Smieja, Electrocatalytic and homogeneous approaches to conversion of $CO_2$ to liquid fuels, *Chemical Society Reviews*, 2009, **38**, 89-99.
2. C. W. Li, J. Ciston and M. W. Kanan, Electroreduction of carbon monoxide to liquid fuel on oxide-derived nanocrystalline copper, *Nature*, 2014, **508**, 504-507.
3. N. S. Lewis, Research opportunities to advance solar energy utilization, *Science*, 2016, **351**, 1920.
4. J. P. Jones, G. K. S. Prakash and G. A. Olah, Electrochemical $CO_2$ reduction: recent advances and current trends, *Israel Journal of Chemistry*, 2014, **54**, 1451-1466.
5. J. Qiao, Y. Liu, F. Hong and J. Zhang, A review of catalysts for the electroreduction of carbon dioxide to produce low-carbon fuels, *Chemical Society Reviews*, 2014, **43**, 631-675.
6. J. Wu, Y. Huang, W. Ye and Y. Li, $CO_2$ reduction: from the electrochemical to photochemical approach, *Advanced Science*, 2017, **4**, 1700194.
7. A. M. Appel, J. E. Bercaw, A. B. Bocarsly, H. Dobbek, D. L. DuBois, M. Dupuis, J. G. Ferry, E. Fujita, R. Hille and P. J. Kenis, Frontiers, opportunities, and challenges in biochemical and chemical catalysis of $CO_2$ fixation, *Chemical Reviews*, 2013, **113**, 6621-6658.
8. D. U. Nielsen, X. Hu, K. Daasbjerg and T. Skrydstrup, Chemically and electrochemically catalysed conversion of $CO_2$ to CO with follow-up utilization to value-added chemicals, *Nature Catalysis*, 2018, **1**, 244-254.
9. W. Wang, S. Wang, X. Ma and J. Gong, Recent advances in catalytic hydrogenation of carbon dioxide, *Chemical Society Reviews*, 2011, **40**, 3703-3727.

10. A. J. Garza, A. T. Bell and M. Head-Gordon, Mechanism of $CO_2$ reduction at copper surfaces: pathways to $C_2$ products, *ACS Catalysis*, 2018, **8**, 1490-1499.

11. M. Jouny, W. Luc and F. Jiao, High-rate electroreduction of carbon monoxide to multi-carbon products, *Nature Catalysis*, 2018, **1**, 748-755.

12. A. Loiudice, P. Lobaccaro, E. A. Kamali, T. Thao, B. H. Huang, J. W. Ager and R. Buonsanti, Tailoring copper nanocrystals towards $C_2$ products in electrochemical $CO_2$ reduction, *Angewandte Chemie International Edition*, 2016, **55**, 5789-5792.

13. Q. Fan, M. Zhang, M. Jia, S. Liu, J. Qiu and Z. Sun, Electrochemical $CO_2$ reduction to $C_{2+}$ species: Heterogeneous electrocatalysts, reaction pathways, and optimization strategies, *Materials Today Energy*, 2018, **10**, 280-301.

14. S. Zhang, Q. Fan, R. Xia and T. J. Meyer, $CO_2$ reduction: from homogeneous to heterogeneous electrocatalysis, *Accounts of Chemical Research*, 2020, **53**, 255-264.

15. A. D. Handoko, F. Wei, B. S. Yeo and Z. W. Seh, Understanding heterogeneous electrocatalytic carbon dioxide reduction through operando techniques, *Nature Catalysis*, 2018, **1**, 922-934.

16. B. Qiao, A. Wang, X. Yang, L. F. Allard, Z. Jiang, Y. Cui, J. Liu, J. Li and T. Zhang, Single-atom catalysis of CO oxidation using $Pt_1/FeO_x$, *Nature Chemistry*, 2011, **3**, 634-641.

17. M. Jia, Q. Fan, S. Liu, J. Qiu and Z. Sun, Single-atom catalysis for electrochemical $CO_2$ reduction, *Current Opinion in Green and Sustainable Chemistry*, 2019, **16**, 1-6.

18. A. Wang, J. Li and T. Zhang, Heterogeneous single-atom catalysis, *Nature Reviews Chemistry*, 2018, **2**, 65-81.

19. Y. Cheng, S. Yang, S. P. Jiang and S. Wang, Supported single atoms as new class of catalysts for electrochemical reduction of carbon dioxide, *Small Methods*, 2019, **3**, 1800440.

20. A. S. Varela, N. Ranjbar Sahraie, J. Steinberg, W. Ju, H. S. Oh and P. Strasser, Metal-doped nitrogenated carbon as an efficient catalyst for direct $CO_2$ electroreduction to CO and hydrocarbons, *Angewandte Chemie International Edition*, 2015, **54**, 10758-10762.

21. J.-H. Liu, L.-M. Yang and E. Ganz, Efficient and selective electroreduction of $CO_2$ by single-atom catalyst two-dimensional TM-Pc monolayers, *ACS Sustainable Chemistry & Engineering*, 2018, **6**, 15494-15502.

22. Y. Pan, R. Lin, Y. Chen, S. Liu, W. Zhu, X. Cao, W. Chen, K. Wu, W. C. Cheong and Y. Wang, Design of single-atom Co–$N_5$ catalytic site: a robust electrocatalyst for $CO_2$ reduction with nearly 100% CO selectivity and remarkable stability, *Journal of the American Chemical Society*, 2018, **140**, 4218-4221.

23. H. Shang, T. Wang, J. Pei, Z. Jiang, D. Zhou, Y. Wang, H. Li, J. Dong, Z. Zhuang and W. Chen, Design of a Single-Atom Indium$^{\delta+}$-$N_4$ Interface for Efficient Electroreduction of $CO_2$ to Formate, *Angewandte Chemie International Edition*, 2020, **59**, 22465-22469.

24. Y. Jiao, Y. Zheng, P. Chen, M. Jaroniec and S. Z. Qiao, Molecular scaffolding strategy with synergistic active centers to facilitate electrocatalytic $CO_2$ reduction to hydrocarbon/alcohol, *Journal of the American Chemical Society*, 2017, **139**, 18093-18100.

25. Y. Jiao, Y. Zheng, K. Davey and S. Z. Qiao, Activity origin and catalyst design principles for electrocatalytic hydrogen evolution on heteroatom-doped graphene, *Nature Energy*, 2016, **1**, 1-9.

26. C. T. Dinh, T. Burdyny, M. G. Kibria, A. Seifitokaldani, C. M. Gabardo, F. P. García De Arquer, A. Kiani, J. P. Edwards, P. De Luna, O. S. Bushuyev, C. Zou, R. Quintero-Bermudez, Y. Pang, D. Sinton and E. H. Sargent, $CO_2$ electroreduction to ethylene via hydroxide-mediated copper catalysis at an abrupt interface, *Science*, 2018, **360**, 783-787.

27. F. Calle-Vallejo and M. T. Koper, Theoretical considerations on the electroreduction of CO to $C_2$ species on Cu (100) electrodes, *Angewandte Chemie International Edition*, 2013, **52**, 7282-7285.

28. D. R. Alfonso, D. N. Tafen and D. R. Kauffmann, First-principles modeling in heterogeneous electrocatalysis, *Catalysts*, 2018, **8**, 424.

# Chapter 2: Literature Review

## 2.1 Introductory Background

Fossil fuels, including coal, natural gas and petroleum, are considered as major energy sources all around the world to sustain our society and the economy after the industrial revolution in the 19$^{th}$ century. However, the combustion of fossil fuels has raised a series of problems.[1-3] Firstly, the global energy demand increases continuously with the rapid development of the economy and the population. Since fossil fuels are non-renewable resources, people have to face an aggravated energy crisis in the foreseeable future. Secondly, the atmospheric carbon dioxide ($CO_2$) concentration keeps increasing due to the huge combustion amount of fossil fuels from continuing human activity. By May 2020, the atmospheric $CO_2$ concentration reached 417.16 parts per million (ppm). It is believed that the excess $CO_2$ concentration in the atmosphere is the major cause of some undesirable environmental problems, and the most significant one is global warming.[4] Therefore, reducing the impact of excessive $CO_2$ emission is a pressing concern in modern society. People focus on energy-related topics in order to solve the environmental problems and energy crisis. Clean and renewable energy sources such as wind, tide and solar are popular solutions because they can mitigate $CO_2$ emission.

However, although the development of renewable energy is fast, the percentage of them in overall energy consumption is still low.[4] More importantly, the use of the renewable sources is limited as most of them are seasonal, intermitted and geographical, which requires advanced energy conversion and storage technologies.[4] In fact, the conversion of atmospheric $CO_2$ into alternative organic molecules with improved energy density is an alternative solution which can help to solve the aforementioned problems.[5-7] On one hand, this strategy can reduce the accumulation of atmospheric $CO_2$. On the other hand, the products are mainly fuel and industrial chemicals, which can alleviate the energy crisis to some degree.

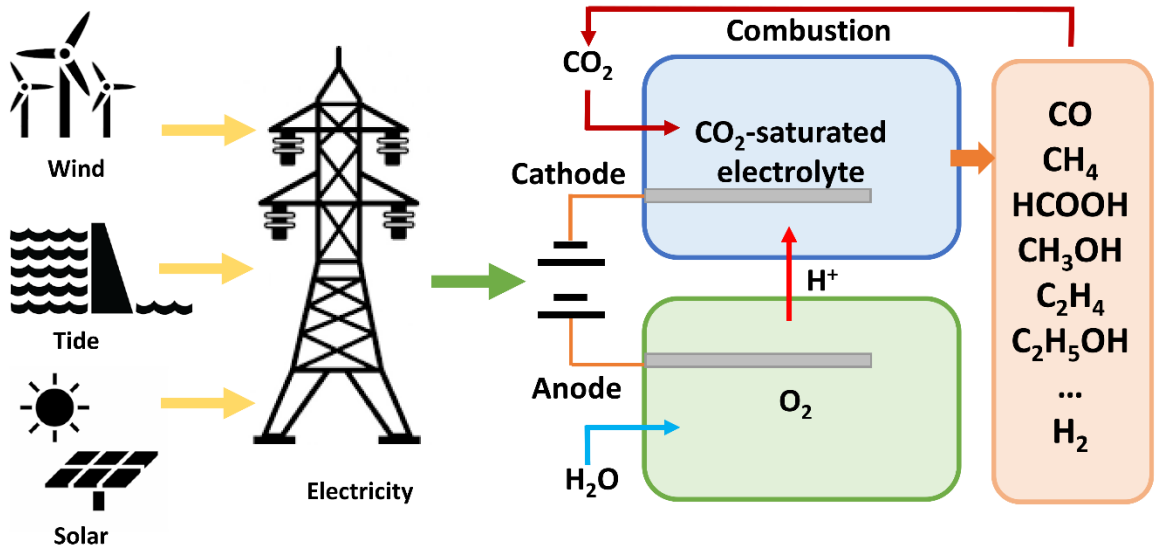


**Figure 1**. Schematic illustration of the electrochemical $CO_2$RR process by renewable energy sources, such as wind, tide, and solar.

### 2.2 Advantages and Challenges for Electrochemical $CO_2$ Reduction Reaction

Various technologies have been proposed and conducted in the past to obtain value-added chemicals, fuels or industrial feedstock from $CO_2$. These technologies include thermochemical, biological, photochemical and electrochemical $CO_2$ reduction.[8-10] Among them, electrochemical $CO_2$ reduction reaction ($CO_2$RR) has attracted growing attention recently for the following advantages: (1) the reaction condition is mild for the process, and the selectivity can be controlled by the reaction temperature and electrode potentials;[11] (2) the electrolytes can be fully recycled, hence the overall chemical consumption can be minimized to simple water or wastewater;[11] (3) through applying renewable electricity from intermittent solar, wind, and tidal energy, it is possible to maintain carbon-neutral balance (Figure 1); (4) the electrochemical reaction systems are compact, modular, on-demand, and easy for scale-up applications.[12]

However, challenges remain for $CO_2$ electroreduction: (1) high reaction overpotentials are demanded to activate and dissociate the C=O double bonds due to the relatively thermodynamic stability of $CO_2$;[13] (2) the reaction selectivity is limited as there are multiple reaction pathways for $CO_2$RR, associating with up to 18 electron transfer steps.[13, 14] This issue is further compounded by hydrogen evolution reaction (HER) which is usually kinetically favoured over $CO_2$RR, existing as the competing side reaction;[15] (3) the energy efficiency of the process is low because of the parasitic or decomposition reaction of the solvent at high reduction potential.[11] Researchers have recognized that low performance of electrocatalyst is the biggest challenge for $CO_2$RR.[11] Therefore, developing stable electrocatalyst materials for $CO_2$ reduction with high activity, selectivity is very important.[16, 17]

$CO_2$RR is a multistep reaction that consists of several proton-coupled electron transfer (PCET) processes, involving the transfer of two, four, six, eight, twelve, or even more electrons to form various products.[14] Therefore, $CO_2$ can be transformed into value-added chemicals, including CO, formic acid (or formate), methane, methanol, ethylene, ethanol, and so on.[8, 10, 18, 19] Normally, there are three major steps in the heterogeneous catalysis processes. Firstly, $CO_2$ is adsorbed to the surface of the electrocatalyst. Secondly, C-O bonds in $CO_2$ are cleaved and C-H bonds are formed through proton-electron transfer. Finally, via configuration rearrangement, products are then desorbed from the surface of the electrocatalyst and diffused into the electrolyte.[20] The simultaneous proton-electron transfer leads to different bond formation steps during the above processes, including hydrogenation of carbon, hydrogenation of oxygen, and carbon-carbon coupling, generating various intermediates and products.[14]

Comparing with producing methane or ethylene, forming CO requires overcoming significantly reduced energy barrier, hence it is relatively simple. Therefore, $CO_2$ reduction to CO has been widely investigated.[21] The production of CO and HCOOH has achieved relatively high reduction current density and selectivity.[18] However, the selectivity of deep reduction

products is still unsatisfactory.[22] $C_2$ products are used widely as chemical feedstock.[23-25] Moreover, comparing with $C_1$ products, $C_2$ are more preferable because of their higher energy density.[26] The main challenge for obtaining $C_2$ product is the carbon-carbon (C-C) coupling step, which is an essential reaction step for the formation of multicarbon products. Therefore, understanding the reaction mechanisms of C-C coupling steps is important for finding a suitable catalyst having exclusive selectivity for $C_2$ products.

### 2.3 Atomistic Mechanism of Various $C_2$ Products and C-C Coupling

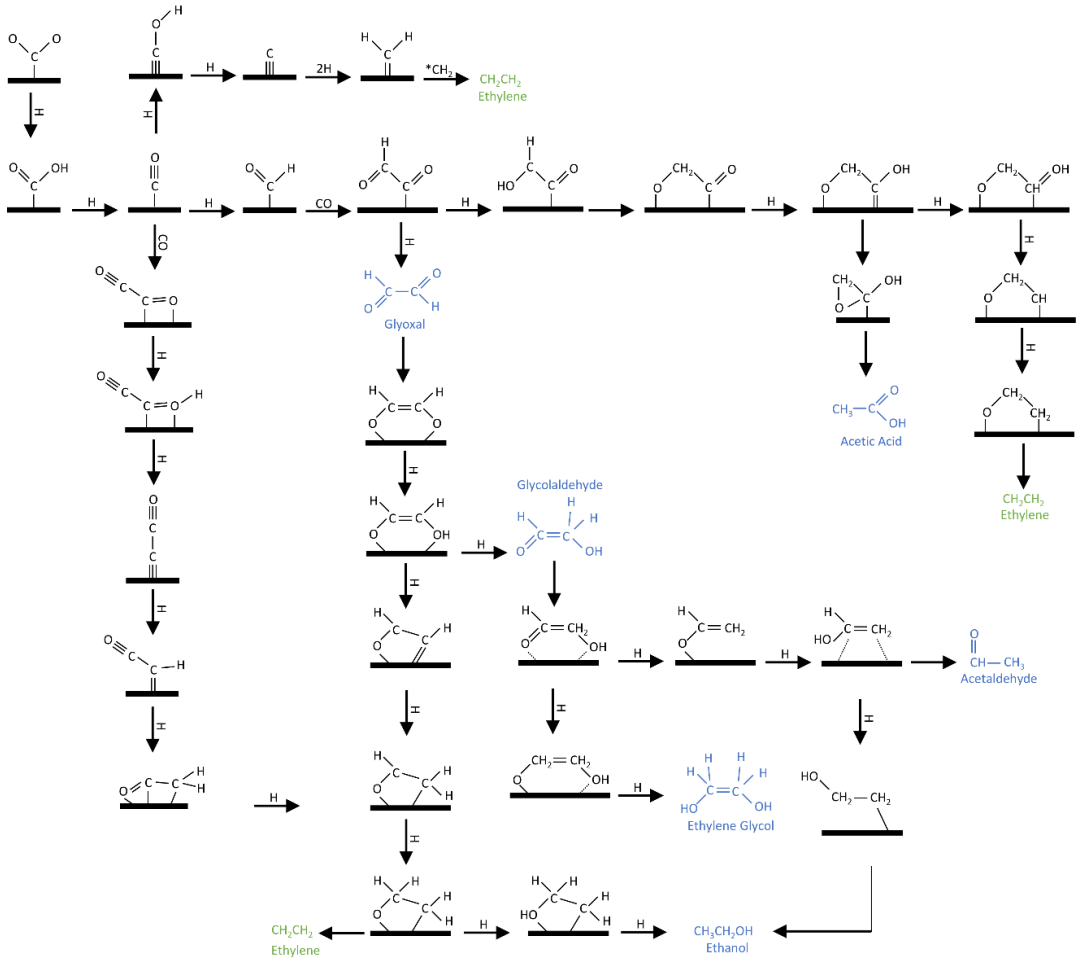


**Figure 2**. Proposed mechanisms for the reduction of $CO_2$ to seven $C_2$ products through electrochemical processes. Ethylene production is highlighted in green, while the other six $C_2$ productions are highlighted in blue.

With the help of density functional theory (DFT) simulations, the reaction network for $CO_2$ reduction to $C_2$ products can be predicted. Figure 2 summarized the proposed reaction mechanisms for $CO_2$ reduction to seven different $C_2$ products including ethylene, ethanol, glyoxal, glycolaldehyde, ethylene glycol, acetic acid, and acetaldehyde. As shown in Figure 2, there are many intermediates involved in $CO_2$RR. Besides, many reaction pathways share the same intermediates, leading to poor selectivity for one product. Moreover, there are multiple pathways to obtain one product. To be specific, in Figure 2 there are three pathways obtaining ethylene, and two pathways obtaining ethanol. Fan et al. proposed that the $C_2H_4$ generation mechanisms include nonelectrochemical coupling of two $*CH_2$ species, the combination of $*CH_2$ and CO, and *CO dimerization.[27]

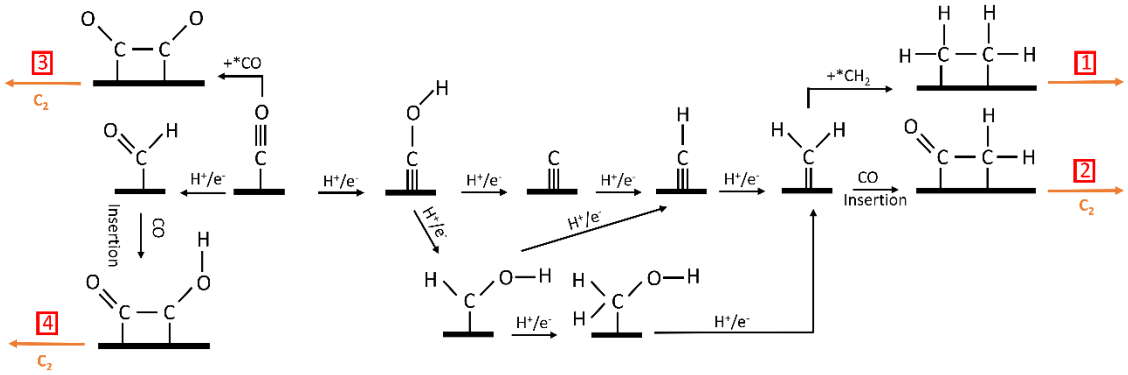


**Figure 3**. Four possible C-C bond formation mechanisms from *CO on the Cu surfaces. The red numbers indicate the different C-C bond formation mechanisms.

Since the reaction pathways to $C_2$ products are very complex, focusing on C-C coupling process is a good method to help understand the reaction mechanisms for $CO_2$ reduction to $C_2$ products, which will also benefit the design of the related catalysts. The formation of C-C bond is regarded as the most probable rate determining step when producing $C_2$ products. Based on experimental research results and application of DFT, several possible mechanisms have been

proposed.[28] The possible C-C coupling mechanisms are summarized in Figure 3. Number one and two mechanisms in Figure 3 were proposed by Hori et al., one is the direct dimerization of $*CH_2$, and the other is the formation of $*CH_2CO$ by CO insertion.[29] The results showed that $*CH_2$ dimerization is favorable on Cu (111) via the analyzation of thermodynamic energy and reaction kinetic barrier.[30] However, the above two mechanisms cannot explain why experimental results indicate that no $C_2H_6$ was found in Cu electrodes.[29] Hence, other C-C forming processes are required to explain the experimental observations. Calle-Vallejo and Koper proposed CO dimerization (to form *CO-CO) as the first step to $C_2$ products, which is number three mechanism in Figure 3.[31] It was found that *CO dimerization is the key step in C-C coupling process and is more energeticly favorable at low overpotentials.[27, 32, 33] Moreover, another C-C coupling pathway is proposed, which is the formation of *CO-COH, number four in Figure 3.[31] The pH dependence of $C_2H_4$ formation and the preference for $C_2H_4$ formation in alkaline media can be properly explained by this mechanism.[28]

### 2.4 Other Metals and Copper in Application of $CO_2RR$

In the past studies, various metal electrodes have been investigated as potential catalysts for $CO_2RR$, including Cu, Au, Ag, Pd, Zn, Ni, Fe, Pt, Cd, Sn, In and so on.[34, 35] The possible reaction pathways and reaction mechanisms of $CO_2RR$ on these electrodes have been studied experimentally and theoretically for years.[23, 36-38] Most of the reported catalysts for $CO_2RR$ are capable to reduce $CO_2$ to CO or HCOOH with high efficiency and selectivity. The main product for Au, Ag, Zn, Pd metal sites is CO, and that for Pb, In, Sn, Cd is HCOOH.[35] HER is generally favoured over $CO_2RR$ on Ni, Fe, Pt. Among them, Cu is the only monometallic catalyst found so far that can produce hydrocarbons and oxygenates including up to three carbon atoms.[39-41] Therefore, Cu has been studied extensively because of its unique property in $CO_2RR$.

Hori and his co-workers conducted pioneer researches on Cu electrodes in the 1980s.[40] The outstanding performance can be explained by the appropriate adsorption strength of the

relevant intermediates.[23, 42, 43] Although the Faradaic efficiencies (FEs) are fairly high for the electrolcatalysis of $CO_2$ into low-carbon hydrocarbons and oxygenates, the overpotential required is relatively large, which is nearly 1V.[13, 40, 44, 45] Furthermore, there are other typical diaadvantages for Cu electrode, including low product selectivity and short catalyst lifetime.[43] The different surface morphologies or structures of Cu provide various reaction pathways and product distributions.[46, 47] In order to obtain a better result, several methods have been applied to modify the morphology of Cu, such as nanostructuring and bimetallic alloys.[39]

The current effort of most studies has been focused on the facilitation of C-C coupling based on metallic Cu systems.[22] Since there are at least 16 different products that have been explored on the surface of Cu, it is not considered as a selective catalyst for specific product.[13] Therefore, Cu modification is necessary to obtain desirable products. Reske et al. have explored relevant catalytic behaviours for copper nanoparticles (NPs) with size ranging from 2 to 15 nm.[48] They found that for bulk Cu catalysts, $CH_4$ is the predominant product, while smaller size NPs show a higher activity and increased selectivity to $H_2$ and CO, as they possess numerous low coordinated sites.[48] However, the selectivity for $C_{2+}$ products can be enhanced through applying complicated architectures for Cu.[28] For example, the selectivity for $C_{2+}$ products on the mesoporous Cu film can be controlled through tuning its pore size and depth. The fluid transformation speed is reduced by the pores, and hence the inside ion concentration is increased.[28] Therefore, the intermediates are likely to be trapped in the pores and confined to facilitating long chain molecules.[28] Consequently, $C_{2+}$ product selectivity is enhanced. This phenomenon inspired the design of the cavities to restrict the outflow of produced $C_2$ products and facilitate further $C_3$ products.[28]

### 2.5 Single Atom Catalyst in Application of $CO_2RR$

Single atom catalysts (SACs) have attracted enormous attention in electrocatalysis up to now.[49-51] The active sites in SACs are homogeneously dispersed, hence displaying analogous catalytic behaviour.[52] The catalytic activity and selectivity toward various electrochemical reaction can be obviously increased through downsizing metal nanoparticles into single atoms.[53] Moreover, atom utilization is increased because of the high dispersion of metal atoms, hence reducing costs in large scale applications.[54] At the same time, the electrocatalytic performance of SACs can be improved by the unsaturated coordination environments and the interactions between individual atoms and supports.[55, 56] However, the aggregation of these single atoms becomes easy due to their high surface free energy. Therefore, various substrates are required to form a stable configuration for the isolated atoms. The changes in the coordination structure for one same active metal center can cause different reaction activities and production distribution.[57] The nanostructured two-dimensional (2D) materials have proven to be a suitable substrate or support for SACs, especially modified or doped carbon-based graphene.[58] This is because the coupling of metal with carbons can tune the electronic structure for catalysis by promoting the charge transfer between them.[59, 60]

Many studies have shown that single-atom metal-based nitrogen-doped carbon (M-N-C) catalysts are attractive electrocatalysts for $CO_2RR$.[61-63] M-N-C has been studied extensively as an efficient $CO_2RR$ catalyst for $CO_2$ reduction to CO and M-N-C catalysts based on Fe, Co and Ni have demonstrated high activity and selectivity for CO formation.[61] Fe SACs exhibits a maximum CO FE for more than 90%.[64, 65] For example, Fe and N doped porous carbon nematosphere (FeNPCN) is reported to give a FE of 94% for $CO_2$ reduction to CO.[66] Ni SACs are regarded as highly efficient electrocatalysts for $CO_2$ reduction to CO. Atomically dispersed Ni on nitrogenated graphene codoped with S (A-Ni-NSG) is reported to have 97% FE at -0.5 V vs reversible hydrogen electrode (RHE) for CO conversion.[67] It was found that the geometry

around Ni(I) in A-Ni-NSG was highly distorted because of the noncentrosymmetric ligand strength, promoting better adsorption of reactants and intermediates on the surface (Figure 4a and 4b).[68] Recently, Li and co-workers reported a Ni-$N_4$-C catalyst giving a maximum FE of 99% at - 0.81 V vs RHE with a current density of 28.6 mA $cm^{-2}$ for $CO_2$ reduction to CO (Figure 4c).[63] The high selectivity of Ni-$N_4$-C was further analysed by DFT calculations. The results demonstrated that the excellent selectivity is obtained because the Ni-$N_4$ species decreases the formation energy of *COOH (Figure 4d).[63]

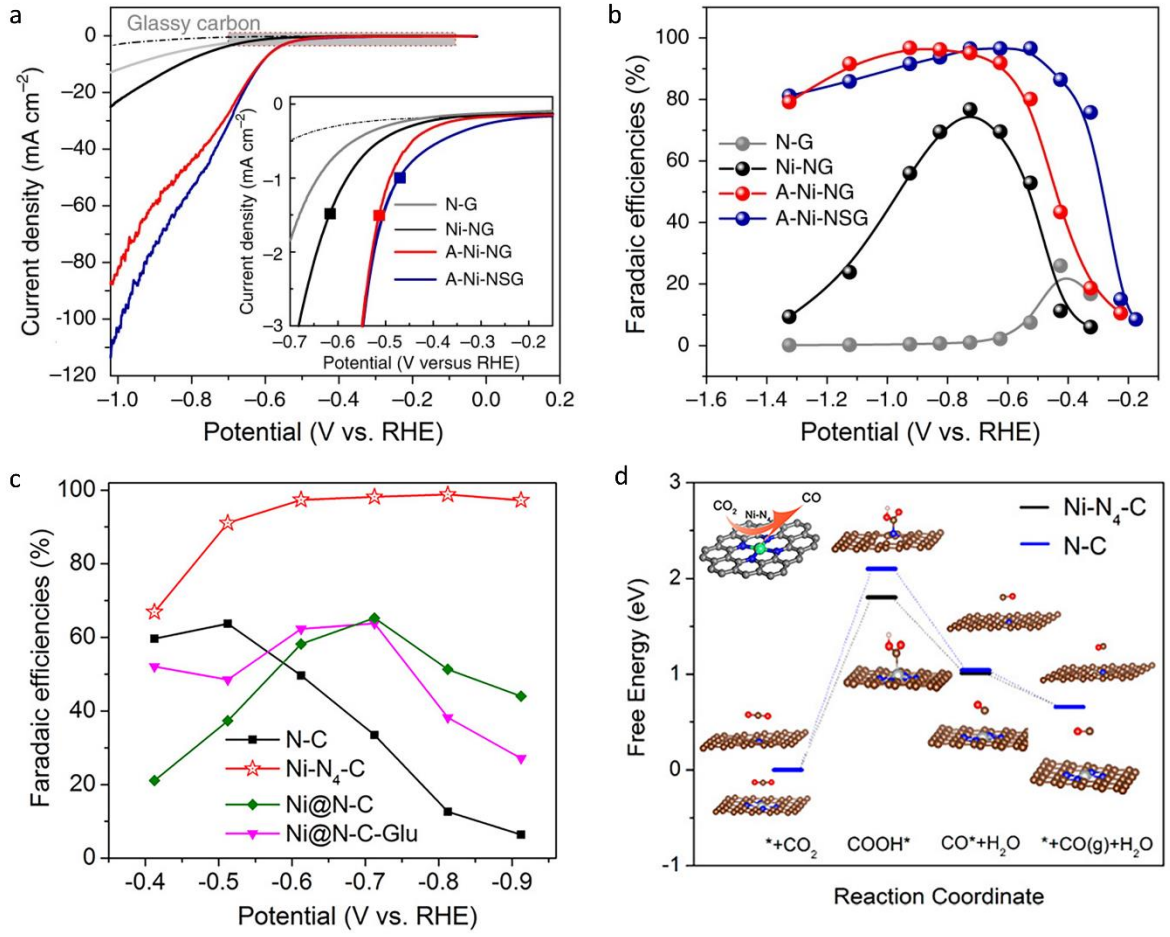


**Figure 4**. a) LSV curves acquired in $CO_2$-saturated 0.5 M $KHCO_3$ solution on a rotating disc electrode at a rotation speed of 1,600 r.p.m. and a scan rate of 5 mV $s^{-1}$ for N-G, Ni-NG, A-Ni-NG, and A-Ni-NSG. Catalyst loading: 0.1 mg $cm^{-2}$. b) CO Faradaic efficiency at various applied potentials for N-G, Ni-NG, A-Ni-NG, and A-Ni-NSG. c) Faradaic efficiencies for CO

generation on N-C, Ni-$N_4$-C, Ni@N-C, and Ni@N-C-Glu. d) Calculated free energy diagrams for $CO_2$RR on Ni-$N_4$-C and N-C. Schematic illustration of Ni-$N_4$-C is shown in the left top conner (green: Ni atom, blue: N atom, grey: C atom, red: O atom). a, b) Reproduced with permission.[67] Copyright 2018, Nature Energy. c, d) Reproduced with permission.[63] Copyright 2017, American Chemical Society.

Apart from the above single atom materials based on doped carbon-based graphene materials, several Cu-N-C electrocatalysts were also reported as electrocatalysts for $CO_2$RR to $C_1$ products.[69, 70] The reaction mechanisms for $CO_2$ reduction on Cu loaded carbon nitride (Cu/CN) are presented in Figure 5a, as well as the possible products include CO, HCOOH, HCHO, $CH_3OH$, and $CH_4$.[70] Since the desorption of $CH_3OH$* on Cu/CN is as high as 0.41 eV, it can be further reduced to $CH_4$, and this pathway is regarded as the primary reaction on Cu/CN.[70] Dominant $C_1$ products are obtained for Cu-N-C electrocatalysts because of the lack of ensemble size of single-atom active sites.[71] Hence, further reduction of $CO_2$ to hydrocarbons or alcohols becomes challenging for single atom electrocatalysts.

The synergetic effect between single atom and the carbon nitride support is regarded as a novel strategy for designing $CO_2$RR electrocatalysts facilitating C-C coupling by stabilizing $C_{2+}$ reaction intermediates. For example, Cu single sites on g-$C_3N_4$ were observed to generate detectable $C_2$ products, including $C_2H_4$, $C_2H_6$, and $C_2H_5OH$ (Figure 5b).[71] Differing from other traditional nitrogen-doped carbons, the nitrogen species in the g-$C_3N_4$ framework have a strong attraction to $CO_2$ molecules during the electrocatalytic process, which is regarded important for $CO_2$ activation.[72] Moreover, it has been demonstrated by DFT calculations that the adsorption of oxygen-containing reaction intermediates (such as *$OCH_x$, *OH, *O) can be enhanced when using N-doped carbon catalysts because the carbon species in g-$C_3N_4$ show

high oxophilicity (Figure 5c), which benefits deep reduction production. As the electronic structure for copper is influenced by g-$C_3N_4$, the position of the d-orbital of copper can be uplifted due to the Fermi level.[71] Therefore, Cu-$C_3N_4$ has a stronger affinity with reaction intermediates and higher $CO_2$ activation. In addition, copper and carbon in Cu-$C_3N_4$ can work in synergy across the whole reduction process to provide a deeper $CO_2$ reduction through the dual active sites. However, there is a lack of systematic studies on reaction mechanism for $CO_2$ reduction to $C_2$ products on Cu-$C_3N_4$. Further fundamental understanding through theoretical modelling is necessary. Through theoretical calculations, we can understand the reaction mechanism for $CO_2$RR and the involved active sites, which helps guide new catalyst development.

To this end, double-atom catalysts (DACs) is another method which may favour $C_{2+}$ selectivity. As a natural extension of SACs, DACs are predicted to boost $CO_2$ reduction to $C_2$ products owing to the synergetic effect between adjacent active sites of metal dimer.[73, 74] Through C-C coupling on dual active sites, deep reduction products, such as $C_2H_4$ and $C_2H_5OH$ can be obtained.[75-77] For example, Guan et al. developed a Cu,N-codoped carbon nanosheet structure by atomically constructing the single-atom distribution of Cu-$N_x$ coordination, with varying Cu-doping concentrations.[78] At a high Cu loading density of 4.9%$_{mol}$, the material produces $C_2H_4$ as the main $CO_2$ reduction products. This is because the two adjacent Cu-$N_2$ sites are close to each other, enhancing the C-C coupling.[78] In addition, Chen et al. designed a 2D graphene nitrene heterostructure (grafi$N_6$) which can bind up to three metals for $CO_2$RR.[77]

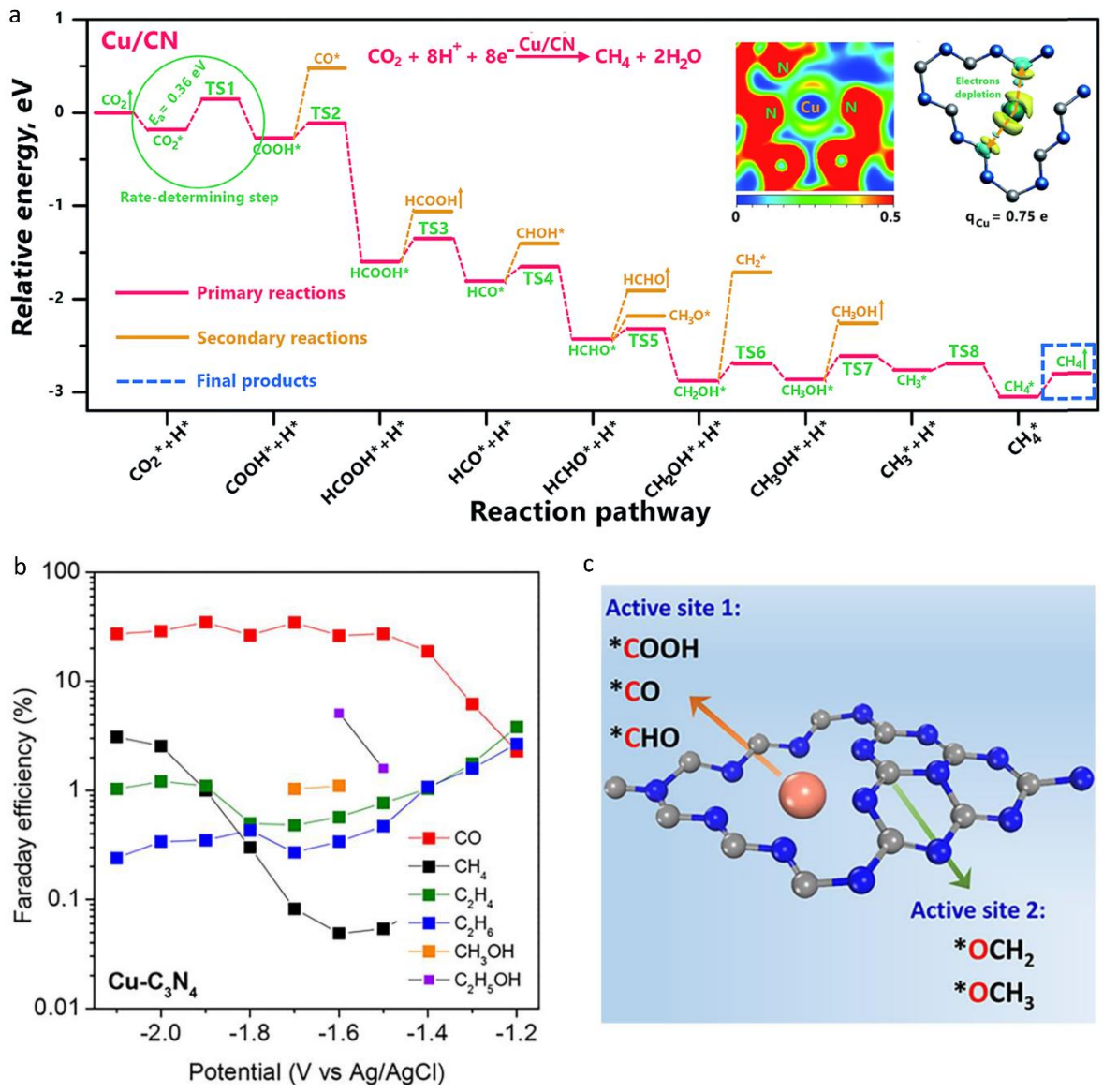


**Figure 5**. a) The calculated reaction pathways for the photocatalytic $CO_2$RR on Cu/CN, in which the climbing image nudged elastic band (CI-NEB) method is used. Electronic localization function (ELF) and charge density difference result for Cu/CN is presented at the top right corner. Color code: C blue, N grey, Cu green. Blue represents electron accumulation, and yellow represents electron depletion. The isosurface is set to 0.006 eV $Å^{-3}$. Positive values of q depict electron depletion. b) The measured Faradaic efficiencies of various products on Cu-$C_3N_4$. c) Schematic illustration of active sites of Cu-$C_3N_4$. Color code: C green, N blue, Cu orange. a) Reproduced with permission.[70] Copyright 2019, Royal Society of Chemistry. b, c) Reproduced with permission.[71] Copyright 2017, American Chemical Society.

## 2.6 Methods

Although $CO_2RR$ process has been studied for around 20 to 30 years, recognition of the intermediates is still a key problem during the experiment, and the reaction mechanism is not clearly understood. Generally, experimental measurements are applied to evaluate the performance of the process by providing observable characteristics, including linear sweep voltammetry (LSV) curves, current density, faradaic efficiency, and product selectivity. However, the atomic level details for the electrochemical process cannot be elucidated by experiments due to the limitation of the experimental technique and the short intermediate transient lifetime.[79] In addition, the transition states cannot be easily identified by applying kinetic experiment data only.[79] Therefore, it is hard to establish atomic scale interpretation of experimental data, which is crucial for developing catalysts. The application of theoretical insight is a suitable method to solve the above problems, which can identify the reaction mechanisms of the electroreduction of $CO_2$ to hydrocarbons using theoretical calculations.

Density Functional Theories (DFT) is a computational quantum mechanical modelling method. It can be used to investigate the electronic structure and determine the properties of a system including many electrons. The computational cost has been reduced and the calculations for relatively larger systems such as nanoparticles and periodic surfaces become possible through applying DFT calculations.[79] Moreover, $CO_2RR$ mechanisms can be explained on an atomic level by combining the atomic configurations, energy barriers, transition states and so on. Another important application of the DFT method is to validate experimental observations and provide detailed explanations. Correspondingly, through taking advantage of the experimental data, the input parameters can be adjusted to be more reasonable. Nowadays, a large number of studies have successfully identified some active sites and predicted promising novel catalysts via computing methods. For instance, Dinh et al. used DFT to assess the influence of the hydroxide ions on the energy barrier during CO dimerization step and found out that

hydroxide can reduce the binding strength of CO on the surface of Cu and increase the charge imbalance as well.[80] Shin et al. also carried out a DFT study on AgCu bimetallic nanoparticles to evaluate their performance on oxygen reduction reaction (ORR).[81]

The field of modelling electrochemical processes developed rapidly with the introduction of computational hydrogen electrode (CHE) approach in 2004.[82] The reaction $H^+ + e^- \leftrightarrow \frac{1}{2}H_2$ is defined to be in equilibrium at pH = 0 and zero voltage, under standard conditions. The free energy of the electron-proton pair ($H^+ + e^-$) can be referenced to the chemical potential of gaseous $H_2$ under standard conditions (0 V vs standard hydrogen electrode, at 101,325 Pa). The free energies of reactants and each intermediate state at an applied electrode potential U is calculated by using the formula expressed as follows: $G(U) = G - neU$, where n is the electron number of such state, e is the electric charge of one electron, and G is the free energy obtained by the frequency calculations at room temperature (298.15 K) after geometry optimization. The free energy of $H^+$ was derived as $G_{H+} = 1/2\, G_{H2} - k_B T ln10 \times \mathrm{pH}$, in which $k_B$ is Boltzmann's constant, and T is the room temperature (T = 298.15 K). The Gibbs free energy calculation for the elementary steps can be obtained

$$\mathrm{G} = \mathrm{E} - \mathrm{TS} + \mathrm{ZPE} + \int C_p dT \quad (1)$$

in which E indicates the electronic energy obtained by DFT calculations. S and ZPE indicate entropy and zero-point energy corrections, and T is temperature. ZPE and vibrational entropy of adsorbed species were obtained once vibrational frequencies were calculated. Entropies of gas molecules ($H_2$ and $CO_2$) were taken from standard values.[83]

In this project, electronic structure calculations are performed by DFT in the form of the Perdew-Burke-Ernzerhof (PBE) exchange-correlation functional using a projector augmented-wave method in the Vienna Ab Initio Simulation Package (VASP) code.[84-87] The plane-wave for the electron wave functions is expanded by using a 500 eV kinetic energy cutoff. The

convergence criteria for the electronic structure iteration and the geometry optimization is set as $10^{-5}$ eV and 0.01 eV/ Å respectively. For the M-$C_3N_4$ unit cell, the Brillouin zone (BZ) is sampled with a Monkhorst-Pack mesh with a 5 × 5 × 1 k-point grid in reciprocal space during geometry optimization and Nudged Elastic Band (NEB) calculations. Considering the van der Waals interactions between atoms, the Tkatchenko-Scheffler method is applied for all calculations.[88] Solvation calculations are performed for some pathways using VASPsol, in which the solvation energies are modelled on periodic systems.[89, 90]

The overall reaction of $CO_2$ reduction to form $C_2H_4$ on the surface of M-$C_3N_4$ in the presence of hydrogen is expressed in the following formula and the reaction includes 12 elementary hydrogenation steps.

$$2CO_2(g) + 8H_2O(l) + 12e^- \rightarrow C_2H_4(g) + 12OH^-$$

$$E^0_{C_2H_4} = -0.934 \text{ V vs. SHE} \quad (2)$$

**2.7 References**


1. N. Mac Dowell, P. S. Fennell, N. Shah and G. C. Maitland, The role of $CO_2$ capture and utilization in mitigating climate change, *Nature Climate Change*, 2017, **7**, 243-249.
2. S. J. Davis, K. Caldeira and H. D. Matthews, Future $CO_2$ emissions and climate change from existing energy infrastructure, *Science*, 2010, **329**, 1330-1333.
3. A. Haines, R. S. Kovats, D. Campbell-Lendrum and C. Corvalán, Climate change and human health: impacts, vulnerability, and mitigation, *The Lancet*, 2006, **367**, 2101-2109.
4. D. D. Zhu, J. L. Liu and S. Z. Qiao, Recent advances in inorganic heterogeneous electrocatalysts for reduction of carbon dioxide, *Advanced Materials*, 2016, **28**, 3423-3452.

5. M. G. Kibria, J. P. Edwards, C. M. Gabardo, C. T. Dinh, A. Seifitokaldani, D. Sinton and E. H. Sargent, Electrochemical $CO_2$ reduction into chemical feedstocks: from mechanistic electrocatalysis models to system design, *Advanced Materials*, 2019, **31**, 1807166.

6. S. Nitopi, E. Bertheussen, S. B. Scott, X. Liu, A. K. Engstfeld, S. Horch, B. Seger, I. E. Stephens, K. Chan and C. Hahn, Progress and perspectives of electrochemical $CO_2$ reduction on copper in aqueous electrolyte, *Chemical Reviews*, 2019, **119**, 7610-7672.

7. O. Ola and M. M. MarotoValer, Review of material design and reactor engineering on $TiO_2$ photocatalysis for $CO_2$ reduction, *Journal of Photochemistry and Photobiology C: Photochemistry Reviews*, 2015, **24**, 16-42.

8. A. M. Appel, J. E. Bercaw, A. B. Bocarsly, H. Dobbek, D. L. DuBois, M. Dupuis, J. G. Ferry, E. Fujita, R. Hille and P. J. Kenis, Frontiers, opportunities, and challenges in biochemical and chemical catalysis of $CO_2$ fixation, *Chemical Reviews*, 2013, **113**, 6621-6658.

9. S. Roy, A. Cherevotan and S. C. Peter, Thermochemical $CO_2$ hydrogenation to single carbon products: scientific and technological challenges, *ACS Energy Letters*, 2018, **3**, 1938-1966.

10. J. Wu, Y. Huang, W. Ye and Y. Li, $CO_2$ reduction: from the electrochemical to photochemical approach, *Advanced Science*, 2017, **4**, 1700194.

11. J. Qiao, Y. Liu, F. Hong and J. Zhang, A review of catalysts for the electroreduction of carbon dioxide to produce low-carbon fuels, *Chemical Society Reviews*, 2014, **43**, 631-675.

12. A. S. Agarwal, Y. Zhai, D. Hill and N. Sridhar, The electrochemical reduction of carbon dioxide to formate/formic acid: engineering and economic feasibility, *ChemSusChem*, 2011, **4**, 1301-1310.

13. K. P. Kuhl, E. R. Cave, D. N. Abram and T. F. Jaramillo, New insights into the electrochemical reduction of carbon dioxide on metallic copper surfaces, *Energy & Environmental Science*, 2012, **5**, 7050-7059.

14. R. Kortlever, J. Shen, K. J. P. Schouten, F. Calle-Vallejo and M. T. Koper, Catalysts and reaction pathways for the electrochemical reduction of carbon dioxide, *The Journal of Physical Chemistry Letters*, 2015, **6**, 4073-4082.

15. Y. Zhang, V. Sethuraman, R. Michalsky and A. A. Peterson, Competition between $CO_2$ reduction and $H_2$ evolution on transition-metal electrocatalysts, *ACS Catalysis*, 2014, **4**, 3742-3748.

16. S. Zhang, Q. Fan, R. Xia and T. J. Meyer, $CO_2$ reduction: from homogeneous to heterogeneous electrocatalysis, *Accounts of Chemical Research*, 2020, **53**, 255-264.

17. A. D. Handoko, F. Wei, B. S. Yeo and Z. W. Seh, Understanding heterogeneous electrocatalytic carbon dioxide reduction through operando techniques, *Nature Catalysis*, 2018, **1**, 922-934.

18. D. U. Nielsen, X. Hu, K. Daasbjerg and T. Skrydstrup, Chemically and electrochemically catalysed conversion of $CO_2$ to CO with follow-up utilization to value-added chemicals, *Nature Catalysis*, 2018, **1**, 244-254.

19. W. Wang, S. Wang, X. Ma and J. Gong, Recent advances in catalytic hydrogenation of carbon dioxide, *Chemical Society Reviews*, 2011, **40**, 3703-3727.

20. R. Schlögl, Heterogeneous catalysis, *Angewandte Chemie International Edition*, 2015, **54**, 3465-3520.

21. X. Wang, Q. Zhao, B. Yang, Z. Li, Z. Bo, K. H. Lam, N. M. Adli, L. Lei, Z. Wen and G. Wu, Emerging nanostructured carbon-based non-precious metal electrocatalysts for selective electrochemical $CO_2$ reduction to CO, *Journal of Materials Chemistry A*, 2019, **7**, 25191-25202.

22. D. Gao, R. M. Arán-Ais, H. S. Jeon and B. R. Cuenya, Rational catalyst and electrolyte design for $CO_2$ electroreduction towards multicarbon products, *Nature Catalysis*, 2019, **2**, 198-210.

23. A. A. Peterson, F. Abild-Pedersen, F. Studt, J. Rossmeisl and J. K. Norskov, How copper catalyzes the electroreduction of carbon dioxide into hydrocarbon fuels, *Energy & Environmental Science*, 2010, **3**, 1311-1315.

24. H. Mistry, A. S. Varela, C. S. Bonifacio, I. Zegkinoglou, I. Sinev, Y. W. Choi, K. Kisslinger, E. A. Stach, J. C. Yang and P. Strasser, Highly selective plasma-activated copper catalysts for carbon dioxide reduction to ethylene, *Nature Communications*, 2016, **7**, 1-9.

25. E. Bertheussen, A. Verdaguer-Casadevall, D. Ravasio, J. H. Montoya, D. B. Trimarco, C. Roy, S. Meier, J. Wendland, J. K. Nørskov and I. E. Stephens, Acetaldehyde as an intermediate in the electroreduction of carbon monoxide to ethanol on oxide-derived copper, *Angewandte Chemie International Edition*, 2016, **55**, 1450-1454.

26. Y. Huo, X. Peng, X. Liu, H. Li and J. Luo, High selectivity toward $C_2H_4$ production over Cu particles supported by butterfly-wing-derived carbon frameworks, *ACS Applied Materials & Interfaces*, 2018, **10**, 12618-12625.

27. Q. Fan, M. Zhang, M. Jia, S. Liu, J. Qiu and Z. Sun, Electrochemical $CO_2$ reduction to $C_{2+}$ species: Heterogeneous electrocatalysts, reaction pathways, and optimization strategies, *Materials Today Energy*, 2018, **10**, 280-301.

28. Y. Zheng, A. Vasileff, X. Zhou, Y. Jiao, M. Jaroniec and S. Z. Qiao, Understanding the roadmap for electrochemical reduction of $CO_2$ to multi-carbon oxygenates and hydrocarbons on copper-based catalysts, *Journal of the American Chemical Society*, 2019, **141**, 7646-7659.

29. Y. Hori, R. Takahashi, Y. Yoshinami and A. Murata, Electrochemical reduction of CO at a copper electrode, *The Journal of Physical Chemistry B*, 1997, **101**, 7075-7081.

30. X. Nie, M. R. Esopi, M. J. Janik and A. Asthagiri, Selectivity of $CO_2$ reduction on copper electrodes: the role of the kinetics of elementary steps, *Angewandte Chemie*, 2013, **125**, 2519-2522.

31. F. Calle-Vallejo and M. T. Koper, Theoretical considerations on the electroreduction of CO to $C_2$ species on Cu (100) electrodes, *Angewandte Chemie International Edition*, 2013, **52**, 7282-7285.

32. H. Xiao, T. Cheng and W. A. Goddard, Atomistic mechanisms underlying selectivities in $C_1$ and $C_2$ products from electrochemical reduction of CO on Cu (111), *Journal of the American Chemical Society*, 2016, **139**, 130-136.

33. J. D. Goodpaster, A. T. Bell and M. Head-Gordon, Identification of possible pathways for C–C bond formation during electrochemical reduction of $CO_2$: New theoretical insights from an improved electrochemical model, *The Journal of Physical Chemistry Letters*, 2016, **7**, 1471-1477.

34. J. Zhou and Y. Zhang, Metal-based heterogeneous electrocatalysts for reduction of carbon dioxide and nitrogen: mechanisms, recent advances and perspective, *Reaction Chemistry & Engineering*, 2018, **3**, 591-625.

35. Y. Hori, H. Wakebe, T. Tsukamoto and O. Koga, Electrocatalytic process of CO selectivity in electrochemical reduction of $CO_2$ at metal electrodes in aqueous media, *Electrochimica Acta*, 1994, **39**, 1833-1839.

36. A. A. Peterson and J. K. Nørskov, Activity descriptors for $CO_2$ electroreduction to methane on transition-metal catalysts, *The Journal of Physical Chemistry Letters*, 2012, **3**, 251-258.

37. H. A. Hansen, J. B. Varley, A. A. Peterson and J. K. Nørskov, Understanding trends in the electrocatalytic activity of metals and enzymes for $CO_2$ reduction to CO, *The Journal of Physical Chemistry Letters*, 2013, **4**, 388-392.

38. C. Shi, H. A. Hansen, A. C. Lausche and J. K. Nørskov, Trends in electrochemical $CO_2$ reduction activity for open and close-packed metal surfaces, *Physical Chemistry Chemical Physics*, 2014, **16**, 4720-4727.

39. M. Jouny, W. Luc and F. Jiao, High-rate electroreduction of carbon monoxide to multi-carbon products, *Nature Catalysis*, 2018, **1**, 748-755.

40. Y. Hori, A. Murata and R. Takahashi, Formation of hydrocarbons in the electrochemical reduction of carbon dioxide at a copper electrode in aqueous solution, *Journal of the Chemical Society, Faraday Transactions 1: Physical Chemistry in Condensed Phases*, 1989, **85**, 2309-2326.

41. C. S. Chen, A. D. Handoko, J. H. Wan, L. Ma, D. Ren and B. S. Yeo, Stable and selective electrochemical reduction of carbon dioxide to ethylene on copper mesocrystals, *Catalysis Science & Technology*, 2015, **5**, 161-168.

42. A. Loiudice, P. Lobaccaro, E. A. Kamali, T. Thao, B. H. Huang, J. W. Ager and R. Buonsanti, Tailoring copper nanocrystals towards $C_2$ products in electrochemical $CO_2$ reduction, *Angewandte Chemie International Edition*, 2016, **55**, 5789-5792.

43. X. Nie, W. Luo, M. J. Janik and A. Asthagiri, Reaction mechanisms of $CO_2$ electrochemical reduction on Cu (111) determined with density functional theory, *Journal of Catalysis*, 2014, **312**, 108-122.

44. S. Ma, M. Sadakiyo, R. Luo, M. Heima, M. Yamauchi and P. J. Kenis, One-step electrosynthesis of ethylene and ethanol from $CO_2$ in an alkaline electrolyzer, *Journal of Power Sources*, 2016, **301**, 219-228.

45. C. W. Li and M. W. Kanan, $CO_2$ reduction at low overpotential on Cu electrodes resulting from the reduction of thick $Cu_2O$ films, *Journal of the American Chemical Society*, 2012, **134**, 7231-7234.

46. K. D. Yang, W. R. Ko, J. H. Lee, S. J. Kim, H. Lee, M. H. Lee and K. T. Nam, Morphology-directed selective production of ethylene or ethane from $CO_2$ on a Cu mesopore electrode, *Angewandte Chemie*, 2017, **129**, 814-818.

47. C. Reller, R. Krause, E. Volkova, B. Schmid, S. Neubauer, A. Rucki, M. Schuster and G. Schmid, Selective electroreduction of $CO_2$ toward ethylene on nano dendritic copper catalysts at high current density, *Advanced Energy Materials*, 2017, **7**, 1602114.

48. R. Reske, H. Mistry, F. Behafarid, B. Roldan Cuenya and P. Strasser, Particle size effects in the catalytic electroreduction of $CO_2$ on Cu nanoparticles, *Journal of the American Chemical Society*, 2014, **136**, 6978-6986.

49. B. Qiao, A. Wang, X. Yang, L. F. Allard, Z. Jiang, Y. Cui, J. Liu, J. Li and T. Zhang, Single-atom catalysis of CO oxidation using $Pt_1/FeO_x$, *Nature Chemistry*, 2011, **3**, 634-641.

50. M. Jia, Q. Fan, S. Liu, J. Qiu and Z. Sun, Single-atom catalysis for electrochemical $CO_2$ reduction, *Current Opinion in Green and Sustainable Chemistry*, 2019, **16**, 1-6.

51. A. Wang, J. Li and T. Zhang, Heterogeneous single-atom catalysis, *Nature Reviews Chemistry*, 2018, **2**, 65-81.

52. X. Li, X. Yang, Y. Huang, T. Zhang and B. Liu, Supported noble-metal single atoms for heterogeneous catalysis, *Advanced Materials*, 2019, **31**, 1902031.

53. L. Liu and A. Corma, Metal catalysts for heterogeneous catalysis: from single atoms to nanoclusters and nanoparticles, *Chemical Reviews*, 2018, **118**, 4981-5079.

54. Y. Peng, B. Lu and S. Chen, Carbon-supported single atom catalysts for electrochemical energy conversion and storage, *Advanced Materials*, 2018, **30**, 1801995.

55. R. Qin, P. Liu, G. Fu and N. Zheng, Strategies for stabilizing atomically dispersed metal catalysts, *Small Methods*, 2018, **2**, 1700286.

56. H. Zhang, G. Liu, L. Shi and J. Ye, Single-atom catalysts: emerging multifunctional materials in heterogeneous catalysis, *Advanced Energy Materials*, 2018, **8**, 1701343.

57. B. Lu, Q. Liu and S. Chen, Electrocatalysis of single-atom sites: impacts of atomic coordination, *ACS Catalysis*, 2020, **10**, 7584-7618.

58. C. Zhu, S. Fu, Q. Shi, D. Du and Y. Lin, Single-atom electrocatalysts, *Angewandte Chemie International Edition*, 2017, **56**, 13944-13960.

59. M. Sharma, J. H. Jang, D. Y. Shin, J. A. Kwon, D. H. Lim, D. Choi, H. Sung, J. Jang, S. Y. Lee and K. Y. Lee, Work function-tailored graphene via transition metal encapsulation as a highly active and durable catalyst for the oxygen reduction reaction, *Energy & Environmental Science*, 2019, **12**, 2200-2211.

60. D. Xie, Y. Chen, D. Yu, S. Han, J. Song, Y. Xie, F. Hu, L. Li and S. Peng, Single-layer carbon-coated FeCo alloy nanoparticles embedded in single-walled carbon nanotubes for high oxygen electrocatalysis, *Chemical Communications*, 2020, **56**, 6842-6845.

61. T. Wang, Q. Zhao, Y. Fu, C. Lei, B. Yang, Z. Li, L. Lei, G. Wu and Y. Hou, Carbon-rich nonprecious metal single atom electrocatalysts for $CO_2$ reduction and hydrogen evolution, *Small Methods*, 2019, **3**, 1900210.

62. Y. Cheng, S. Zhao, B. Johannessen, J. P. Veder, M. Saunders, M. R. Rowles, M. Cheng, C. Liu, M. F. Chisholm and R. De Marco, Atomically dispersed transition metals on carbon nanotubes with ultrahigh loading for selective electrochemical carbon dioxide reduction, *Advanced Materials*, 2018, **30**, 1706287.

63. X. Li, W. Bi, M. Chen, Y. Sun, H. Ju, W. Yan, J. Zhu, X. Wu, W. Chu and C. Wu, Exclusive Ni-$N_4$ sites realize near-unity CO selectivity for electrochemical $CO_2$ reduction, *Journal of the American Chemical Society*, 2017, **139**, 14889-14892.

64. F. Pan, H. Zhang, K. Liu, D. Cullen, K. More, M. Wang, Z. Feng, G. Wang, G. Wu and Y. Li, Unveiling active sites of $CO_2$ reduction on nitrogen-coordinated and atomically dispersed iron and cobalt catalysts, *ACS Catalysis*, 2018, **8**, 3116-3122.

65. Y. Ye, F. Cai, H. Li, H. Wu, G. Wang, Y. Li, S. Miao, S. Xie, R. Si and J. Wang, Surface functionalization of ZIF-8 with ammonium ferric citrate toward high exposure of Fe-N active sites for efficient oxygen and carbon dioxide electroreduction, *Nano Energy*, 2017, **38**, 281-289.

66. H. Zhong, F. Meng, Q. Zhang, K. Liu and X. Zhang, Highly efficient and selective $CO_2$ electro-reduction with atomic Fe-CN hybrid coordination on porous carbon nematosphere, *Nano Research*, 2019, **12**, 2318-2323.

67. H. B. Yang, S. F. Hung, S. Liu, K. Yuan, S. Miao, L. Zhang, X. Huang, H. Y. Wang, W. Cai and R. Chen, Atomically dispersed Ni (I) as the active site for electrochemical $CO_2$ reduction, *Nature Energy*, 2018, **3**, 140-147.

68. Q. Jia, N. Ramaswamy, H. Hafiz, U. Tylus, K. Strickland, G. Wu, B. Barbiellini, A. Bansil, E. F. Holby and P. Zelenay, Experimental observation of redox-induced Fe-N switching behavior as a determinant role for oxygen reduction activity, *ACS Nano*, 2015, **9**, 12496-12505.

69. J. X. Wu, S. Z. Hou, X. D. Zhang, M. Xu, H. F. Yang, P. S. Cao and Z. Y. Gu, Cathodized copper porphyrin metal-organic framework nanosheets for selective formate and acetate production from $CO_2$ electroreduction, *Chemical Science*, 2019, **10**, 2199-2205.

70. J. Li, P. Yan, K. Li, J. You, H. Wang, W. Cui, W. Cen, Y. Chu and F. Dong, Cu supported on polymeric carbon nitride for selective $CO_2$ reduction into $CH_4$: a combined kinetics and thermodynamics investigation, *Journal of Materials Chemistry A*, 2019, **7**, 17014-17021.

71. Y. Jiao, Y. Zheng, P. Chen, M. Jaroniec and S. Z. Qiao, Molecular scaffolding strategy with synergistic active centers to facilitate electrocatalytic $CO_2$ reduction to hydrocarbon/alcohol, *Journal of the American Chemical Society*, 2017, **139**, 18093-18100.

72. J. P. Jones, G. S. Prakash and G. A. Olah, Electrochemical CO2 reduction: recent advances and current trends, *Israel Journal of Chemistry*, 2014, **54**, 1451-1466.

73. Y. Ying, X. Luo, J. Qiao and H. Huang, "More is different:" synergistic effect and structural engineering in double-atom catalysts, *Advanced Functional Materials*, 2021, **31**, 2007423.

74. Y. Pan, C. Zhang, Z. Liu, C. Chen and Y. Li, Structural regulation with atomic-level precision: From single-atomic site to diatomic and atomic interface catalysis, *Matter*, 2020, **2**, 78-110.

75. D. Chen, Z. Chen, Z. Lu, J. Tang, X. Zhang and C. V. Singh, Computational screening of homo and hetero transition metal dimer catalysts for reduction of $CO_2$ to $C_2$ products with high activity and low limiting potential, *Journal of Materials Chemistry A*, 2020, **8**, 21241-21254.

76. Y. Zhao, S. Zhou and J. Zhao, Selective C−C Coupling by spatially confined dimeric metal centers, *Iscience*, 2020, **23**, 101051.

77. S. Chen, H. Yuan, S. I. Morozov, L. Ge, L. Li, L. Xu and W. A. Goddard, Design of a graphene nitrene two-dimensional catalyst heterostructure providing a well-defined site

accommodating one to three metals, with application to $CO_2$ reduction electrocatalysis for the two-metal case, *The Journal of Physical Chemistry Letters*, 2020, **11**, 2541-2549.

78. A. Guan, Z. Chen, Y. Quan, C. Peng, Z. Wang, T. K. Sham, C. Yang, Y. Ji, L. Qian and X. Xu, Boosting $CO_2$ electroreduction to $CH_4$ via tuning neighboring single-copper sites, *ACS Energy Letters*, 2020, **5**, 1044-1053.

79. Y. Li, S. H. Chan and Q. Sun, Heterogeneous catalytic conversion of $CO_2$: a comprehensive theoretical review, *Nanoscale*, 2015, **7**, 8663-8683.

80. C. T. Dinh, T. Burdyny, M. G. Kibria, A. Seifitokaldani, C. M. Gabardo, F. P. García De Arquer, A. Kiani, J. P. Edwards, P. De Luna, O. S. Bushuyev, C. Zou, R. Quintero-Bermudez, Y. Pang, D. Sinton and E. H. Sargent, $CO_2$ electroreduction to ethylene via hydroxide-mediated copper catalysis at an abrupt interface, *Science*, 2018, **360**, 783-787.

81. K. Shin, D. H. Kim, S. C. Yeo and H. M. Lee, Structural stability of AgCu bimetallic nanoparticles and their application as a catalyst: a DFT study, *Catalysis Today*, 2012, **185**, 94-98.

82. J. K. Nørskov, J. Rossmeisl, A. Logadottir, L. Lindqvist, J. R. Kitchin, T. Bligaard and H. Jonsson, Origin of the overpotential for oxygen reduction at a fuel-cell cathode, *The Journal of Physical Chemistry B*, 2004, **108**, 17886-17892.

83. W. M. Haynes, *CRC handbook of chemistry and physics*, CRC press, 2014.

84. G. Kresse and J. Hafner, Ab initio molecular dynamics for liquid metals, *Physical Review B*, 1993, **47**, 558-561.

85. G. Kresse and J. Furthmüller, Efficient iterative schemes for ab initio total-energy calculations using a plane-wave basis set, *Physical Review B*, 1996, **54**, 11169-11186.

86. G. Kresse and D. Joubert, From ultrasoft pseudopotentials to the projector augmented-wave method, *Physical Review B*, 1999, **59**, 1758-1775.

87. J. P. Perdew, K. Burke and M. Ernzerhof, Generalized gradient approximation made simple, *Physical Review Letters*, 1996, **77**, 3865-3868.

88. A. Tkatchenko and M. Scheffler, Accurate molecular Van Der Waals interactions from ground-state electron density and free-atom reference data, *Physical Review Letters*, 2009, **102**, 073005.

89. K. Mathew, R. Sundararaman, K. Letchworth-Weaver, T. Arias and R. G. Hennig, Implicit solvation model for density-functional study of nanocrystal surfaces and reaction pathways, *The Journal of Chemical Physics*, 2014, **140**, 084106.

90. K. Mathew, V. C. Kolluru, S. Mula, S. N. Steinmann and R. G. Hennig, Implicit self-consistent electrolyte model in plane-wave density-functional theory, *The Journal of Chemical Physics*, 2019, **151**, 234101.

# Chapter 3: $CO_2$ Reduction by Single Copper Atom Supported on g-$C_3N_4$ with Asymmetrical Active Sites

## 3.1 Introduction and Significance

In this chapter, single atom Cu supported on graphitic carbon nitride (Cu-$C_3N_4$) has been studied as an electrocatalyst for the generation of high-value $C_2$ products for $CO_2$ reduction by providing asymmetrical active sites. The reaction pathways for ethylene production on the three active sites of Cu-$C_3N_4$ (Cu, C, and N) were explored based on Density Functional Theory (DFT) computations. The possible coupling of seven reaction intermediates, 17 reaction pathways, and three combinations of different active sites (Cu, C, and N) were analysed to form a thorough C-C coupling network to ethylene production. The most favourable reaction pathway to ethylene production is 1.08 eV at open circuit conditions, which is benefited by the synergistic effect of both Cu and C active sites. Comparing with other pathways utilizing Cu/N and C/N active sites, the carbon atom provides a perfect settling centre for the first $CO_2$ after reduction by Cu and leaves Cu vacant for the second $CO_2$ reduction. Our study provides reaction mechanism insights for $C_2$ production on Cu-$C_3N_4$ and sheds light on designing electrocatalysts with dual active sites. We achieved the research objectives 1.2.1 and 1.2.2 as we obtained 17 reaction pathways to ethylene on the surface of Cu-$C_3N_4$ and the synergetic effect between Cu and the substrate g-$C_3N_4$ was studied in detail by analysing the reaction mechanisms of Cu/C reaction pathways.

The highlights of this Chapter include:

- Reaction mechanisms for $C_2H_4$ production on Cu-$C_3N_4$ were studied thoroughly, 17 possible pathways are investigated.
- The asymmetrical active sites enable $C_2$ production from CRR.

- The combination of Cu /C as active sites present a higher activity than Cu/N from the thermodynamic perspectives.

### 3.2 $CO_2$ Reduction by Single Copper Atom Supported on g-$C_3N_4$ with Asymmetrical Active Sites

This Chapter is included as it appears as a journal paper published by **Sijia Fu**, Xin Liu, Jingrun Ran, Yan Jiao, Shi-Zhang Qiao, $CO_2$ Reduction by Single Copper Atom Supported on g-$C_3N_4$ with Asymmetrical Active Sites. Applied Surface Science, 2021, 540, 148293.

# Statement of Authorship

| | |
|---|---|
| Title of Paper | $CO_2$ Reduction by Single Copper Atom Supported on g-$C_3N_4$ with Asymmetrical Active Sites |
| Publication Status | ☑ Published ☐ Accepted for Publication<br>☐ Submitted for Publication ☐ Unpublished and Unsubmitted w ork w ritten in manuscript style |
| Publication Details | Fu, Sijia, Xin Liu, Jingrun Ran, Yan Jiao, and Shi-Zhang Qiao. "$CO_2$ reduction by single copper atom supported on g-$C_3N_4$ with asymmetrical active sites." *Applied Surface Science* 540 (2021): 148293. |

## Principal Author

| | | | |
|---|---|---|---|
| Name of Principal Author (Candidate) | Sijia Fu | | |
| Contribution to the Paper | Research plan, computation calculations, most of the characterizations and data analysis, and manuscript draft. | | |
| Overall percentage (%) | 70 | | |
| Certification: | This paper reports on original research I conducted during the period of my Higher Degree by Research candidature and is not subject to any obligations or contractual agreements with a third party that would constrain its inclusion in this thesis. I am the primary author of this paper. | | |
| Signature | | Date | 12/03/2021 |

## Co-Author Contributions

By signing the Statement of Authorship, each author certifies that:

i. the candidate's stated contribution to the publication is accurate (as detailed above);

ii. permission is granted for the candidate in include the publication in the thesis; and

iii. the sum of all co-author contributions is equal to 100% less the candidate's stated contribution.

| | | | |
|---|---|---|---|
| Name of Co-Author | Xin Liu | | |
| Contribution to the Paper | manuscript draft | | |
| Signature | | Date | 12/03/2021 |

| | | | |
|---|---|---|---|
| Name of Co-Author | Jingrun Ran | | |
| Contribution to the Paper | Supervision of the work, discussion of this manuscript and manuscript evaluation. | | |
| Signature | | Date | 12/03/2021 |

| | |
|---|---|
| Name of Co-Author | Yan Jiao |

| | | | |
|---|---|---|---|
| Contribution to the Paper | Supervision of the work, discussion of this manuscript and manuscript evaluation. | | |
| Signature | | Date | 17/03/2021 |

| | | | |
|---|---|---|---|
| Name of Co-Author | Shi-Zhang Qiao | | |
| Contribution to the Paper | Discussion of this manuscript and manuscript evaluation. | | |
| Signature | | Date | 17/03/2021 |

Please cut and paste additional co-author panels here as required.

Applied Surface Science 540 (2021) 148293

Contents lists available at ScienceDirect

Applied Surface Science

journal homepage: www.elsevier.com/locate/apsusc

# $CO_2$ reduction by single copper atom supported on g-$C_3N_4$ with asymmetrical active sites

Sijia Fu [1], Xin Liu [1], Jingrun Ran, Yan Jiao [*], Shi-Zhang Qiao

*Centre for Materials in Energy and Catalysis, The University of Adelaide, South Australia 5005, Australia*
*School of Chemical Engineering and Advanced Materials, The University of Adelaide, South Australia 5005, Australia*

ARTICLE INFO

*Keywords:*
$CO_2$ reduction
Single atom catalyst
Asymmetrical active sites
$C_2$ production
Density functional theory

ABSTRACT

Electrochemical reduction of $CO_2$ requires catalysts beyond Cu with high activity and selectivity to produce $C_2$ products. Different from many single-atom catalysts that show high performance in obtaining $C_1$ products, Cu supported on carbon nitride (Cu-$C_3N_4$) has shown a unique capability to generate $C_2$ products by providing asymmetrical active sites. Herein, we study 17 possible pathways and reaction mechanisms of $CO_2$ reduction toward ethylene – a featured $C_2$ product, on Cu-$C_3N_4$. The possible reaction intermediates along with different reaction pathways on three active sites of Cu-$C_3N_4$ (Cu, C, and N) were obtained by density functional theory (DFT) computations. The most probable reaction pathway toward $C_2H_4$ production is 1.08 eV at open circuit conditions, which is benefited by the synergistic effect of both Cu and C active sites. Comparing with other pathways utilizing Cu/N and C/N active sites, the carbon atom provides a perfect settling centre for the first $CO_2$ after reduction by Cu and leaves Cu vacant for the second $CO_2$ reduction. Our study provides reaction mechanism insights for $C_2$ production on Cu-$C_3N_4$ and sheds light on designing electrocatalysts with dual active sites.

## 1. Introduction

Because of the excessive carbon dioxide ($CO_2$) emission caused by intensive consumption of fossil fuels, the reduction of $CO_2$ into alternative value-added fuels is a promising method to alleviate greenhouse effect and positively affect the global carbon balance [1,2]. However, the reduction of $CO_2$ to fuels is challenging as $CO_2$ molecule is stable and unreactive [1,3]. The electrochemical $CO_2$ reduction reaction (CRR) holds great promise attributing to its mild reaction conditions and potential controlled product selectivity [4–6]. One of the major challenges in this area is the design of the catalysts with high activity and selectivity to certain products [7,8]. $C_2$ products are generally regarded as more economically valuable than $C_1$ products because of their higher volumetric energy densities and their importance in the synthesis of long-chain hydrocarbon fuels [9]. However, the C—C bond formation process is a critical challenge in the catalysis process and the whole reaction is suffering from low selectivity and high over potential caused by the competition with C—O, C—H bond formations or competitive hydrogen evolution reaction (HER) [10–12]. As a result, the major CRR products for most metallic catalysts are $C_1$ hydrocarbons (*e.g.*, CO and HCOOH) [4,13,14] Although copper has proved to be able to produce $C_1$, $C_2$, and $C_3$ products, the types of high-performance catalysts are still limited [15–17].

In recent years, single-atom catalysts (SACs) have been applied in many catalytic reactions. This is mainly attributed to the high utilization rate of metal atoms as active centres, as well as favourable electronic structure alternation of SAC due to strong interactions between the embedded metal atoms and the substrates [18–22]. SACs have attracted increasing interests in the application of CRR, and showed enhanced activity and selectivity since 2015 [23–25]. For example, by introducing atomic Fe to nitrogen-doped porous carbon nematosphere (NPCN), a lower theoretical onset potential for CO production can be obtained as the formation of the intermediates can be promoted by Fe, resulting in Faradaic efficiency (FE) for CO reaches up to 94% at −0.5 V vs. RHE [26]. However, most SACs only show activity towards $C_1$ products such as CO and HCOOH during CRR. Similarly, Ni SACs supported on nitrogen doped carbon was reported to achieve a CO production FE of 96.5% and current density of 36 mA $cm^{-2}$ at an overpotential of 0.61 V [27], and a Co-$N_5$ SAC showed CO production FE of 99.2% and current density of 6.2 mA $cm^{-2}$ at low potential of −0.73 V vs. RHE [28]. However, previous reports on SAC for electrochemical $CO_2$ reduction mainly limited to transition metals. More recently, it was found that main group

* Corresponding author.
*E-mail address:* yan.jiao@adelaide.edu.au (Y. Jiao).
[1] These authors contributed equally to this work.

https://doi.org/10.1016/j.apsusc.2020.148293
Received 7 September 2020; Received in revised form 25 October 2020; Accepted 27 October 2020
Available online 2 November 2020

element like indium (In) with exclusive $In^{\delta+}$-$N_4$ interface on metal-organic frameworks (MOFs) derived N-doped carbon matrix (In-SAs/NC) could achieve a formate production FE of 96% and current density of 8.87 mA $cm^{-2}$ at low potential of −0.65 V vs. RHE owing to the $In^{\delta+}$-$N_4$ interface active sites [29]. By now, most SACs only show activity towards $C_1$ products such as CO and HCOOH during CRR. This high selectivity toward CO might be attributed to that these SACs only contain one active site and can only effectively stabilize *CO. Hence, the possibility of generating $C_2$ products is limited. The application of the molecular framework supported SACs is a possible solution to boost $CO_2$ reduction to $C_2$ products by providing a second active site for C—C coupling. More isolated mixed metal sites supported on carbon materials can be constructed based on MOF [30]. Recently, a Cu-$C_3N_4$ SAC was found to generate detectable $C_2$ products, including $C_2H_4$, $C_2H_6$, and $C_2H_5OH$ [31]. Through loading metals on g-$C_3N_4$, high metal loading amount and appropriate coordination ability can be achieved, which can be served as desirable $CO_2$RR electrocatalysts with promising performance [32,33]. One reaction pathway for $C_2H_5OH$ production involving Cu and C as active sites has been explored in the past. However, complicated reaction networks, as well as the combinations of different active sites, are not systematically studied in previous works. Hence, it is still not clear that whether Cu/C is the best combination and there is not enough evidence in the past to prove the advantage of Cu/C, which prevents us to understand the problem further.

The understanding of the systematic effect of dual active sites of single Cu atom catalyst supported on g-$C_3N_4$ can give answers to the above doubts. Therefore, in the present work, we employed extensive DFT calculations to explore various C—C coupling pathways on different combination of Cu/C/N active sites. $C_2H_4$ was selected as a representative $C_2$ product because of its essential role in the chemical and fuels industries (*e.g.*, plastic production). More importantly, it could serve as a model product to explore the reaction mechanisms and can be expanded to other $C_2$ species formation. Our extensive computation indicated that 17 possible reaction pathways exist for $C_2H_4$ production on Cu-$C_3N_4$. Furthermore, the lowest free energy changes for these pathways were summarized, and further analysed from the charge transfer perspective. Our work provides both reaction pathway level and electronic level insights for $C_2$ production on Cu-$C_3N_4$. In addition, it can serve as a reference for designing more electrocatalysts with dual active sites, such as metal-organic-framework-based SACs [34].

## 2. Models and methods

The models were built based on graphitic carbon nitride (g-$C_3N_4$), with one copper atom embedded in the cavity. The optimized lattice parameter for Cu-$C_3N_4$ is 7.089 × 7.089 × 20.000 Å, and the angle between the first two vectors is 120°. As shown in Fig. 1a, the carbon and nitrogen sites of the Cu-$C_3N_4$ substrate and the copper atom are all considered as active sites. All combinations with these possible intermediates ($C_xH_yO_z$) on these active sites are considered to form a comprehensive C—C coupling network.

Density functional theory (DFT) methods were used to carry out the electronic structure calculations through the Perdew-Burke-Ernzerhof (PBE) exchange-correlation functional in Vienna Ab Initio Simulation Package (VASP) [35–39]. The kinetic energy cutoff is set to be 500 eV for the plane-wave expansion after testing several cutoff energies. The convergence criterion for electronic structure iteration is $10^{-5}$ eV, and that for geometry optimization is 0.01 eV/Å. A 5 × 5 × 1 Γ-centred Monkhorst-Pack k-point mesh was used for Cu-$C_3N_4$. Considering the van der Waals interactions between atoms, the Tkatchenko-Scheffler method was applied for all calculations [40].

The computational hydrogen electrode method (CHE) was used for the calculation of the Gibbs free energy during the $CO_2$ reduction process [41]. The free energy of the electron-proton pair ($H^+ + e^-$) can be referenced to the chemical potential of gaseous $H_2$ under standard conditions (0 V vs standard hydrogen electrode, at 101,325 Pa). The

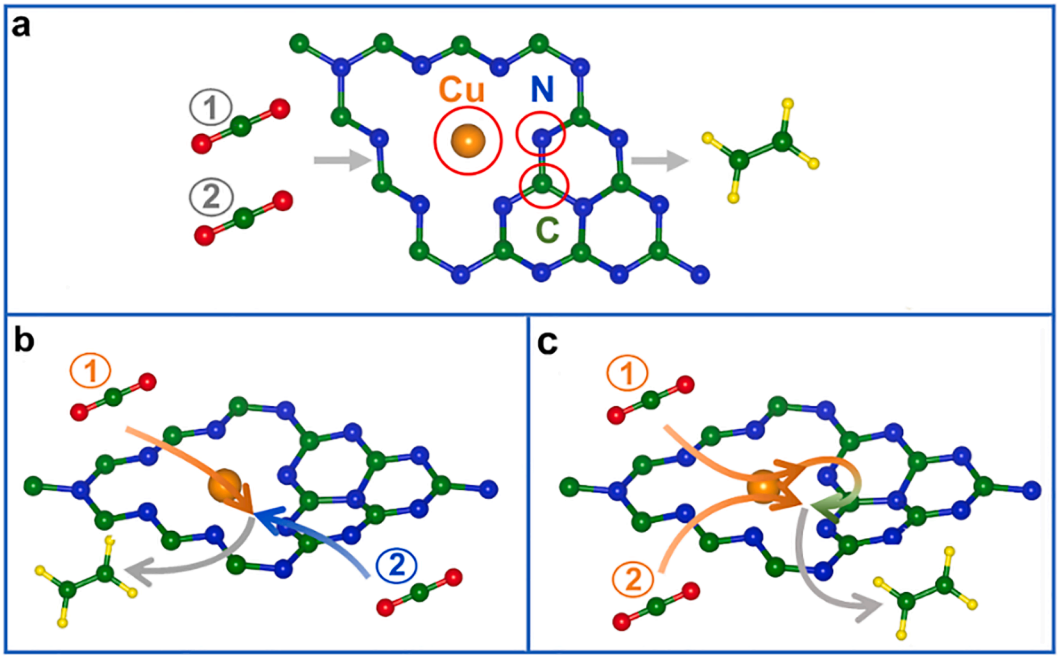


**Fig. 1.** (a) Illustration of the electrocatalyst, reactant, and product in this study. Three active sites on the surface of Cu-$C_3N_4$ were investigated, including the copper atom, the pyridinic atom at the edge of g-$C_3N_4$, and the carbon atom connecting two pyridinic nitrogen. Reactants are two $CO_2$ molecules (as displayed in the figure), proton sourced from the electrolyte, and electron from the electrode (the latter two are not displayed). Product is one ethylene molecule. (b) The reaction mechanism based on the combination of copper and nitrogen atoms as active sites. The reaction starts with the protonation of the first $CO_2$ on the copper site. The following step is the protonation of the second $CO_2$ on the pyridinic nitrogen site. C—C coupling process is based on Cu/N. (c) The reaction mechanisms based on the combination of copper and carbon atom as active sites. The reaction starts with the protonation of the first $CO_2$ on the copper site, and the reduced intermediate is transferred to the carbon site. The following step is the protonation of the second $CO_2$ on the vacant copper site. C—C coupling process is based on Cu/C. Colour code: C green, N blue, Cu gold, O red, H yellow.

Gibbs free energy calculation is using the formula expressed as follows,

$$G = E - TS + ZPE + \int C_p dT \quad (1)$$

in which *E* indicates the electronic energy obtained by DFT calculations. *TS* and *ZPE* indicate entropy and zero-point energy corrections, and *T* is the room temperature (*T* = 298.15 K). *ZPE* and vibrational entropy of adsorbed species were obtained once vibrational frequencies were calculated. Entropies of gas molecules ($H_2$ and $CO_2$) were taken from standard values [42]. The free energy corrections for gas-phase properties of the critical reaction intermediates are summarized in Table S1 of the Supporting Information (SI).

For the electron density difference calculation, the formula used is expressed as follows,

$$\rho_{diff} = \rho_{total} - \rho_{Cu-C_3N_4} - \rho_{*COOH+*OCH_2} \quad (2)$$

in which $\rho_{diff}$ indicates the electron density difference before and after the inclusion of intermediates atoms. $\rho_{total}$, $\rho_{Cu-C_3N_4}$ and $\rho_{*COOH+*OCH_2}$ indicates the electron density of the total adsorption configuration, the substrate Cu-$C_3N_4$, and the adsorbed intermediates, respectively.

The overall reaction of $CO_2$ reduction to form $C_2H_4$ on the Cu-$C_3N_4$ in the presence of hydrogen is expressed in the following formula and the reaction includes 12 elementary hydrogenation steps [43].

$$2CO_2(g) + 8H_2O(l) + 12e^- \rightarrow C_2H_4(g) + 12OH^-$$

$$E^0_{C_2H_4} = -0.764\ V \quad vs. \quad SHE \quad (3)$$

The overall reaction of $CO_2$ reduction to form CO on the Cu-$C_3N_4$ in the presence of hydrogen is expressed in the following formula and the reaction includes 2 elementary hydrogenation steps [43].

$$CO_2(g) + 2H_2O(l) + 2e^- \rightarrow CO(g) + 2OH^-$$

$$E^0_{CO} = -0.934\ V \quad vs. \quad SHE \quad (4)$$

Solvation calculations for selected $C_2H_4$ pathways (pathway 3 and 10) and CO pathway were performed using VASPsol, in which the solvation energies are modelled on periodic systems [44,45].

## 3. Results and discussion

At the starting point of $CO_2$ reduction, the first elementary step is $CO_2$ protonation to *COOH; for this step, three possible active sites exist, which are Cu, C, N. Through DFT simulations and Gibbs free energy calculation, it has been found that the free energy required for the protonation of $CO_2$ to form *COOH on copper site is 0.37 eV, while that on nitrogen site is 1.47 eV - nearly four times compared with Cu. Cu here has a better $CO_2$ activation ability than N site on Cu-$C_3N_4$. Although the adsorption of $CO_2$ on g-$C_3N_4$ is limited, the attachment of Cu can enhance the $CO_2$ adsorption performance [46]. We considered carbon site for $CO_2$ protonation as well, and the free energy required is 0.43 eV. However, for carbon as the active site for $CO_2$ activation, it is difficult to identify a C—C coupling pathway later on. Therefore, for Cu-$C_3N_4$, only Cu and N are considered as the active sites for $CO_2$ protonation. The brief reaction mechanisms for Cu/N and Cu/C are shown in Fig. 1b and c.

To demonstrate the complex reaction networks and how the thermodynamics of these reaction pathways change, we classify these pathways according to the intermediates involved for C—C coupling and the sites where the coupling takes place - because it is known that C—C coupling step is crucial for $C_2$ production and usually determines the overall selectivity. The pathways can be grouped as those adopt Cu/N as dual active sites (pathways 1–2, 4–5, 7–16), and those adopt Cu/C as dual active sites (pathway 3 and 6). The main difference for these pathways is the C—C coupling steps which involve various intermediates as shown in Table 1 (for example, for pathway 1, the C—C coupling step is between N*CHO and Cu*CO). The free energy change of potential determining step (PDS) on each coupling pathway are summarized in Fig. 2. In addition, the detailed values for the free energy change are included in Table S2.

**Table 1**
Summary of C—C coupling network on active sites of Cu-$C_3N_4$, including intermediates and the related active sites.[a]

| Active Sites | | Cu* | | | | | | |
|---|---|---|---|---|---|---|---|---|
| *Intermediates* | | *CO* | *CHO* | *COOH* | *$OCH_2$* | *CHOH* | *CH* | *$CH_2$* |
| N* | *CHO* | **1** | **4** | **7** | **9** | **11** | — | — |
| | *COOH* | — | **5** | — | **10** | **12** | **14** | **15** |
| | *CHOH* | **2** | — | **8** | — | **13** | — | **16** |
| C | *$OCH_2$* | **3** | **6** | — | — | — | — | — |

[a] The bold numbers are the index of different pathways. * indicates the active sites for $CO_2$ protonation.

As shown in Table 1, the intermediates before C—C coupling step for each pathway are listed as well as the active sites. The results indicated that although the active sites for most of the reaction pathways (14 pathways) are the combination of Cu and N, 3rd and 6th pathway with Cu and C as the active sites feature lower free energy changes. In addition, the combination of C and N can provide an additional pathway (the 17th pathway). However, on this 17th pathway, the protonation of the second $CO_2$ is considered not facile due to lacking bond formation between adsorbate and catalyst. More detail for the 17th pathway is included in SI, and the free energy diagram is shown in Fig. S1.

We first carefully compared the Cu/N cases and found that for the C—C coupling step, the first $CO_2$ always tends to be reduced on Cu site and form intermediates like *CH, *$CH_2$, *CO, *CHO, *COOH, or *CHOH. The protonation of the second $CO_2$ then takes place on N site. However, this second protonation step is found to be the PDS with at least a free energy change of 1.40 eV (9th and 10th pathway). Afterwards, for Cu/C cases, namely the 3rd and 6th pathway, the lowest free energy change of 0.96 eV under the vacuum environment was detected. This value was the best one among all cases for Cu-$C_3N_4$, and is comparable with $C_2H_4$ pathway on Cu (1 0 0) [47]. In general, based on the analysis of potential determining steps along with their free energy change, we concluded that Cu/C showed a better synergistic effect than Cu/N and presented a comparable activity with Cu (1 0 0).

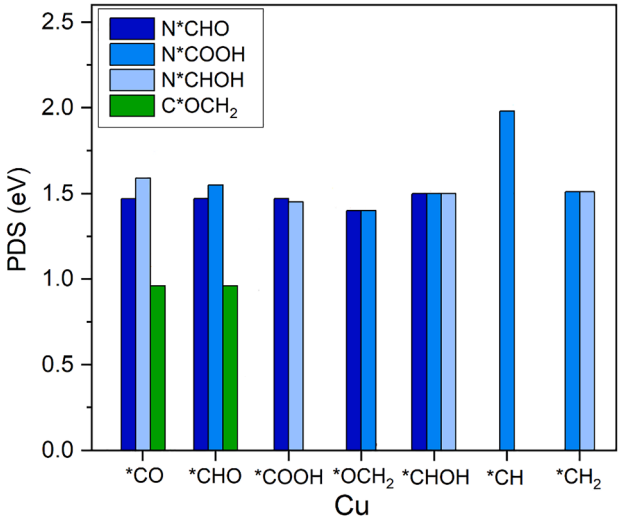


**Fig. 2.** Summary of the different highest free energy change for different pathways. Highest free energy change can be used to evaluate the activity of different pathways. Cu*$C_xH_yO_z$ is regarded as one of the intermediates for C—C coupling. Pathway 1 to 16 are shown from left to right. N*CHO/N*COOH/N*CHOH/C*$OCH_2$ is another intermediate for C—C coupling. Some Cu*$C_xH_yO_z$ reaction intermediates do not have N*CHO/N*COOH/N*CHOH/C*$OCH_2$ bars because these combinations cannot form stable C—C bond.

To further elucidate why Cu/C showed a better synergistic effect, in the following sections, we focused on specific pathways as shown in Fig. 3. The 3rd and 10th pathways were chosen as they were the ones with the lowest free energy change for Cu/C and Cu/N, respectively. The free energies for the intermediates involved in these two pathways were further calculated under the solvation environment for a more realistic result. The results show that the highest free energy change for pathway 3 after considering solvation effect is 1.08 eV, and that for pathway 10 is 1.22 eV. The following analysis of Fig. 3 will be consistent with the reaction sequence, starting from the protonation of the first $CO_2$, then the protonation of the second $CO_2$, finally the C—C coupling process. The optimized configurations of intermediates with the lowest free energy in the above processes at each step are demonstrated in Fig. S2. The reaction free energy profiles for other pathways are shown in Fig. S3–16.

The reduction processes for the first $CO_2$ on pathway 3 and pathway 10 are nearly the same. These two pathways share the same first three proton-electron pair transfer steps, as shown in Fig. 2 (from step 1 to step 4). All these three hydrogenation steps occur on the copper site due to the high $CO_2$ activation activity of Cu. In addition, the reaction pathways both proceed through the CHO intermediate (0.92 eV), which is regarded as the key step to open the hydrocarbon-forming reaction pathways [41]. We considered the formation of *COH from the hydrogenation of *CO as well, and the potential required for that step is 3 eV, which makes it impossible from the thermodynamic aspect. Then, the two pathways start to diverge from the fourth proton-electron pair transfer. The *CHO intermediate (step 4) is protonated to form $*OCH_2$ (step 5a and 5b), with oxygen as the anchoring atom on the surface of the catalyst. However, $*OCH_2$ is still adsorbed on the copper site for step 5b (Cu/N pathway). For step 5a (Cu/C pathway), $*OCH_2$ is adsorbed on the carbon site on g-$C_3N_4$ network. The existence of carbon atom of g-$C_3N_4$ substrate provides a perfect settling site for the first reduced $CO_2$ intermediate from the copper site. The transfer of the active centre indicates Cu and C act in synergy. We considered *COOH, *CO and *CHO go through similar transfers, but the C site cannot stabilize these intermediates. The carbon species has been proven to show a strong affinity to oxygen-containing reaction intermediates (such as $*OCH_2$, $*OCH_3$, *O and *OH), which favours further reduction during CRR as oxygen-bound reaction intermediates are always required during the late stage to obtain $C_2/C_3$ products [8].

The next step on the reaction pathway is the protonation of the second $CO_2$, and two pathways are using different active sites for this step. In pathway 3, after the binding atom for the first reduced $CO_2$ intermediate ($*OCH_2$) is transferred from Cu to C, the copper site is vacant, which allows the protonation of the second $CO_2$ molecule occurs on Cu again to form *COOH. Hence the PDS can be reduced effectively by using copper to reduce two $CO_2$ due to the better $CO_2$ activation ability of copper. The second *COOH formation is energetically different from the first one, although they are both generated from the reduction of $CO_2$ on copper. The free energy change for the formation of the 2nd *COOH is 0.59 eV downhill, while that for the 1st *COOH is 0.01 downhill. On the other hand, the adsorption configurations are also different; Cu not only binds the carbon atom from the second *COOH,

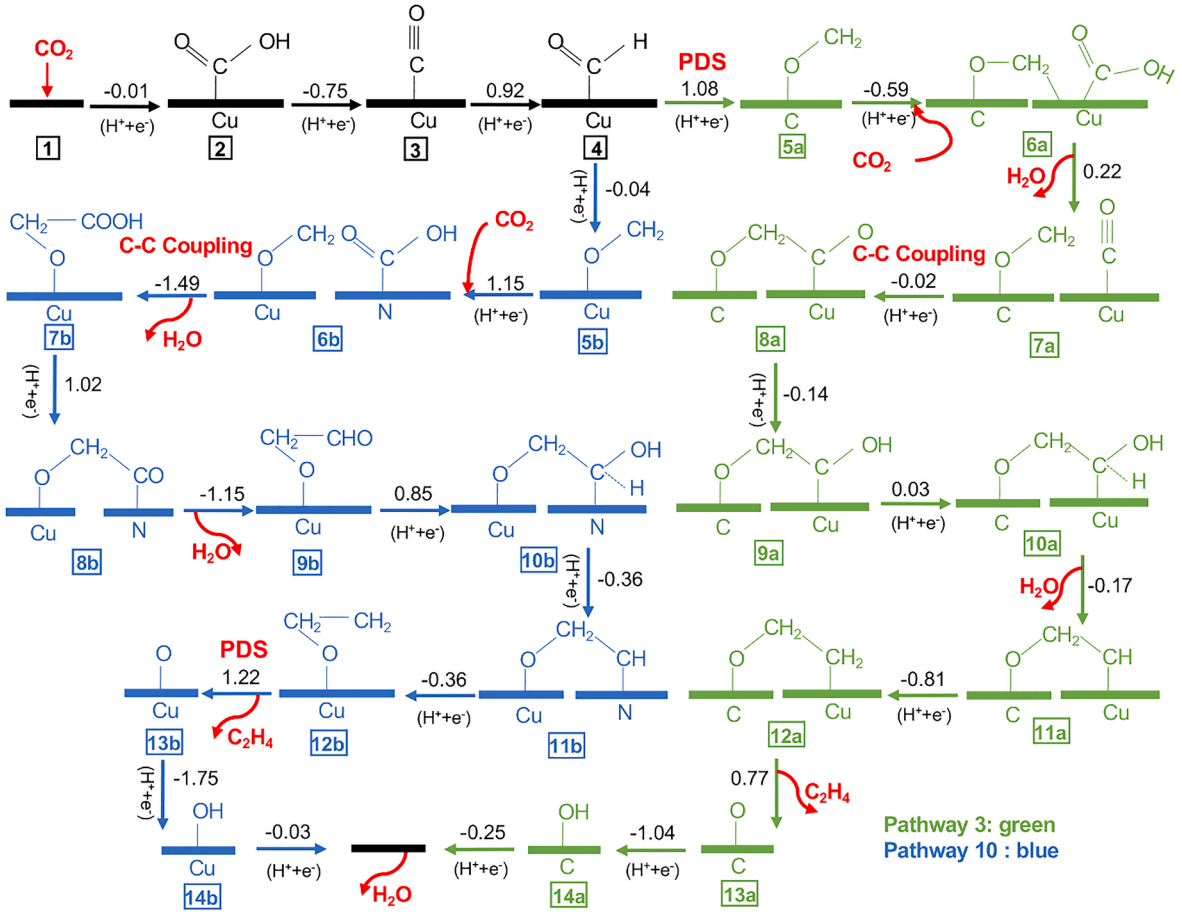


**Fig. 3.** Complete reaction network of pathway 3 (Cu/C, marked by green colour) and pathway 10 (Cu/N, marked by blue colour) for $CO_2$ electroreduction to $C_2H_4$ on the surface of Cu-$C_3N_4$. These two pathways share a common route until step 5; for pathway 3 the active centre changes from copper to the adjacent carbon atom with a free energy change of 1.08 eV, leaving the copper atom serving as an active centre for the second $CO_2$ activation. For pathway 10 the active centre (for the first $CO_2$ molecule) remains to be copper, and the pyridinic nitrogen activates the second $CO_2$ molecule. Calculated Gibbs free energies (eV) are marked as the numbers parallel to reaction arrows.

but also binds the carbon atom from *$OCH_2$ in 6a at this time. This can be explained by the strong affinity of Cu towards carbon atom of the reaction intermediates. Because of the existence of *$OCH_2$ on C, the protonation of the 2nd $CO_2$ actually is easier. In addition, the interaction between *$OCH_2$ and *COOH also avoids desorption of *$OCH_2$ forming formaldehyde (HCHO), which helps reserve it for the following C—C coupling step. In pathway 10, the reduction of the second $CO_2$ occurs on the nitrogen atom on the g-$C_3N_4$ network (step 6b), leaving *$OCH_2$ binding with Cu. This step requires 1.15 eV uphill free energy change, which is close to the PDS for this pathway (1.22 eV). Following analysis from charge transfer aspects would explain why N atom is not capable of activating $CO_2$.

As previously discussed, the free energy change for the protonation of the second $CO_2$ on Cu site of pathway 3 is 0.59 eV downhill. However, the free energy for this step of pathway 10 is 1.4 eV uphill, involving N as the active site. Cu here has a better $CO_2$ activation ability than N site. To further elucidate the difference, we calculated the electron density difference caused by the adsorption process and Bader charge. The results are summarized in Fig. 4. More electrons (0.728 $e^-$) are transferred from Cu-$C_3N_4$ to the adsorbed intermediates for 3rd pathway based on Bader charge analysis, which could be a piece of evidence for the stabilization of the intermediates. What's more, we also found electron accumulation between *$OCH_2$ and *COOH (Fig. 4a), which may further benefit C—C coupling between the two intermediates. However, for pathway 10, the transferred charge is only 0.040 $e^-$, and there is no significant electron transfer between *$OCH_2$ and *COOH as shown in Fig. 4b. The analysis showed that Cu/C dual active sites (as in Pathway 3) could effectively stabilize the resulting intermediates of C—C coupling. In addition, we also found that for 3rd pathway (Cu/C), C site loses 1.520 $e^-$, while for 10th pathway (Cu/N), the N site gains 1.021 $e^-$. The high electronegativity of N (3.04) results in its high ability to capture electrons [42]. However, the active sites should provide electrons for intermediates to form stable interaction. Therefore, the C site can provide electrons to the intermediates due to its moderate electronegativity (2.55), and this can explain why the intermediates can be effectively stabilized by Cu/C [42]. Therefore, atoms with relatively weak electronegativity are considered as more suitable for CRR.

For the C—C coupling step, which is the core step towards $C_2H_4$ product, pathway 3 holds *$OCH_2$ on C site while *CO on Cu site, and a C—C bond was formed between the carbon atoms of these two intermediates. This coupling process is not very challenging because the reasonable distance between C and Cu (varying from 2.5 to 3.5 Å) in the configuration of Cu-$C_3N_4$ benefits the formation of *$OCH_2CO$* (O—C bond: 1.4 Å, C—C bond: 1.6 Å). Furthermore, from step 8a to step 12a, the intermediates all have Cu and C as two anchoring/active sites, and the change of the free energies among these steps is neither significant nor positive, indicating these steps are easy to happen. For pathway 10, step 7b is the C—C coupling step, and *$OCH_2COOH$ is formed from *$OCH_2$ (initiated on Cu) and *COOH (initiated on N), and finally bonded with Cu. The intermediates involving Cu/N are formed across the boundary of Cu-$C_3N_4$ instead of in the void of one Cu-$C_3N_4$. The detailed structures, such as 8b can be found in Fig. S2. Among these steps, the free energy change for step 8b and step 10b is still relatively high compared with the insignificant free energy change of pathway 3. Therefore, the performance of Cu/N is not satisfactory.

Gibbs free energies of the reaction intermediates in the process of $CO_2$ reduction on the surface of Cu-$C_3N_4$ for pathway 3 and pathway 10 are summarized in Fig. 5 to provide a direct impression of the free energy change, as well as the PDS differences for the two pathways. The detailed status of every step after ($H^+$+$e^-$) transfer of these two pathways are shown in Table S3 (pathway 3) and Table S4 (pathway 10). In addition, as CO was experimentally reported to be one of the main products on Cu-$C_3N_4$ [31], we also investigated CO production on Cu-$C_3N_4$ for comparison purposes. The Gibbs free energy pathway for CO generation is presented in Fig. 5. In this Figure, the PDS for CO formation is the desorption of CO, which is 0.97 eV. This value is slightly higher than the formation of *CHO of the $C_2H_4$ pathway (0.92 eV). Moreover, the smallest PDS for $C_2H_4$ formation is 1.08 eV, which is close to the PDS for CO formation.

As shown in Fig. 5, the PDS for pathway 3 is the formation of *$OCH_2$ on C site, which shows a 1.08 eV uphill free energy change. This value is only 0.16 eV higher than the formation of *CHO, the sharing step for both pathways. The results also indicated that the coupling intermediates are effectively stabilized by the dual sites of Cu-$C_3N_4$ so that the coupling step is not the PDS. Pathway 10 shares the first $CO_2$ protonation step with pathway 3; however, the PDS for pathway 10 is the desorption of $C_2H_4$, which is 1.22 eV uphill. Therefore, with regard to the PDS difference between the two pathways, we focus on the study of the desorption of $C_2H_4$ to identify the underlying mechanisms.

We noted that for pathway 3, the adsorption of *$OCH_2CH_2$ takes place on both C site and Cu site, and the free energy change is 0.77 eV uphill. However, the free energy for this step of pathway 10 is 1.22 eV uphill, involving only Cu as the binding site. The electron density difference for these structures is shown in Fig. S17 and Bader charge are

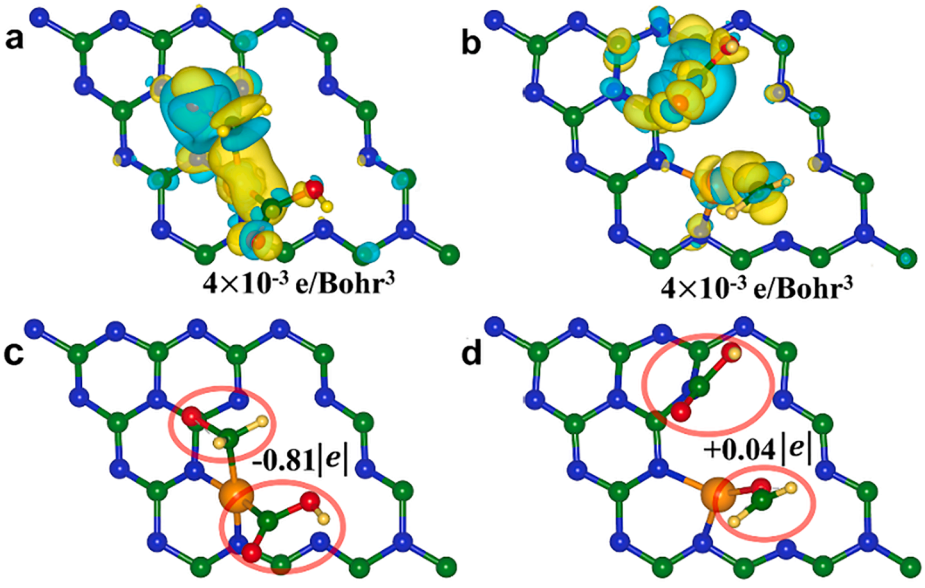


**Fig. 4.** The electron density difference for the intermediates (*$OCH_2$+*COOH) adsorbed on the surface of Cu-$C_3N_4$ in the structure of (a) C*$OCH_2$*Cu*COOH (Pathway 3) and (b) Cu*$OCH_2$ + N*COOH (Pathway 10). Yellow represents electron accumulation, and cyan denotes electron depletion. The net Bader charge value for the electrons transfers between the substrate and *$OCH_2$+*COOH in the structure of (c) C*$OCH_2$*-Cu*COOH and (d) Cu*$OCH_2$ + N*COOH. The plus/minus sign indicates that *$OCH_2$+*COOH is positively/negatively charged. Color code: C green, N blue, H yellow, O red, Cu orange. Isosurface value for both (a) and (b) are $4 \times 10^{-3}$ e/$Bohr^3$.

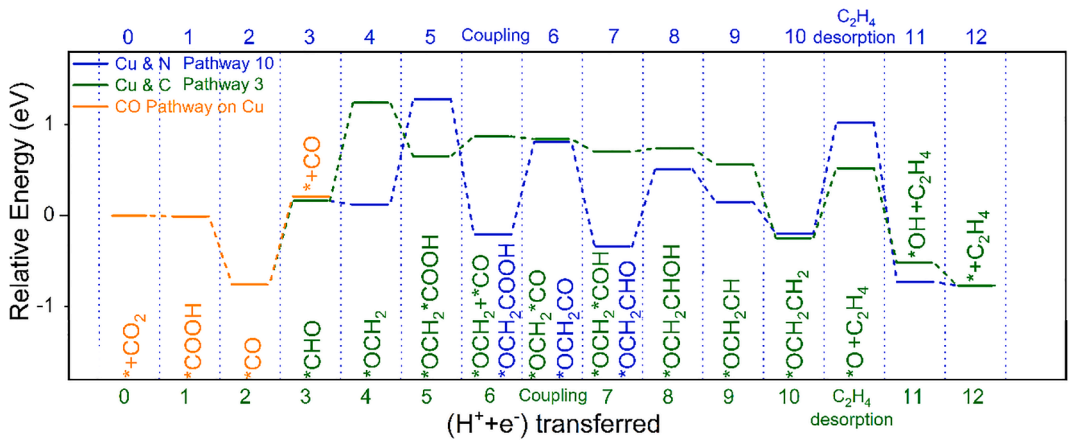


**Fig. 5.** The free energy diagram of pathway 3, pathway 10, and that of CO production. Pathway 3 and 10 show the lowest limiting potential involving Cu/C or Cu/N as active sites for $CO_2$ reduction to $C_2H_4$ on the Cu-$C_3N_4$ catalyst. Colour code: Pathway 3 (Cu & C), green; Pathway 10 (Cu & N), blue; CO pathway on Cu, orange.

summarized in Fig. 6 to further analyse the phenomenon. Fig. 6a and b provide the top views for structure 12a ($C^*OCH_2CH_2$) and 12b ($Cu^*OCH_2CH_2$). As shown in Fig. 6c, the intermediate $C_2H_4$ losses 0.32 $e^-$ for 3rd pathway based on Bader charge analysis. For pathway 10, $C_2H_4$ losses 0.70 $e^-$. The desorption of $C_2H_4$ in pathway 10 is harder than that in pathway 3 because of the strong bond effect between $C_2H_4$ and O atom. In addition, the easier desorption of $C_2H_4$ in pathway 3 can be ascribed to the synergetic work of Cu and C as well. In pathway 3, the final reaction intermediate ($^*OC_2H_4$) is bonded with both C and Cu site. The $C_2H_4$ moiety is connected to the C site of g-$C_3N_4$ via the O atom (O—C1 bond length: 1.43 Å; O—C2 bond length: 1.47 Å), and is also connected to the single Cu atom site via a Cu—C bond (bond length: 1.97 Å). While for pathway 10, the $C_2H_4$ moiety only has one strong bond with the O atom anchoring with Cu site (O—Cu bond length: 1.83 Å). In addition, the bond length between O atom and $C_2H_4$ is 1.37 Å. Both of these bond length values for pathway 10 are shorter than that for pathway 3, indicating a stronger interaction for the pathway 10, which is in line with a larger amount of charge transfer for pathway 10 (0.70 $e^-$) compared with pathway 3 (0.32 $e^-$). Therefore, the moderate binding between the substrate and the adsorbate for pathway 3 benefits the desorption of the product.

## 4. Conclusions

The mechanism for electrochemical reduction of $CO_2$ to $C_2H_4$ on Cu-$C_3N_4$ model catalyst was studied in detail by using the DFT methods. We established various reaction pathways towards $C_2H_4$ on this asymmetric framework Cu-$C_3N_4$. The synergistic effect of dual sites was extensively studied based on the whole reaction networks. We found that Cu/C sites presented a higher performance (1.08 eV for PDS) from thermodynamic perspectives. Further analysis from the charge transfer process explained Cu/C could not only help stabilize the coupling intermediates but also keep the binding effect to a moderate level, and thus show better activity. Our study proves the peculiarity of g-$C_3N_4$ as molecular scaffold for single atom catalyst: which is providing an extra active centre for the CRR and can enhance $CO_2$ reduction to $C_2H_4$ and, possibly, other $C_2$ species. Furthermore, we conclude that we can enable $C_2$ production for CRR by using a framework with good catalytic activity.

### CRediT authorship contribution statement

**Sijia Fu:** Methodology, Investigation, Data curation, Formal analysis, Writing - original draft. **Xin Liu:** Methodology, Investigation, Data curation, Writing - original draft. **Jingrun Ran:** Writing - review &

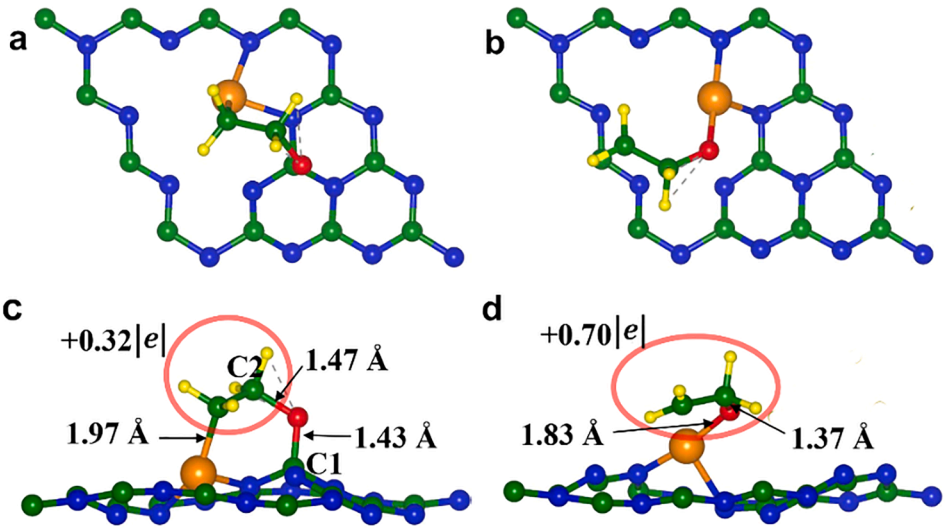


**Fig. 6.** The top views and side views for the key reaction intermediates (a)(c) $C^*OCH_2CH_2{}^*Cu$ (on Pathway 3) and (b)(d) $Cu^*OCH_2CH_2$ (on Pathway 10). The bond length and net Bader charge value for the electrons transfers between intermediates and the substrate are displayed in (c)(d). The plus sign indicates that $^*CH_2CH_2$ is positively charged. Colour code: C green, N blue, H yellow, O red, Cu orange.

editing. **Yan Jiao:** Conceptualization, Resources, Supervision, Writing - review & editing. **Shizhang Qiao:** Conceptualization, Supervision, Writing - review & editing.

## Declaration of Competing Interest

The authors declare that they have no known competing financial interests or personal relationships that could have appeared to influence the work reported in this paper.

## Acknowledgements

This research is supported by the Australian Research Council through these programs (FT190100636 and DP190103472). DFT computations for this research were undertaken with the assistance of supercomputing resources provided by the Phoenix HPC service at the University of Adelaide and the resources and services from the National Computational Infrastructure (NCI) supported by the Australian Government.

## Appendix A. Supplementary material

Supplementary data to this article can be found online at https://doi.org/10.1016/j.apsusc.2020.148293.

## References

[1] E.E. Benson, C.P. Kubiak, A.J. Sathrum, J.M. Smieja, Electrocatalytic and homogeneous approaches to conversion of CO 2 to liquid fuels, Chem. Soc. Rev. 38 (2009) 89–99.
[2] C.W. Li, J. Ciston, M.W. Kanan, Electroreduction of carbon monoxide to liquid fuel on oxide-derived nanocrystalline copper, Nature 508 (2014) 504–507.
[3] C.W. Li, M.W. Kanan, CO2 reduction at low overpotential on Cu electrodes resulting from the reduction of thick Cu2O films, J. Am. Chem. Soc. 134 (2012) 7231–7234.
[4] J.P. Jones, G.S. Prakash, G.A. Olah, Electrochemical CO2 reduction: recent advances and current trends, Isr. J. Chem. 54 (2014) 1451–1466.
[5] D.T. Whipple, P.J. Kenis, Prospects of CO2 utilization via direct heterogeneous electrochemical reduction, J. Phys. Chem. Lett. 1 (2010) 3451–3458.
[6] D.D. Zhu, J.L. Liu, S.Z. Qiao, Recent advances in inorganic heterogeneous electrocatalysts for reduction of carbon dioxide, Adv. Mater. 28 (2016) 3423–3452.
[7] A. Vasileff, Y. Zheng, S.Z. Qiao, Carbon solving carbon's problems: recent progress of nanostructured carbon-based catalysts for the electrochemical reduction of CO2, Adv. Energy Mater. 7 (2017) 1700759.
[8] Y. Zheng, A. Vasileff, X. Zhou, Y. Jiao, M. Jaroniec, S.-Z. Qiao, Understanding the roadmap for electrochemical reduction of CO2 to multi-carbon oxygenates and hydrocarbons on copper-based catalysts, J. Am. Chem. Soc. 141 (2019) 7646–7659.
[9] A.J. Garza, A.T. Bell, M. Head-Gordon, Mechanism of CO2 reduction at copper surfaces: pathways to C2 products, ACS Catal. 8 (2018) 1490–1499.
[10] M. Jouny, W. Luc, F. Jiao, High-rate electroreduction of carbon monoxide to multi-carbon products, Nat. Catal. 1 (2018) 748–755.
[11] A. Loiudice, P. Lobaccaro, E.A. Kamali, T. Thao, B.H. Huang, J.W. Ager, R. Buonsanti, Tailoring copper nanocrystals towards C2 products in electrochemical CO2 reduction, Angewandte Chemie Int. Ed. 55 (2016) 5789–5792.
[12] Q. Fan, M. Zhang, M. Jia, S. Liu, J. Qiu, Z. Sun, Electrochemical CO2 reduction to C2+ species: heterogeneous electrocatalysts, reaction pathways, and optimization strategies, Mater. Today Energy 10 (2018) 280–301.
[13] S. Liu, H. Yang, X. Huang, L. Liu, W. Cai, J. Gao, X. Li, T. Zhang, Y. Huang, B. Liu, Identifying active sites of nitrogen-doped carbon materials for the CO2 reduction reaction, Adv. Funct. Mater. 28 (2018) 1800499.
[14] Y. Hori, A. Murata, R. Takahashi, S. Suzuki, Electrochemical reduction of carbon monoxide to hydrocarbons at various metal electrodes in aqueous solution, Chem. Lett. 16 (1987) 1665–1668.
[15] K.P. Kuhl, E.R. Cave, D.N. Abram, T.F. Jaramillo, New insights into the electrochemical reduction of carbon dioxide on metallic copper surfaces, Energy Environ. Sci. 5 (2012) 7050–7059.
[16] Y.i. Hori, Electrochemical CO 2 reduction on metal electrodes, in: Modern Aspects of Electrochemistry, Springer, 2008, pp. 89–189.
[17] L. Zhang, Z.J. Zhao, J. Gong, Nanostructured materials for heterogeneous electrocatalytic CO2 reduction and their related reaction mechanisms, Angewandte Chemie Int. Ed. 56 (2017) 11326–11353.
[18] M. Jia, Q. Fan, S. Liu, J. Qiu, Z. Sun, Single-atom catalysis for electrochemical CO2 reduction, Curr. Opin. Green Sustain. Chem. 16 (2019) 1–6.
[19] A. Wang, J. Li, T. Zhang, Heterogeneous single-atom catalysis, Nat. Rev. Chem. 2 (2018) 65–81.
[20] X. Liu, Y. Jiao, Y. Zheng, M. Jaroniec, S.-Z. Qiao, Building up a picture of the electrocatalytic nitrogen reduction activity of transition metal single-atom catalysts, J. Am. Chem. Soc. 141 (2019) 9664–9672.
[21] Y. Zhou, G. Gao, J. Kang, W. Chu, L.-W. Wang, Transition metal-embedded two-dimensional C 3 N as a highly active electrocatalyst for oxygen evolution and reduction reactions, J. Mater. Chem. A 7 (2019) 12050–12059.
[22] X. Liu, Y. Jiao, Y. Zheng, K. Davey, S.-Z. Qiao, A computational study on Pt and Ru dimers supported on graphene for the hydrogen evolution reaction: new insight into the alkaline mechanism, J. Mater. Chem. A 7 (2019) 3648–3654.
[23] Y. Cheng, S. Yang, S.P. Jiang, S. Wang, Supported single atoms as new class of catalysts for electrochemical reduction of carbon dioxide, Small Methods 3 (2019) 1800440.
[24] A.S. Varela, N. Ranjbar Sahraie, J. Steinberg, W. Ju, H.S. Oh, P. Strasser, Metal-doped nitrogenated carbon as an efficient catalyst for direct CO2 electroreduction to CO and hydrocarbons, Angewandte Chemie Int. Ed. 54 (2015) 10758–10762.
[25] J.-H. Liu, L.-M. Yang, E. Ganz, Efficient and selective electroreduction of CO2 by single-atom catalyst two-dimensional TM–Pc monolayers, ACS Sustain. Chem. Eng. 6 (2018) 15494–15502.
[26] H. Zhong, F. Meng, Q. Zhang, K. Liu, X. Zhang, Highly efficient and selective CO 2 electro-reduction with atomic Fe-CN hybrid coordination on porous carbon nematosphere, NANO Res. 12 (2019) 2318–2323.
[27] H.B. Yang, S.-F. Hung, S. Liu, K. Yuan, S. Miao, L. Zhang, X. Huang, H.-Y. Wang, W. Cai, R. Chen, Atomically dispersed Ni (I) as the active site for electrochemical CO 2 reduction, Nat. Energy 3 (2018) 140–147.
[28] Y. Pan, R. Lin, Y. Chen, S. Liu, W. Zhu, X. Cao, W. Chen, K. Wu, W.-C. Cheong, Y. Wang, Design of single-atom Co–N5 catalytic site: a robust electrocatalyst for CO2 reduction with nearly 100% CO selectivity and remarkable stability, J. Am. Chem. Soc. 140 (2018) 4218–4221.
[29] H. Shang, T. Wang, J. Pei, Z. Jiang, D. Zhou, Y. Wang, H. Li, J. Dong, Z. Zhuang, W. Chen, Design of a single-atom indiumδ+-N4 interface for efficient electroreduction of CO2 to formate, Angewandte Chemie Int. Ed. (2020).
[30] T. Sun, L. Xu, D. Wang, Y. Li, Metal organic frameworks derived single atom catalysts for electrocatalytic energy conversion, NANO Res. (2019) 1–14.
[31] Y. Jiao, Y. Zheng, P. Chen, M. Jaroniec, S.Z. Qiao, Molecular scaffolding strategy with synergistic active centers to facilitate electrocatalytic CO2 reduction to hydrocarbon/alcohol, J. Am. Chem. Soc. 139 (2017) 18093–18100.
[32] X. Li, H. Rong, J. Zhang, D. Wang, Y. Li, Modulating the local coordination environment of single-atom catalysts for enhanced catalytic performance, NANO Res 13 (2020).
[33] Z. Jiang, T. Wang, J. Pei, H. Shang, D. Zhou, H. Li, J. Dong, Y. Wang, R. Cao, Z. Zhuang, Discovery of main group single Sb–N 4 active sites for CO 2 electroreduction to formate with high efficiency, Energy Environ. Sci. 13 (2020) 2856–2863.
[34] H.-F. Wang, L. Chen, H. Pang, S. Kaskel, Q. Xu, MOF-derived electrocatalysts for oxygen reduction, oxygen evolution and hydrogen evolution reactions, Chem. Soc. Rev. 49 (2020) 1414–1448.
[35] G. Kresse, J. Hafner, Ab initio molecular dynamics for liquid metals, Physical Review B 47 (1993) 558–561.
[36] G. Kresse, J. Furthmüller, Efficient iterative schemes for ab initio total-energy calculations using a plane-wave basis set, Phys. Rev. B 54 (1996) 11169–11186.
[37] G. Kresse, D. Joubert, From ultrasoft pseudopotentials to the projector augmented-wave method, Phys. Rev. B 59 (1999) 1758–1775.
[38] J.P. Perdew, K. Burke, M. Ernzerhof, Generalized gradient approximation made simple, Phys. Rev. Lett. 77 (1996) 3865–3868.
[39] J.P. Perdew, K. Burke, M. Ernzerhof, Generalized gradient approximation made simple [Phys. Rev. Lett. 77, 3865 (1996)], Phys. Rev. Lett. 78 (1997), 1396-1396.
[40] A. Tkatchenko, M. Scheffler, Accurate molecular Van Der Waals interactions from ground-state electron density and free-atom reference data, Phys. Rev. Lett. 102 (2009) 073005.
[41] A.A. Peterson, F. Abild-Pedersen, F. Studt, J. Rossmeisl, J.K. Norskov, How copper catalyzes the electroreduction of carbon dioxide into hydrocarbon fuels, Energy Environ. Sci. 3 (2010) 1311–1315.
[42] W.M. Haynes, CRC Handbook of Chemistry and Physics, CRC Press, 2014.
[43] A. Bard, R. Parsons, J. Jordan, Standard Potentials in Aqueous Solution, CRC Press, 1985.
[44] K. Mathew, R. Sundararaman, K. Letchworth-Weaver, T. Arias, R.G. Hennig, Implicit solvation model for density-functional study of nanocrystal surfaces and reaction pathways, J. Chem. Phys. 140 (2014) 084106.
[45] K. Mathew, V.C. Kolluru, S. Mula, S.N. Steinmann, R.G. Hennig, Implicit self-consistent electrolyte model in plane-wave density-functional theory, J. Chem. Phys. 151 (2019) 234101.
[46] Z. Sun, J.M.T.A. Fischer, Q. Li, J. Hu, Q. Tang, H. Wang, Z. Wu, M. Hankel, D. J. Searles, L. Wang, Enhanced CO2 photocatalytic reduction on alkali-decorated graphitic carbon nitride, Appl. Catal. B 216 (2017) 146–155.
[47] W. Luo, X. Nie, M.J. Janik, A. Asthagiri, Facet dependence of CO2 reduction paths on Cu electrodes, ACS Catal. 6 (2016) 219–229.

# Supporting Information

# $CO_2$ Reduction by Single Copper Atom Supported on g-$C_3N_4$ with Asymmetrical Active Sites

*Sijia Fu[†a,b], Xin Liu[†a,b], Jingrun Ran,[a,b] Yan Jiao[*a.b] and Shi-Zhang Qiao[a,b]*

[a] Centre for Materials in Energy and Catalysis, The University of Adelaide, South Australia 5005, Australia.

[b] School of Chemical Engineering and Advanced Materials, The University of Adelaide, South Australia 5005, Australia.

[†]These authors contributed equally to this work.

**This PDF file includes:**

C-C coupling on carbon and nitrogen

CO and $CO_2$ Free Energy Correction

Reaction intermediates configurations

Reaction free energy diagrams

Computed gas phase properties

Summary of highest free energy change on each pathway

Detailed status of every step after ($H^+$+$e^-$) transfer for pathway 3 and 10

**Note S1 to S2**
**Figure S1 to S17**
**Table S1 to S4**

**Note S1: C-C coupling on Carbon and Nitrogen**

C and N can work as C-C coupling sites as well and the related Gibbs free energy diagram is shown in Figure S1, referring to pathway 17. The C-C coupling sites are considered as Cu/C and Cu/N in the paper. However, the C-C coupling sites can be C and N in pathway 17, although the actives sites for $CO_2$ protonation are still Cu and N. In pathway 17, the first $CO_2$ is still protonated by Cu like the other pathways, then the intermediate is settled by C. For pathway 3 and 6, after the settling of the first reduced $CO_2$ intermediates, the second $CO_2$ protonation occurs on Cu again, resulting in a combination of Cu/C as C-C coupling sites. However, the protonation of the second $CO_2$ happens on N instead of Cu in pathway 17. The PDS of pathway 17 is the protonation of *CO to *CHO, which is the same as that of pathway 3 and 6. In conclusion, C here provides a settling point for the reaction intermediates, which benefits the protonation of the second $CO_2$.

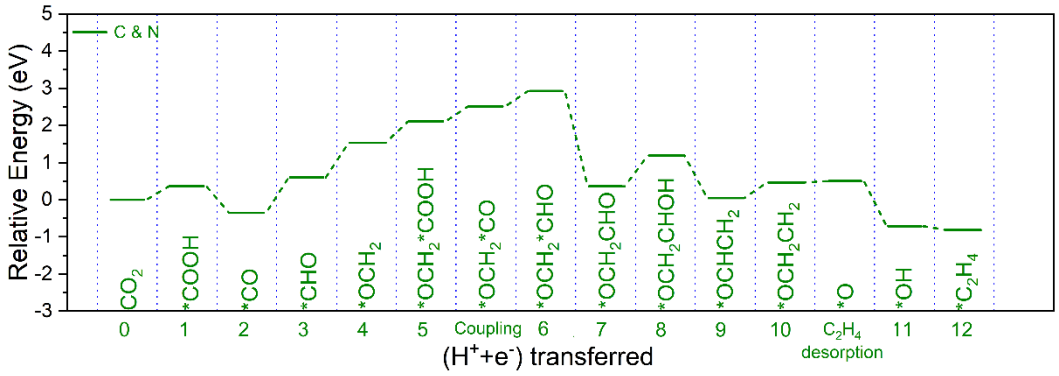


**Figure S1** Free energy diagram of $CO_2$ reduction to $C_2H_4$ for pathway 17 on Cu-$C_3N_4$.

**Note S2: CO and $CO_2$ Free Energy Correction**

Since the free energy change calculations based on CO and $CO_2$ energies obtained from direct DFT calculations are not accurate, we set the free energy of $C_2H_4$ product as reference and adopted the standard electrode potential to derive the free energy of $CO_2$(g). Afterwards, the obtained free energy of $CO_2$(g) was used to compute the that of CO(g) following empirical thermodynamics values. The equations used are as follows.

The overall reaction of $CO_2$ reduction to form $C_2H_4$ under standard conditions is expressed in the following formula and the reaction includes 12 proton-coupled electron transfer:

$$2CO_2(g) + 12H^+ + 12e^- \rightarrow C_2H_4(g) + 4H_2O(l)$$

$$E^0_{C_2H_4} = 0.064 \text{ V vs SHE} \qquad \text{(S1a) [1]}$$

Therefore, the Gibbs free energy of reaction $\Delta G(U)$ can be calculated using the following equation

$$\Delta G(U) = 12eU = (G_{C_2H_4} + 4G_{H_2O}) - (2G_{CO_2} + 12G_{H^+} + 12G_{e^-}) \quad \text{(S1b)}$$

Where U is the electrode potential under standard conditions, and G is the Gibbs free energies for $C_2H_4$(g), $H_2O$(l), $CO_2$(g), protons and electrons. Based on which, the free energy of $CO_2$(g) can be calculated as

$$G_{CO_2} = (G_{C_2H_4} + 4G_{H_2O} - 12G_{H^+} - 12G_{e^-} - 12eU)/2 \quad \text{(S1c)}$$

The overall reaction of $CO_2$ reduction to form CO is expressed in the following formula with two proton coupled electron transfer:

$$CO_2(g) + 2H^+ + 2e^- \rightarrow CO(g) + H_2O(l)$$

$$E_{CO}^{0} = -0.106 \text{ V vs SHE} \qquad \text{(S2a) [1]}$$

Therefore, the Gibbs free energy of reaction $\Delta G(U)$ can be calculated using the following equation

$$\Delta G(U) = 2eU = (G_{CO} + G_{H_2O}) - (G_{CO_2} + 2G_{H^+} + 2G_{e^-}) \quad \text{(S2b)}$$

Where U is the electrode potential under standard conditions, and G is the Gibbs free energies for CO(g), $H_2O$(l), $CO_2$(g), protons and electrons. Based on which, the free energy of CO(g) can be calculated as

$$G_{CO} = G_{CO_2} + 2G_{H^+} + 2G_{e^-} - G_{H_2O} + 2eU \quad \text{(S2c)}$$

The free energy of ($H^+$) and $H_2O$(l) involved in the above CO and $CO_2$ formulas can be obtained from the following equations.

$$(H^+ + e^-) \leftrightarrow \frac{1}{2}H_2 \quad @ \text{ 0V vs SHE} \quad \text{(S3a)}$$

$$G_{H^+} = \frac{1}{2}G_{H_2} \quad @ \text{ 0V vs SHE} \quad \text{(S3b)}$$

$$G_{e^-} = 0 \quad @ \text{ 0V vs SHE} \quad \text{(S3c)}$$

$$G_{H_2O}(l) = G_{H_2O}(g) + RT \times \ln(\frac{p}{p_0}) \quad \text{(S4)}$$

R is the ideal gas constant, T is the room temperature 298.15K, p is the fugacity of water in its liquid phase with value of 0.035 bar, and $p_0$ is the pressure of standard gas with value of 1 bar. $G_{H_2}(g)$ and $G_{H_2O}(g)$ are obtained from DFT calculations.

The calculated free energy for $G_{CO_2}$is -23.31 eV, and $G_{CO}$ is -15.38 eV.

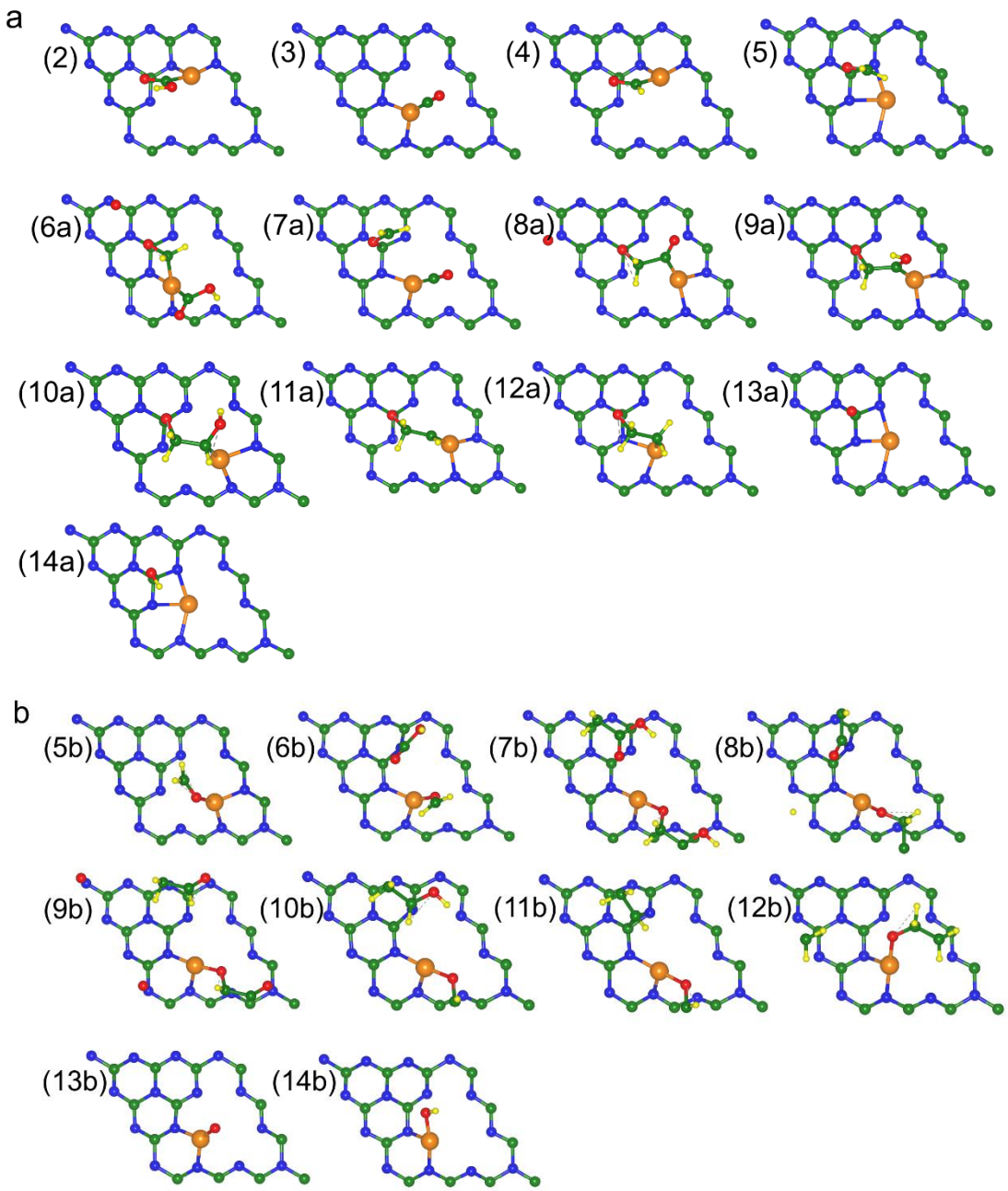


**Figure S2** Optimized configurations of the intermediates on pathway 3 (a) and pathway 10 (b). The numbers indicate the specific steps in Figure 3.

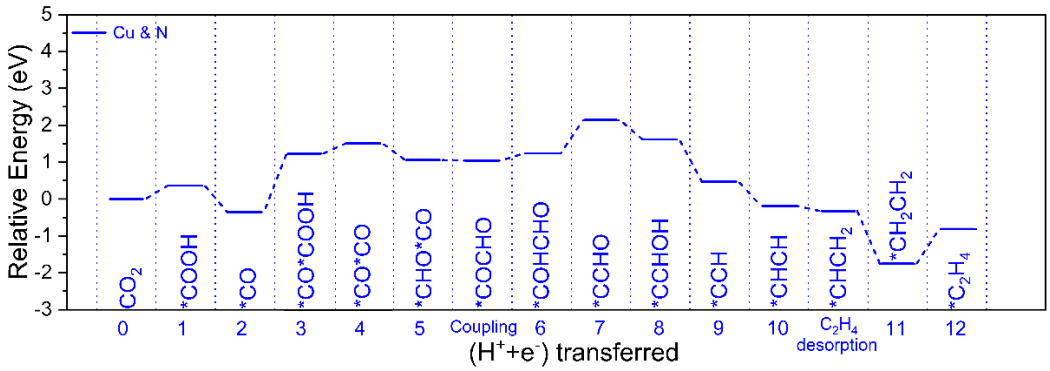


**Figure S3** Free energy diagram of $CO_2$ reduction to $C_2H_4$ for pathway 1 on Cu-$C_3N_4$.

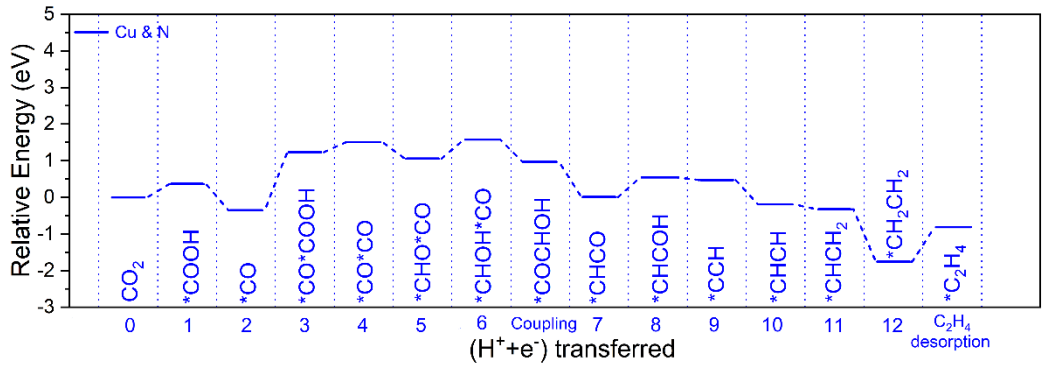


**Figure S4** Free energy diagram of $CO_2$ reduction to $C_2H_4$ for pathway 2 on Cu-$C_3N_4$.

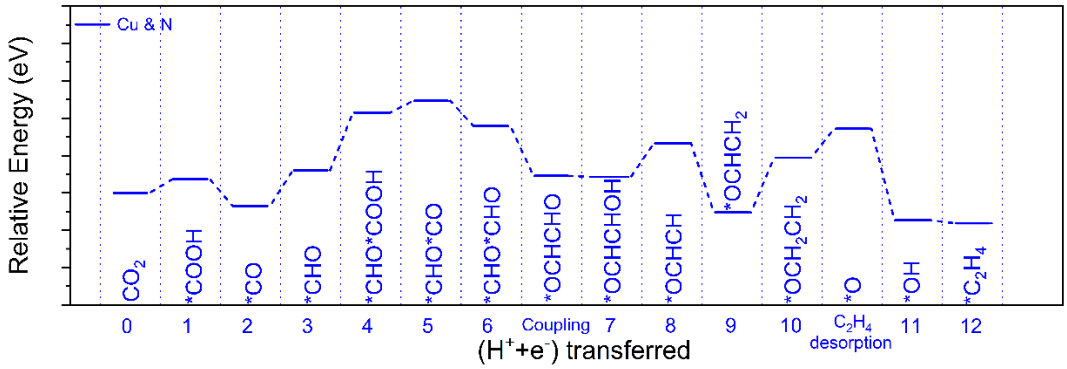


**Figure S5** Free energy diagram of $CO_2$ reduction to $C_2H_4$ for pathway 4 on Cu-$C_3N_4$.

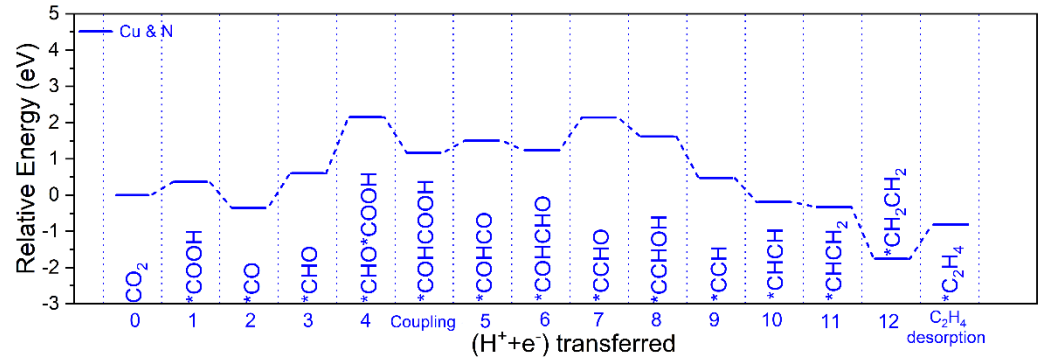


**Figure S6** Free energy diagram of $CO_2$ reduction to $C_2H_4$ for pathway 5 on Cu-$C_3N_4$.

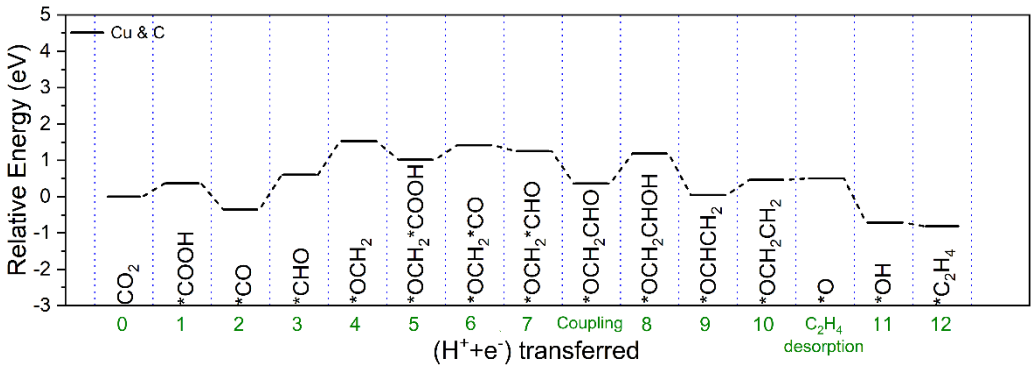


**Figure S7** Free energy diagram of $CO_2$ reduction to $C_2H_4$ for pathway 6 on Cu-$C_3N_4$.

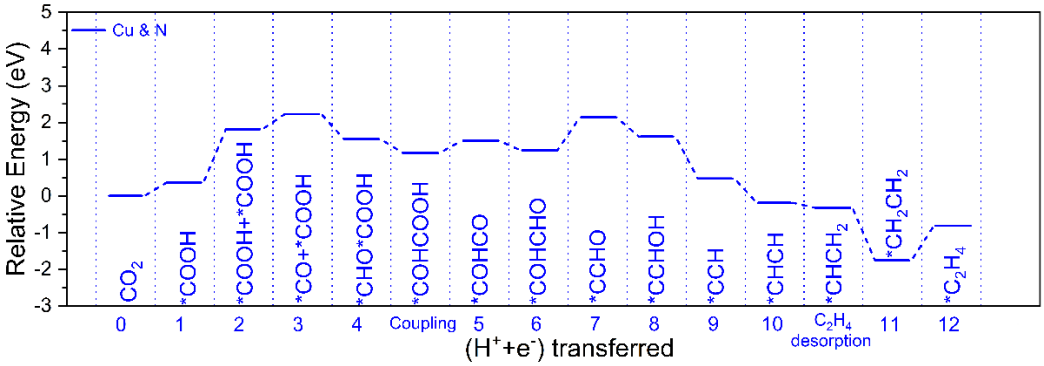


**Figure S8** Free energy diagram of $CO_2$ reduction to $C_2H_4$ for pathway 7 on Cu-$C_3N_4$.

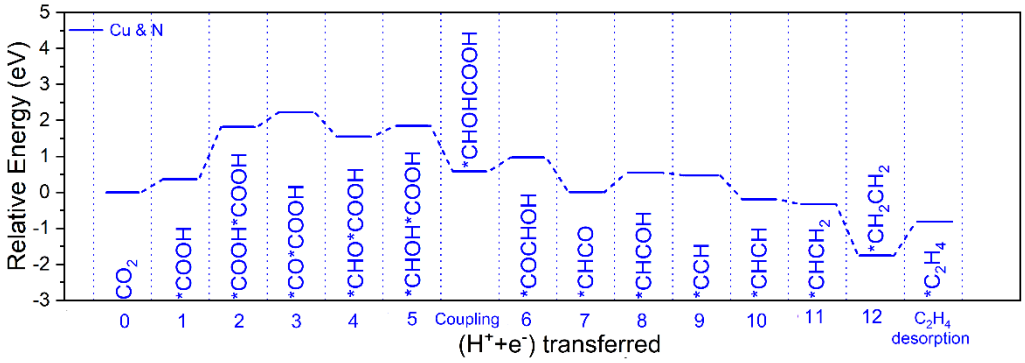


**Figure S9** Free energy diagram of $CO_2$ reduction to $C_2H_4$ for pathway 8 on Cu-$C_3N_4$.

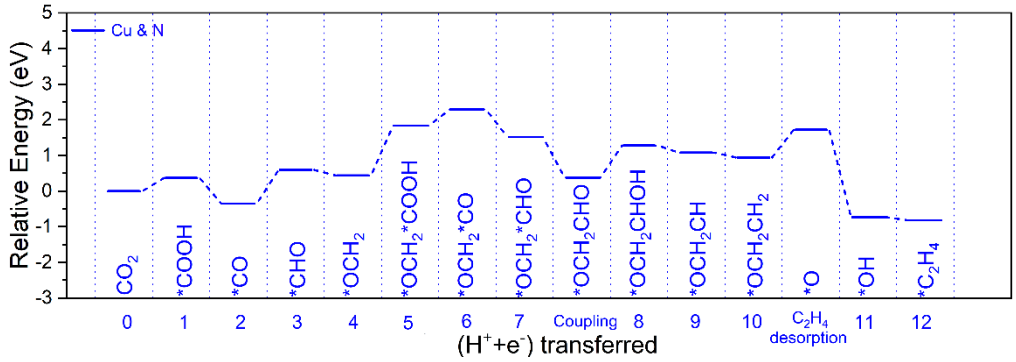


**Figure S10** Free energy diagram of $CO_2$ reduction to $C_2H_4$ for pathway 9 on Cu-$C_3N_4$.

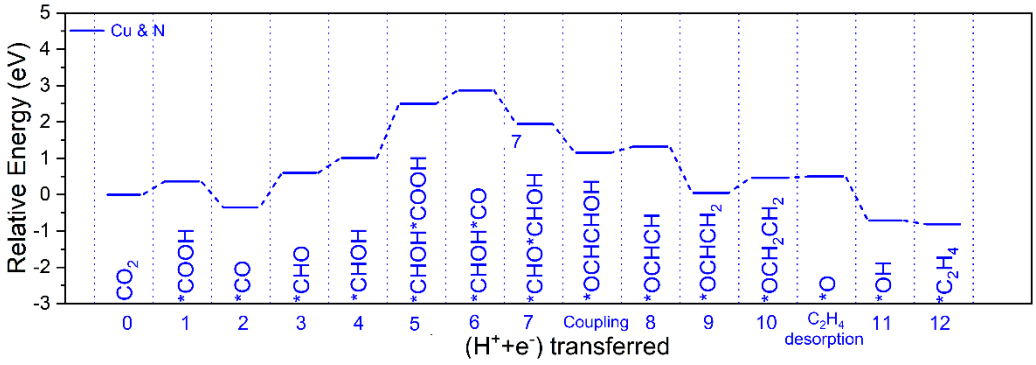


**Figure S11** Free energy diagram of $CO_2$ reduction to $C_2H_4$ for pathway 11 on Cu-$C_3N_4$.

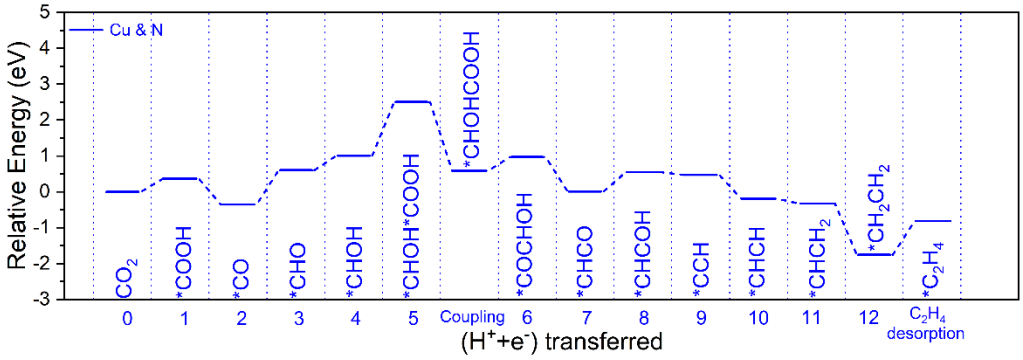


**Figure S12** Free energy diagram of $CO_2$ reduction to $C_2H_4$ for pathway 12 on Cu-$C_3N_4$.

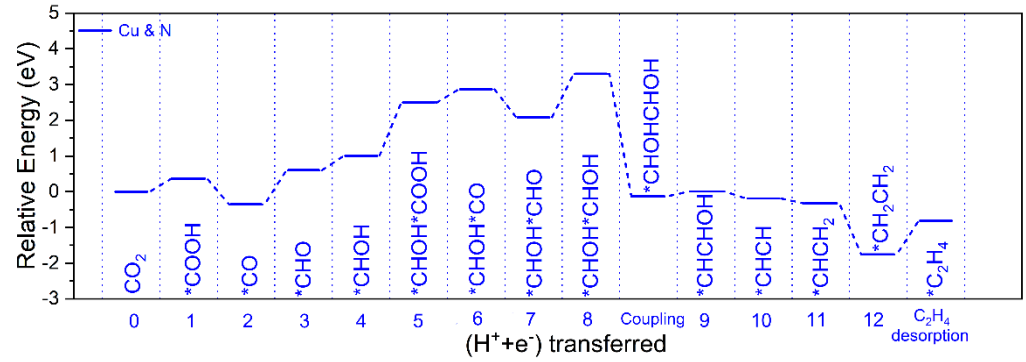


**Figure S13** Free energy diagram of $CO_2$ reduction to $C_2H_4$ for pathway 13 on Cu-$C_3N_4$.

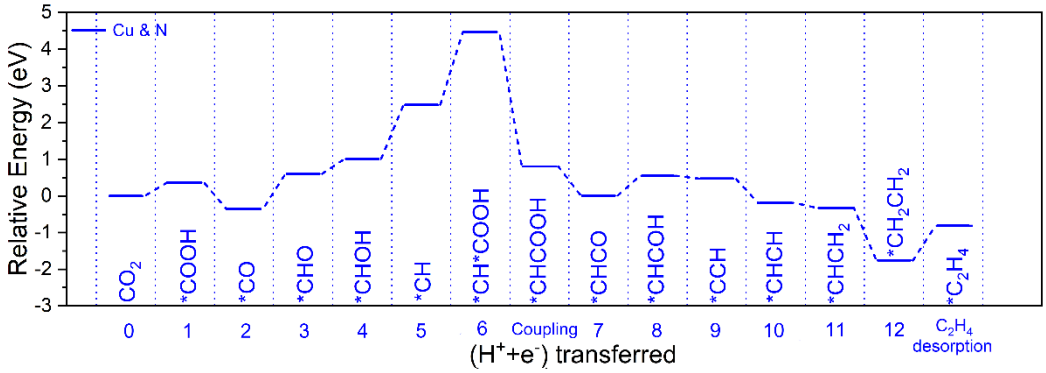


**Figure S14** Free energy diagram of $CO_2$ reduction to $C_2H_4$ for pathway 14 on Cu-$C_3N_4$.

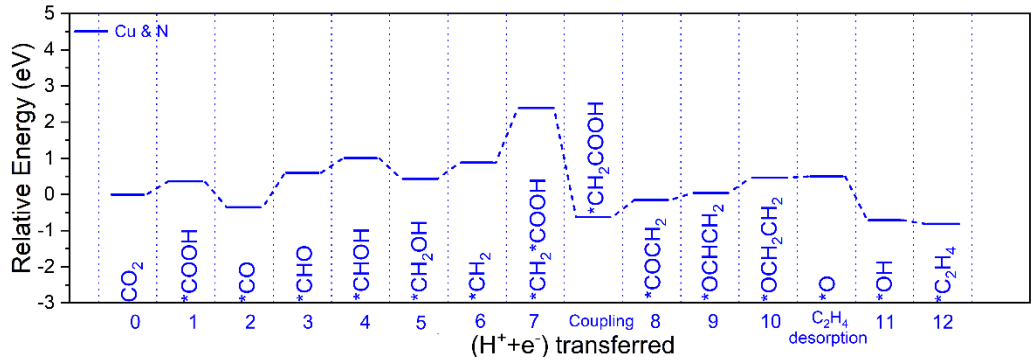


**Figure S15** Free energy diagram of $CO_2$ reduction to $C_2H_4$ for pathway 15 on Cu-$C_3N_4$.

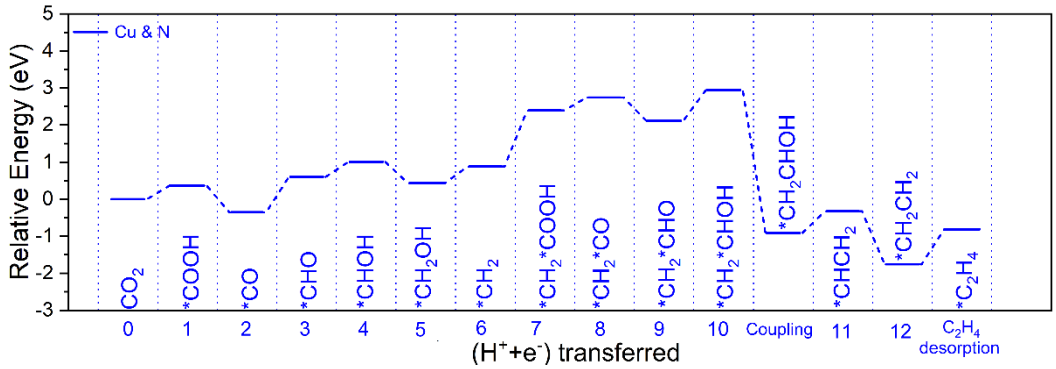


**Figure S16** Free energy diagram of $CO_2$ reduction to $C_2H_4$ for pathway 16 on Cu-$C_3N_4$.

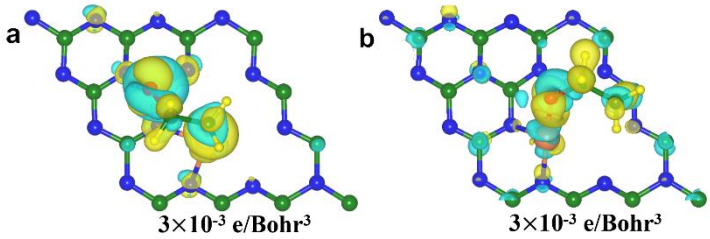


**Figure S17** The electron density difference for the intermediates (*$OCH_2CH_2$) adsorbed on the surface of Cu-$C_3N_4$ in the structure of (a) C*$OCH_2CH_2$*Cu (Pathway 3) and (b) Cu*$OCH_2CH_2$ (Pathway 10). Yellow represents electron accumulation, and cyan denotes electron depletion. Colour code: C green, N blue, H yellow, O red, Cu orange. Isosurface value for both (a) and (b) are $3\times10^{-3}$ e/Bohr$^3$.

**Table S1.** Computed gas phase properties in eV.

| Gas molecule | ZPE | $\int C_p dT$ | $-TS$ |
|---|---|---|---|
| CO(g) | 0.14 | 0.10 | -0.61 |
| $CO_2$(g) | 0.31 | 0.11 | -0.66 |
| HCHO(g) | 0.72 | 0.17 | -0.68 |
| $C_2H_4$(g) | 1.37 | 0.11 | -0.17 |
| $H_2$(g) | 0.27 | 0.10 | -0.20 |
| $H_2O$(g) | 0.58 | 0.10 | -0.25 |

**Table S2** Summary of the highest free energies change of the $C_2H_4$ pathways on the surface of Cu-$C_3N_4$ in vacuum..[a]

| **Active Sites** | | **Cu*** | | | | | | |
|---|---|---|---|---|---|---|---|---|
| *Intermediates* | | *CO* | *CHO* | *COOH* | *$OCH_2$* | *CHOH* | *CH* | *$CH_2$* |
| **N*** | *CHO* | **1.47** | **1.47** | **1.47** | **1.40** | **1.50** | — | — |
| | *COOH* | — | **1.55** | — | **1.40** | **1.50** | **1.98** | **1.51** |
| | *CHOH* | **1.59** | — | **1.45** | **—** | **1.50** | — | **1.51** |
| **C** | *$OCH_2$* | **0.96** | **0.96** | — | — | — | — | — |

a. The unit is eV.

**Table S3.** The detailed status of every step after ($H^+$+$e^-$) transfer for pathway 3.

| **($H^+$+$e^-$) transfer** | **status** |
|---|---|
| 0(Initial Stage) | *+2$CO_2$+12($H^+$+$e^-$) |
| 1 | Cu*COOH+$CO_2$+11($H^+$+$e^-$) |
| 2 | Cu*CO+$CO_2$+10($H^+$+$e^-$) +$H_2O$ |
| 3 | Cu*CHO+$CO_2$+9($H^+$+$e^-$) +$H_2O$ |
| 4 | C*$OCH_2$+$CO_2$+8($H^+$+$e^-$) +$H_2O$ |
| 5 | C*$OCH_2$*Cu*COOH+7($H^+$+$e^-$) +$H_2O$ |
| 6 | C*$OCH_2$+Cu*CO+6($H^+$+$e^-$) +2$H_2O$ |
| Coupling | C*$OCH_2$*Cu*CO+6($H^+$+$e^-$) +2$H_2O$ |
| 7 | C*$OCH_2$COH*Cu+5($H^+$+$e^-$) +2$H_2O$ |
| 8 | C*$OCH_2$CHOH*Cu+4($H^+$+$e^-$) +2$H_2O$ |
| 9 | C*$OCH_2$CH*Cu+3($H^+$+$e^-$) +3$H_2O$ |
| 10 | C*$OCH_2CH_2$*Cu+2($H^+$+$e^-$) +3$H_2O$ |
| $C_2H_4$ desorption | C*O+$C_2H_4$+2($H^+$+$e^-$) +3$H_2O$ |
| 11 | C*OH+$C_2H_4$+($H^+$+$e^-$) +3$H_2O$ |
| 12(Final Stage) | *+$C_2H_4$+4$H_2O$ |

**Table S4.** The detailed status of every step after ($H^+$+$e^-$) transfer for pathway 10.

| **($H^+$+$e^-$) transfer** | **status** |
|---|---|
| 0(Initial Stage) | *+2$CO_2$+12($H^+$+$e^-$) |
| 1 | Cu*COOH+$CO_2$+11($H^+$+$e^-$) |
| 2 | Cu*CO+$CO_2$+10($H^+$+$e^-$) +$H_2O$ |
| 3 | Cu*CHO+$CO_2$+9($H^+$+$e^-$) +$H_2O$ |
| 4 | Cu*$OCH_2$+$CO_2$+8($H^+$+$e^-$) +$H_2O$ |
| 5 | Cu*$OCH_2$+N*COOH+7($H^+$+$e^-$) +$H_2O$ |
| Coupling | Cu*$OCH_2COOH$+7($H^+$+$e^-$) +$H_2O$ |
| 6 | Cu*$OCH_2CO$*N+6($H^+$+$e^-$) +2$H_2O$ |
| 7 | Cu*$OCH_2CHO$+5($H^+$+$e^-$) +2$H_2O$ |
| 8 | Cu*$OCH_2CHOH$*N+4($H^+$+$e^-$) +2$H_2O$ |
| 9 | Cu*$OCH_2CH$*N+3($H^+$+$e^-$) +3$H_2O$ |
| 10 | Cu*$OCH_2CH_2$+2($H^+$+$e^-$) +3$H_2O$ |
| $C_2H_4$ desorption | Cu*O+$C_2H_4$+2($H^+$+$e^-$) +3$H_2O$ |
| 11 | Cu*OH+$C_2H_4$+($H^+$+$e^-$) +3$H_2O$ |
| 12(Final Stage) | *+$C_2H_4$+4$H_2O$ |

Reference

[1] A. Bard, R. Parsons, J. Jordan, Standard potentials in aqueous solution, CRC Press, 1985.

# Chapter 4: Theoretical Considerations on Activity of the Electrochemical $CO_2$ Reduction on Metal Single-Atom Catalysts with Asymmetrical Active Sites

## 4.1 Introduction and Significance

In this chapter, the catalytic activity and the synergetic effect of dual active sites for various single metal catalysts supported on graphitic carbon nitride (g-$C_3N_4$) for $CO_2$ reduction have been studied via Density Functional Theory (DFT) calculations. Through the application of the adsorption energies of CO* on the metal site and H* on the nitrogen site as bi-descriptors, seven out of 14 metal centers were screened out to have the propensity to generate high-value $C_2$ products. To further evaluate the catalyst activity on $C_2$ product formation, we established reaction pathways towards ethylene through M/N or M/C. The results show that Ru has the best performance (the limiting potential is - 0.90 V) by taking M/N as active sites. A dual volcano-shaped plot was built up based on the CO adsorption energies on metal sites, which can be used to indicate whether M/C or M/N shows better performance for a specific metal center. Our work shed light on developing criteria to guide the design of $CO_2$ reduction electrocatalysts with dual active sites. We achieved the research objectives 1.2.1 and 1.2.3 as we grouped the potential products for these 14 metal centers based on bi-descriptor, and the performance of obtaining $C_2$ products was further evaluated by establishing the dual volcano-shaped plot.

The highlights of this Chapter include:

- 14 different metal centers supported on graphitic carbon nitride (g-$C_3N_4$) as $CO_2$ reduction electrocatalysts are studied.
- A bi-descriptor picture is built to classify metal centers which can generate beyond CO product for $CO_2$ electroreduction.

- A dual volcano-shaped plot is formed to theoretically predict the $CO_2$ reduction performance under the synergistic effect of two active sites

## 4.2 Theoretical Considerations on Activity of the Electrochemical $CO_2$ Reduction on Metal Single-Atom Catalysts with Asymmetrical Active Sites

This Chapter is included as it has been accepted for publication by Catalysis Today on 11th June, 2021.

# Statement of Authorship

| | |
|---|---|
| Title of Paper | Theoretical Considerations on Activity of the Electrochemical $CO_2$ Reduction on Metal Single-Atom Catalysts with Asymmetrical Active Sites |
| Publication Status | ☐ Published ☑ Accepted for Publication<br>☐ Submitted for Publication ☐ Unpublished and Unsubmitted w ork w ritten in manuscript style |
| Publication Details | |

## Principal Author

| | | | |
|---|---|---|---|
| Name of Principal Author (Candidate) | Sijia Fu | | |
| Contribution to the Paper | Research plan, computation calculations, most of the characterizations and data analysis, and manuscript draft. | | |
| Overall percentage (%) | 90 | | |
| Certification: | This paper reports on original research I conducted during the period of my Higher Degree by Research candidature and is not subject to any obligations or contractual agreements with a third party that would constrain its inclusion in this thesis. I am the primary author of this paper. | | |
| Signature | | Date | 17/06/2021 |

## Co-Author Contributions

By signing the Statement of Authorship, each author certifies that:

i. the candidate's stated contribution to the publication is accurate (as detailed above);

ii. permission is granted for the candidate in include the publication in the thesis; and

iii. the sum of all co-author contributions is equal to 100% less the candidate's stated contribution.

| | | | |
|---|---|---|---|
| Name of Co-Author | Xin Liu | | |
| Contribution to the Paper | Assitance with research plan and data analysis. | | |
| Signature | | Date | 17/06/2021 |

| | | | |
|---|---|---|---|
| Name of Co-Author | Jingrun Ran | | |
| Contribution to the Paper | Supervision of the work, discussion of this manuscript and manuscript evaluation. | | |
| Signature | | Date | 17/06/2021 |

| | |
|---|---|
| Name of Co-Author | Yan Jiao |

| | | | |
|---|---|---|---|
| Contribution to the Paper | Supervision of the work, discussion of this manuscript and manuscript evaluation. | | |
| Signature | | Date | 17/06/2021 |

Please cut and paste additional co-author panels here as required.

# Theoretical Considerations on Activity of the Electrochemical $CO_2$ Reduction on Metal Single-Atom Catalysts with Asymmetrical Active Sites

Sijia Fu, Xin Liu, Jingrun Ran, Yan Jiao*

Center for Materials in Energy and Catalysis, School of Chemical Engineering and Advanced Materials, The University of Adelaide, South Australia 5005, Australia. yan.jiao@adelaide.edu.au

**ABSTRACT**

Electrochemical $CO_2$ reduction to higher-value hydrocarbons beyond $C_1$ products has attracted much attention recently. Single-atom catalysts (SACs) are regarded as promising $CO_2$ reduction electrocatalysts. However, most SACs only show activity to $C_1$ products. In this work, we considered the activity and the synergetic effect of dual active sites for metal SACs supported on graphitic carbon nitride (g-$C_3N_4$) as $CO_2$ reduction electrocatalysts. Density functional theory (DFT) calculations are employed. First, by using the adsorption energies of CO* on the metal site and that of H* on the nitrogen site as bi-descriptors, we predicted seven out of 14 metal centers have the propensity to generate beyond CO products. To further evaluate the catalyst activity on beyond CO product formation, we established reaction pathways towards ethylene through M/N or M/C. Ru has the best performance (the limiting potential is - 0.90 V) by taking M/N as active sites. A dual volcano-shaped plot is built up based on the CO adsorption energies on metal sites, which can be used to indicate whether M/C or M/N shows better performance for a specific metal center. Our work shed light on developing criteria to guide the design of $CO_2$ reduction electrocatalysts with dual active sites.

**Keywords**

$CO_2$ reduction reaction; Single atom catalyst; Asymmetrical active sites; $C_2$ production; Density functional theory

## 1. INTRODUCTION

The electrochemical $CO_2$ reduction reaction ($CO_2RR$) through renewable energy is a promising energy conversion process to help establish a carbon-neutral economy [1-3]. However, the $CO_2$ conversion is challenging due to the stability of the $CO_2$ molecule and therefore efficient catalysts are required [4, 5]. To date, most of the electrocatalytic $CO_2RR$ studies revolve around metal catalysts; among them, copper gains the most attention because of its ability to catalyse the generation of deeply reduced products, including various hydrocarbons and alcohols [6-10]. However, most of the catalysts can only obtain carbon monoxide (CO) or formic acid (HCOOH) through two-electron reductions, which are not as readily used as fuels as are higher-value, energy-dense hydrocarbons and alcohols [11, 12]. Although further reductions to hydrocarbons beyond CO or HCOOH, in particular $C_{2+}$ products, are desirable for realistic applications in energy storage, transportation, and chemical industry, it suffers from high overpotential and low selectivity caused by competitive hydrogen evolution reaction (HER) [13-15]. This is because HER is unavoidable in aqueous solution, which may occur either through the reduction protons ($2H^+ + 2e^- \rightarrow H_2$) or through the reduction of the solvent molecule itself ($2H_2O + 2e^- \rightarrow H_2+2OH^-$).

Single-atom catalysts (SACs) have attracted increasing interest in $CO_2RR$ in recent years due to the high utilization rate of metal atoms as active sites and favourable electronic structure [16-19]. However, for most SACs, they only show activity to $C_1$ products and the performance of generating higher carbon chain products is not satisfactory as they only contain one active site [20-22]. In recent years, a Cu-$C_3N_4$ SAC was found to generate detectable $C_2$ products, including $C_2H_4$, $C_2H_6$, and $C_2H_5OH$ [23]. This is because the molecular framework g-$C_3N_4$ provides a second active site (N/C) other than Cu, which enables the adsorption of two $CO_2$ molecules and benefits the following C-C coupling process [24]. These findings provide guidelines for the design of SACs electrocatalysts with synergetic effect of two active sites having the potential to generate $C_2$ products, such as loading other metals onto g-$C_3N_4$ ($M@C_3N_4$). However, there lacks a systematic study on underlying the mechanisms for generating beyond CO product and revealing the activity trends for various $M@C_3N_4$ [25]. Therefore, an

understanding of how the asymmetrical active sites work to generate beyond CO product can help guide the rational design of catalytic materials with dual active sites.

In this work, we employed density functional theory (DFT) calculations to reveal the mechanistic aspects of $CO_2$RR and trends in catalytic properties of dual sites of metal supported on g-$C_3N_4$. We used ethylene ($C_2H_4$) as a representative $C_2$ product to propose a systematic analysis of the factors which determine trends in catalytic properties of 14 types of M@$C_3N_4$. A bi-descriptor picture based on the adsorption energy of *CO and *H on the active sites is built to classify the product distribution for different metal centers. Seven out of 14 metal centers have the propensity to produce $C_2$ products. Through establishing the reaction pathways to obtain $C_2H_4$ on these seven metal centers through taking M/N or M/C as dual active sites, we found that Ru has the best performance with a limiting potential of – 0.90 V. Furthermore, we built up a dual volcano-shaped plot to theoretically predict the $CO_2$ reduction performance. The adsorption strength of *CO on metal site determines the better reaction mechanism (M/C or M/N) that the metal center takes. The activity trends displayed in the dual volcano-shaped plot may be served as a reference for the design of catalysts with dual active sites.

## 2. METHOD

DFT methods were used to carry out the electronic structure calculations through the Perdew-Burke-Ernzerhof (PBE) exchange-correlation functional in Vienna Ab Initio Simulation Package (VASP) [26-30]. The kinetic energy cutoff is set to be 500 eV for the plane-wave expansion after testing several cutoff energies. The convergence criterion for electronic structure iteration is $10^{-5}$ eV, and that for geometry optimization is 0.01 eV/Å. A 5 × 5 × 1 Γ-centerd Monkhorst-Pack k-point mesh was used for M@$C_3N_4$. The lattice parameter used for M@$C_3N_4$ were 7.089 × 7.089 × 20.000 Å, and the angle between the first two vectors is 120°. Considering the van der Waals interactions between atoms, the Tkatchenko-Scheffler method was applied for all calculations [31]. The computational hydrogen electrode method (CHE) was used for the calculation of the Gibbs free energy during the $CO_2$ reduction process[32]. The free energy of the electron-proton pair ($H^+ + e^-$) can be referenced to the chemical

potential of gaseous $H_2$ under standard conditions (0 V vs standard hydrogen electrode SHE, at 101,325 Pa). The Gibbs free energy calculation is using the formula expressed as follows,

$$G = E - TS + ZPE + \int C_p dT \quad (1)$$

in which E indicates the electronic energy obtained by DFT calculations. TS and ZPE indicate entropy and zero-point energy corrections, and T is the room temperature (T = 298.15K). ZPE and vibrational entropy of adsorbed species were obtained once vibrational frequencies were calculated. Entropies of gas molecules ($H_2$ and $CO_2$) were taken from standard values [33]. The free energy corrections for gas-phase properties of the critical reaction intermediates are summarized in Table S1 of the Supporting Information (SI).

Solvation calculations are performed for the reaction intermediates by using VASPsol, in which the solvation energies are modelled on periodic systems [34, 35].

The computational details of the calculation of the adsorption energy ($E_{ads}$) of the intermediates were calculated as follows:

$$E_{ads} = E_{adsorbate} + E_{support} - E_{adsorbate/support} \quad (2)$$

The limiting potential ($U_L$) at which each elementary step of a reaction becomes exergonic is simply measured from the potential dependence of the electrochemical rate, which is equivalent to the negative Gibbs free-energy change of the elementary reaction divided by the electronic charge. By choosing a simple hydrogenation reaction *A + $H^+$ + $e^-$ → *B as an example, $U_L$ is given by the following equation:

$$U_L = -\frac{\mu_B - \mu_A - \mu_{H^+ + e^-}\,[U=0\ V_{RHE}]}{e}$$

$$= \frac{-\Delta G_{elem}\,[U=0\ V_{RHE}]}{e} \quad (3)$$

where $e$ is the positive charge of an electron, and $\mu_{H^+ + e^-}$ is the chemical potential of $H^+$ + $e^-$ pair at zero potential, which can be obtained from the computational hydrogen electrode method [36, 37]. $\mu_A$ and $\mu_B$ are the chemical potentials of *A and *B respectively, which can be found from the calculated binding energies of these adsorbed species.

(a) (b)

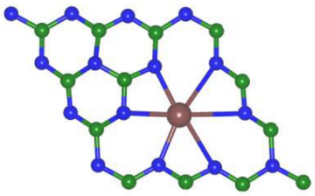

| | | | | | | | |
|---|---|---|---|---|---|---|---|
| 26 Fe Iron | 27 Co Cobalt | 28 Ni Nickel | 29 Cu Copper | 30 Zn Zinc | | | |
| 44 Ru Ruthenium | | 46 Pd Palladium | 47 Ag Silver | | 49 In Indium | 50 Sn Tin | |
| | | 78 Pt Platinum | 79 Au Gold | | | 82 Pb Lead | 83 Bi Bismuth |

Figure 1. (a) Atomic models for single metal atom catalyst supported on g-$C_3N_4$ matrix. (b) Metals that are considered for screening. Color code: C green, N blue, metal center brown.

Carbon nitride matrix (g-$C_3N_4$) has proven to be a suitable molecular scaffold, which can stabilize metal atoms under electrochemical conditions [23, 38]. In this study, we extent Cu-$C_3N_4$ to M-SACs supported on g-$C_3N_4$ (M@$C_3N_4$) to understand the reduction to beyond CO product on these surfaces. The atomic model is shown in Figure 1a. We screened 14 metal centers to thoroughly explore the effect of metal centers on the performance of forming $C_2$ products. In order to describe the structural stabilities of SACs on the $C_3N_4$ quantitatively, we calculated the binding energies of different metals with the g-$C_3N_4$ ligands. The computational details are included in Supplementary Note S1 and the binding energies are summarized in Figure S1. Figure 1b shows all the metal elements for screening included in this work. These metal elements are chosen because their activity for $CO_2$RR has been found in the past experiments [39, 40].

## 3. RESULTS AND DICUSSIONS

### 3.1 Beyond CO Product Selectivity by Bi-Descriptors

Although these metal centers M@$C_3N_4$ have similar structures with Cu-$C_3N_4$, they may not all have the ability to reduce $CO_2$ to $C_2$ products because of their different structures, physical and electronic properties. Under this circumstance, a simple descriptor that can help evaluate the promising catalyst materials that can generate beyond CO product is of great importance. Given that there are multiple intermediates in the reduction of $CO_2$ to $C_2$, the analysis of multi-dimensional space of adsorbate-surface interaction energies is complex. However, the CO binding energy can be used as a descriptor to

represent the adsorption energies of the carbon-bound species, which makes the analysis easier [41]. In addition, as hydrogen evolution reaction (HER) is regarded as the competition reaction of $CO_2$ reduction at all negative potentials, the H* binding energy is also an important descriptor [42]. Therefore, the CO* binding energy and H* binding energy have been used as bi-descriptors recently to explain the further reduction to products beyond CO [43, 44]. It has been pointed out that two properties are required for pure metals to produce beyond CO products. Firstly, $\Delta G_{H^*}$ should be greater than 0, which indicates the surface should not be poisoned by under-potential deposited H* [43]. Secondly, $\Delta G_{CO^*}$ should be smaller than 0, avoiding weak CO* binding which can release CO [43].

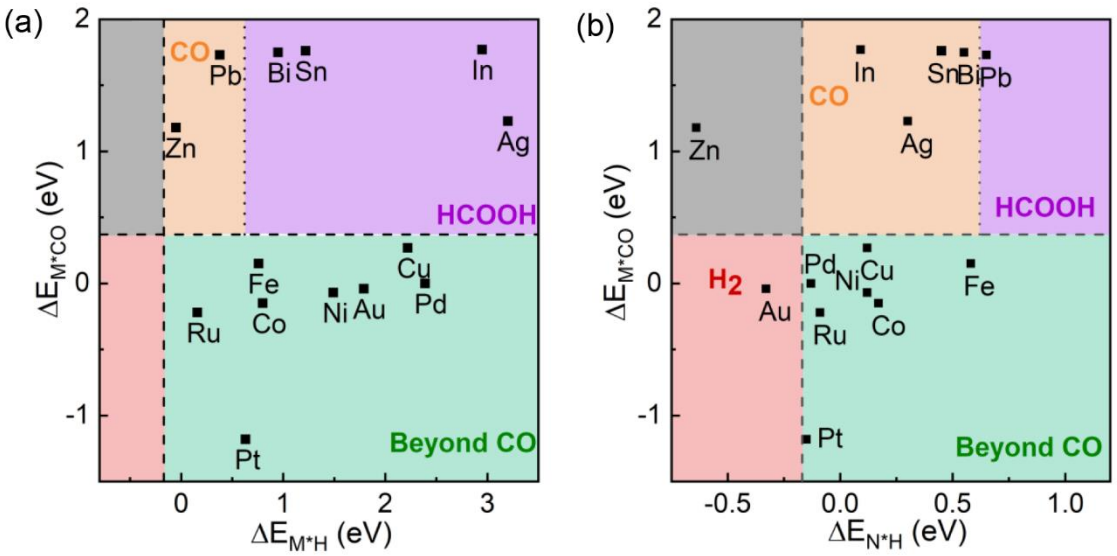


Figure 2. (a) Product grouping of the $M@C_3N_4$ catalysts according to the adsorption energy of CO and H on the metal active sites ($\Delta E_{M^*CO}$) and ($\Delta E_{M^*H}$). (b) Product grouping of the $M@C_3N_4$ catalysts according to the adsorption energy of CO on the metal active sites ($\Delta E_{M^*CO}$) and the adsorption energy of H on the nitrogen active sites ($\Delta E_{N^*H}$). The proposed products include $H_2$, CO, HCOOH (formic acid), and beyond CO. The black dash lines show the thermodynamic boundaries of absorbed hydrogen or non-adsorbed hydrogen ($\Delta G_{H^*}$ = 0 for $\frac{1}{2}H_2 \leftrightarrow H^*$) or CO ($\Delta G_{CO^*}$ = 0, for $CO \leftrightarrow CO^*$). Color code: beyond CO green, $H_2$ red, CO orange, HCOOH purple.

As M@$C_3N_4$ has more than one active site, different active sites need to be considered for the product grouping analysis. In this study, we considered H* binding on both metal site and nitrogen site. As shown in Figure 2a, when only consider metals as active sites, the CO* and H* binding energy at the metal site are used as bi-descriptors, Eight metal centers could possibly generate $C_2$ products including Ru, Pt, Fe, Co, Ni, Au, Cu, and Pd, owing to the strong CO* binding and weak H* binding. However, when nitrogen sites are also considered, the product distribution is predicted based on the CO* binding energy at the metal site and the H* binding energy at the nitrogen site. The results shown in Figure 2b indicate that Pt, Ru, Co, Ni, Pd, Fe, and Cu, are still located in the region which has the propensity to give products beyond CO owing to the strong CO* binding on metal site and the weak H* binding on nitrogen site. The binding energy of H-adatoms at the nitrogen site needs to be weak enough to avoid HER becoming the dominant reaction. In this case, Au is located in the region where H-adatom binding is strong, which leads to mainly $H_2$ gas formation. Therefore, after considering both situations, it can be found that when applying Pt, Ru, Co, Ni, Pd, Fe, and Cu as metal centers, M@$C_3N_4$ has the potential for beyond CO production. For metals located in the region where the CO* binding is weak, the main product from $CO_2$ reduction is CO because of a preferential CO desorption. These metals include In, Ag, Sn, Bi, and Pb. If the CO binding is even weaker, the main product for the reduction is HCOOH. This is because the CO* binding is too weak, and the reduction stops before the formation of CO. For Zn-$C_3N_4$, as the H* binding on the nitrogen site is strong and the CO* binding on the Zn site is weak, both $H_2$ and CO are the main products. The bi-descriptor summarizes well the computation results and can serve as an indicator for finding a good $CO_2$RR catalyst with more than one active site which can produce beyond CO products. However, the rough product grouping isn't able to find a catalyst that can reduce $CO_2$ to $C_2$ products at low overpotential. Therefore, the analysis of the potential performance of the electrocatalysts included in the beyond CO region is of great importance in order to obtain a full picture of the $CO_2$RR activity for dual sites.

### 3.2 Limiting Potentials and Mechanisms of $CO_2$RR to Ethylene

After the initial screening of the M@$C_3N_4$ catalysts, we focus on the performance of the metal centers which show the potentials of producing beyond CO product to explore the underlying $CO_2$RR activity

picture. Firstly, we selected $C_2H_4$ as the representative $C_2$ product to obtain the related potential performance for these metal centers. This is because $C_2H_4$ is the most common $C_2$ product for $CO_2$ reduction and it is an important chemical raw material. In our previous work, the reaction mechanisms of $C_2H_4$ formation on Cu-$C_3N_4$ based on Cu/C/N were studied thoroughly, we extended the reaction mechanisms to other M-$C_3N_4$. M*$OCH_2$ and N*COOH are considered as the key intermediates for C-C coupling among M/N mechanisms, and M*CO and C*$OCH_2$ are considered as the key intermediates for C-C coupling among M/C mechanisms. For each metal center, the reaction based on both M/N and M/C mechanisms are performed and compared. Then, as the intrinsic activity of electrocatalysts can be evaluated through analysing the limiting potential ($U_L$), which is defined as the lowest negative potential at which the pathway becomes exergonic [38], the limiting potentials for these M@$C_3N_4$ structures are summarized in Figure 3a. According to this figure, for most of the metal centers, $CO_2$RR is based on the synergetic work of metal and nitrogen, and among them, Ru-$C_3N_4$ has the best performance (- 0.90 V). In addition, only for Fe and Cu, $CO_2$RR is based on the synergetic work of metal and carbon, and Cu has a better $CO_2$RR activity than Fe. Moreover, as shown in Figure 3a, the PDS step varies along with the change of the active sites and the change of the limiting potential for different elements. When $CO_2$RR is based on the synergetic work of metal and carbon (for Fe and Cu), the potential-determining step (PDS) is the same step, which is M*CHO + $(H^+ + e^-)$ → C*$OCH_2$. However, when using metal and nitrogen as active sites (for the rest elements), there are multiple PDSs: the steps for Ni, Pd, and Pt are the same, which is the protonation of the second $CO_2$ on nitrogen site; the step for Co is one dehydrogenation step after C-C coupling; the step for Ru is the formation of Ru*$OCH_2$ from Ru*CHO, instead of the protonation of the second $CO_2$. It is noticeable that the limiting potential is related to the active sites take part in $CO_2$RR and their different reaction mechanisms.

To further reveal the reaction mechanisms between dual active sites, we then plotted the free energy diagrams for $CO_2$RR to $C_2H_4$ on Ru-$C_3N_4$ and Cu-$C_3N_4$ in Figure 3b and c. The two metal centers show the best performance toward M/N and M/C mechanism, and are used to explain the difference between the two reaction mechanisms. The values for free energy change for every step and the related detailed status after every proton and electron pair transfer for Ru and Cu are concluded in Table S2 and S3.

The free energy diagrams for other elements can be found in Figure S2-S6. In addition, the free energy diagram for Ru-$C_3N_4$ applying M/C as active sites is displayed in Figure S7, and that for Cu-$C_3N_4$ applying M/N as active sites is displayed in Figure S8. The main difference that appears for M/N and M/C is the step of the protonation of the second $CO_2$. For the M/N combination, after the first $CO_2$ is reduced on the metal site, the second $CO_2$ is reduced on the nitrogen site. However, for M/C combination, after the first $CO_2$ is reduced on the metal site, the intermediate is transferred to the carbon site and leave the metal site free to reduce the second $CO_2$. Since metal sites have better $CO_2$ reduction activity than the nitrogen site, the protonation of the second $CO_2$ in M/N combination usually is not as easy as in M/C combination. This explains why the protonation of the second $CO_2$ is usually the PDS when using M/N as active sites.

The performance of Ru-$C_3N_4$ is quite outstanding and its PDS is different from other metal centers. Therefore, further analysis based on free energy is carried out to explain the outstanding performance. We compared the free energy difference between the formation of Ru*$OCH_2$ and the protonation of the second $CO_2$ on the N site. It is found from Table S2 that the formation of Ru*$OCH_2$ (0.90 eV) is only 0.02 eV higher than the protonation of the second $CO_2$ (0.88eV). Therefore, the protonation of the second $CO_2$ is still a challenging step for Ru. However, the free energy for Ru*$OCH_2$ + N*COOH is the lowest among all other M*$OCH_2$ + N*COOH structures, indicating that the intermediates are stabilized well by Ru-$C_3N_4$. Hence, the free energy change for the protonation of $CO_2$ on the N site in Ru-$C_3N_4$ is not as high as that for other metals. However, the evaluation of the limiting potentials alone is not enough to explain why some metal centers have better performance when using M/C as active sites in $CO_2$ reduction to $C_2H_4$ while the others prefer using M/N as active sites. Therefore, it is desirable to study the activity trend to underlying reasons for choosing the active sites which will help the rational design of catalysts.

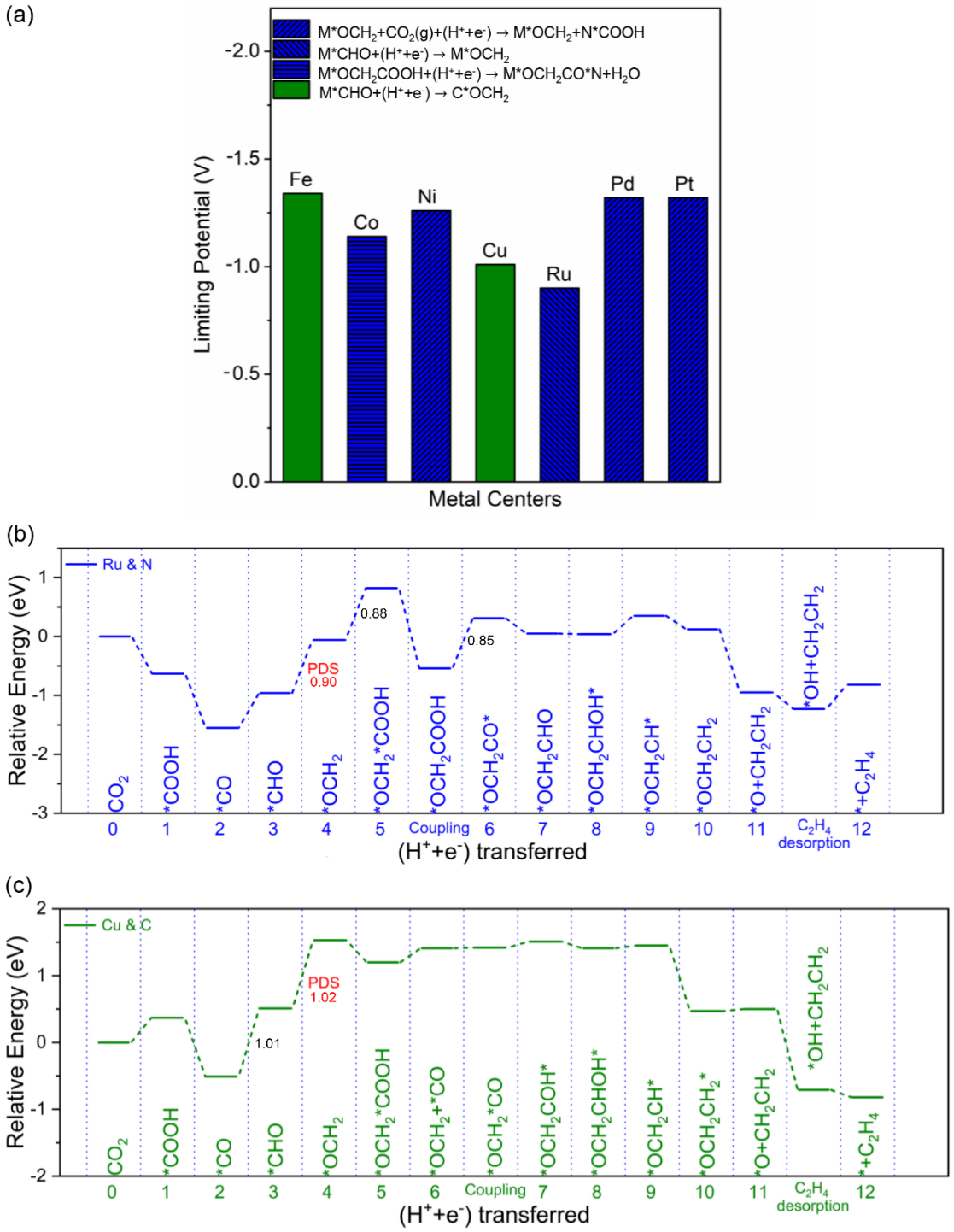


Figure 3. (a) Summary of limiting potentials of metal single-atom catalysts on g-$C_3N_4$ for $CO_2$RR. Green and blue indicates the reaction pathway takes M&C or M&N as active sites. Free energy diagrams of (b) Ru-$C_3N_4$ and (c) Cu-$C_3N_4$, respectively. The reference potential is set to 0V vs SHE. The PDS steps are listed in red with the correlated free energy change values (in eV).

### 3.3 Dual Volcano-shaped Plot for the Design of SACs as $CO_2$RR Electrocatalysts

Given that there are multiple intermediates in the reduction of $CO_2$ to $C_2H_4$, along with the different active sites the intermediates bind, the analysis of the activity trend will be extremely complex if considering all reaction steps. Therefore, to simplify the problem, it is necessary to reduce the number of parameters and only focus on the critical steps. Based on the different reaction mechanisms, we separated the analysis into three parts. The first part includes the steps shared by M/C and M/N, the second and third parts include the critical steps for M/C and M/N reaction mechanisms, respectively. Firstly, we focus on the elementary reaction steps on metal sites, including M*COOH, M*CO, and M*CHO. For both M/C and M/N reaction mechanisms, the protonation of the first $CO_2$ appears on the metal site and the following two reduction intermediates also bind with the catalyst surface through the metal active site. Moreover, these steps are necessary before the introduction of the other active site (either C or N). The calculated adsorption energies of M*COOH and M*CHO are summarized in Figure 4a and plotted against the binding energy of CO. As these intermediates all interact with the surface through a carbon atom, the binding energy of *COOH and *CHO are linearly correlated with that of *CO [45]. The structures and properties for these key intermediates and those mentioned in the following parts on different metal surfaces are summarized in Table S4 and S5.

After that, we focus on the critical step that happens on the carbon site for M/C reaction mechanism, which is the formation of $C^*OCH_2$ ($M^*CHO + H^+ + e^- \rightarrow C^*OCH_2$). As shown in Figure 3a, the formation of $C^*OCH_2$ is the PDS for both Fe and Cu, which are the only two metals applying M/C reaction mechanism. Moreover, the active site transfers from metal to carbon during this step, which leaves the metal site free for the protonation of the second $CO_2$. Therefore, the formation of $C^*OCH_2$ is regarded as the most important step for M/C reaction mechanism. The calculated adsorption energies of $C^*OCH_2$ are summarized in Figure 4b and plotted against the binding energy of CO.

Finally, for M/N reaction mechanism, we focus on the formation of $M^*OCH_2$ ($M^*CHO + H^+ + e^- \rightarrow M^*OCH_2$) and N*COOH ($M\text{-}C_3N_4 + CO_2 + H^+ + e^- \rightarrow N^*COOH$). The formation of $M^*OCH_2$ is considered because it is a necessary step involved in the M/N reaction mechanism before the participation of the second active site, nitrogen. The formation of N*COOH is considered because the

second $CO_2$ protonation on nitrogen site, written as $M^*OCH_2 + CO_2 + (H^+ + e^-) \rightarrow M^*OCH_2 + N^*COOH$, is usually the PDS for M/N. Through the charge density analysis shown in Figure S9, it has been found that there is no electron transfers between $M^*OCH_2$ and N*COOH. Therefore, in this case, we ignored the intermediate combined with the metal site, which is $^*OCH_2$. We only studied the performance of $CO_2$ protonation on the N site so that the results can be compared with that on the metal site. The calculated adsorption energies of $M^*OCH_2$ and N* COOH are summarized in Figure 4c and plotted against the binding energy of CO.

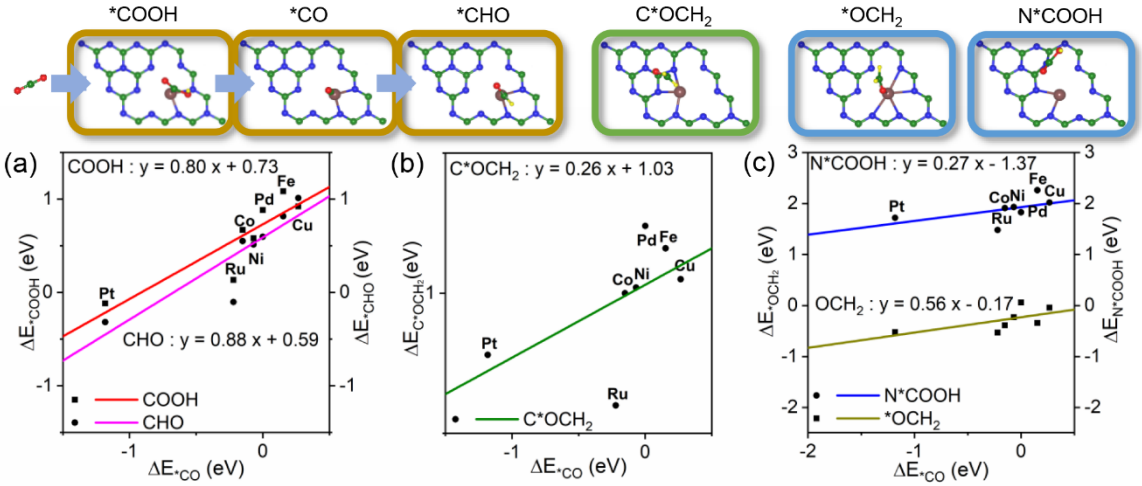


Figure 4. Adsorption energy scaling for the key bound intermediates. (a) The adsorption energies of *COOH and *CO, (b) $C^*OCH_2$, (c) $^*OCH_2$ and N*COOH are plotted against the binding energy of *CO. More tightly bound adsorbates correspond to more negative binding energies. The structures of the intermediates are listed on top. Color code: C green, N blue, O red, H yellow, metal center brown.

The scaling relation performance on carbon and nitrogen active site which is displayed in Figures 4b and 4c is not satisfied. This may be caused by the different active sites and binding stom in the key intermediates. However, the results may help obtain general activity trends for $M@C_3N_4$. Therefore, based on the scale affinity relations found above, the binding energies can be converted to chemical potentials by the free energy corrections calculated with standard statistical mechanics methods [36].

Hence, the limiting potentials for for each of the elementary steps can be estimated as a function of the affinity for CO on metal site [36].

Estimation of the free energy change for the elementary steps mentioned above based on the linear relationships observed is displayed in Figure 5: (a) for M and C as active sites and (b) for M and N as active sites. At a given value of $\Delta E_{*CO}$, the related elementary step of the lowest line indicates the potential-determining step (PDS). For example, as can be seen in Figure 5a, the two bottom-most $U_L$ lines, M*CHO → C*OCH$_2$ and $CO_2$ → M*COOH, are the most negative of the reaction steps for M/C. For the M/N system shown in Figure 5b, a broken line is formed by three bottom-most $U_L$ lines, M*CHO → M*OCH$_2$, M*CO → M*CHO, and $CO_2$ → N*COOH. As shown in Figures 5a and 5b, the limiting potentials for CO production (red and purple lines) are lower comparing to beyond CO formation. The step of introducing the second active site other than metal becomes the bottom-most $U_L$ line during certain $\Delta E_{*CO}$ value, which means it generally increases the value of the limiting potential for both M/C and M/N when producing beyond CO product. Hence, the selectivity for beyond CO product is lower comparing with the production of CO. Figure 5a and 5b also explains that different metal centers impact the limiting potential. $\Delta E_{*CO}$ and the adsorption strength of all intermediates vary when the metal changes according to the scaling relations. The study of the activity trends underlies the reaction mechanisms and rules, which is beneficial for the ration design of other dual active site catalysts.

Since the reaction pathways to $C_2H_4$ for one element can either take M/N or M/C as active sites, the pathway tends to be the one with a more positive value of limiting potential, which brings Figures 5a and 5b together to Figure 5c and generates a dual volcano-shaped plot. This plot indicates that $\Delta E_{*CO}$ determines the active sites taken for one element. The reaction pathway takes M/C as active sites when the $\Delta E_{*CO}$ belongs to the right volcano, and it takes M/N as active sites when the $\Delta E_{*CO}$ belongs to the left volcano. As shown in Figure 5c, the dark yellow, pink, and blue lines form the left volcano shape for M/N, corresponding to the PDS steps found in Figure 5b; the green and purple lines form the right volcano shape for M/C, corresponding to the PDS steps found in Figure 5a. The lowest lines of the cross part are presented in dot as the reaction pathway tends to take the upper lines due to the more positive limiting potential. The importance of introducing another active site is highlighted in Figure 5c

because it improves the performance of metal centers and the related $U_L$ value becomes more positive as it changes from dotted line to solid line. In addition, most of the metal centers are close to where the two volcanos intersect. The top of the right volcano is located higher than the left top, which indicates the smallest overpotential can be explored at the right volcano top. Cu is seen to sit near the right top of this 'volcano'-type relation ($U_L$ value is -1.02 V), indicating its good activity in $CO_2$RR. Among the elements involved in the left volcano, the $U_L$ value for Ru-$C_3N_4$ is outstanding (-0.90 V), which is even better than Cu-$C_3N_4$. As discussed in the previous part, this is because Ru-$C_3N_4$ can stabilize *COOH better comparing with other metal centers.

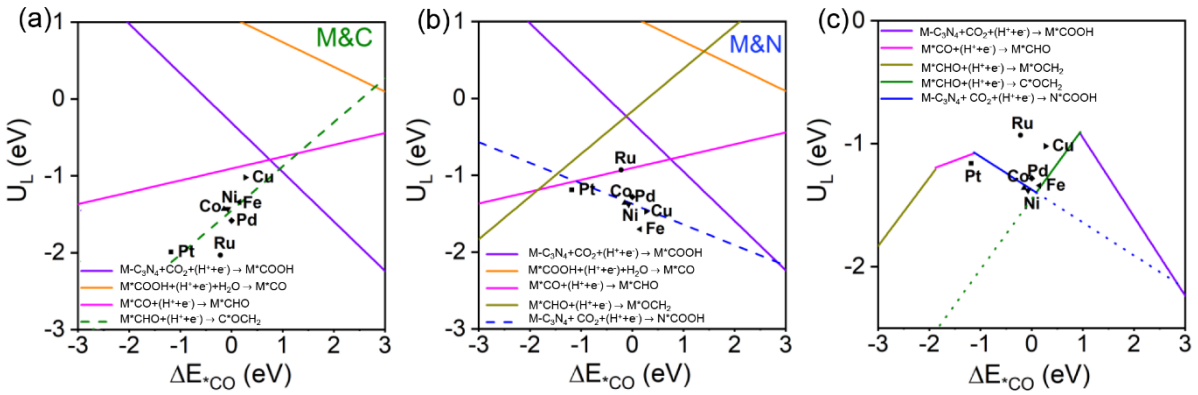


Figure 5. Limiting potentials ($U_L$) defined as the negative of the free energy change for every elementary proton-electron transfer step listed in figure (a) for M and C, (b) for M and N, (c) for M/C/N. Every line is a function of the electrocatalyst adsorption energy of CO ($\Delta E_{*CO}$) at 0 V vs SHE. For each elementary reaction, the addition of a proton-electron pair ($H^+ + e^-$) to the reactant is involved. The $\Delta E_{*CO}$ values for each metal supported on carbon nitride are shown on the plot, along with their overall predicted value of $U_L$ based on the scaling relations. The metal labels in (a) and (b) correspond to the dashed line, and that in (c) correspond to the solid lines only.

## 4. CONCLUSION

In summary, adopting DFT simulations, we took metal SACs supported on carbon nitride matrix as model systems and thoroughly screened 14 metal centers to reveal the mechanistic aspects of chemistry

in the $CO_2$RR process. A bi-descriptor picture is built for the product distribution of the $CO_2$ electroreduction. Through applying the CO binding energy and the H binding energy as descriptors, seven metal centers (including Pt, Ru, Co, Ni, Pd, Fe, and Cu) have been pointed out to have the propensity to generate beyond CO product. Our study also concludes the catalyst activity on beyond CO product formation by taking $C_2H_4$ as an example. We established the reaction pathways to obtain $C_2H_4$ on these seven metal centers through taking M/N or M/C as active sites. Ru-$C_3N_4$ has the best performance among all these metal centers. A dual volcano-shaped plot is built to theoretically predict the $CO_2$ reduction performance under the synergistic effect of two active sites. It has been found that the binding energy of CO on metal site determines whether M/C or M/N has a better performance for one element during $CO_2$ reduction. The activity trends obtained from the calculations shed light on developing criteria to guide the design of $CO_2$ reduction electrocatalysts with dual active sites.

**CRediT Authorship Contribution Statement**

**Sijia Fu**: Performed DFT computations, Investigation, Formal analysis, Writing- original draft preparation. **Xin Liu**: Formal analysis, Validation. **Jingrun Ran**: Supervision, Writing- reviewing and editing. **Yan Jiao**: Conceptualization, Resources, Supervision, Writing- reviewing and editing.

**Acknowledgements**

This work was supported by the Australian Research Council through these programs (FT190100636 and DP190103472). DFT computations for this research were undertaken with the assistance of supercomputing resources provided by the Phoenix HPC service at the University of Adelaide and the resources and services from the National Computational Infrastructure (NCI) supported by the Australian Government.

**References**

[1] X. Lim, Nature News, 526 (2015) 628.

[2] C. Liu, B.C. Colón, M. Ziesack, P.A. Silver, D.G. Nocera, Science, 352 (2016) 1210-1213.

[3] K.K. Sakimoto, A.B. Wong, P. Yang, Science, 351 (2016) 74-77.

[4] A. Vasileff, Y. Zheng, S.Z. Qiao, Advanced Energy Materials, 7 (2017) 1700759.

[5] X. Mao, T.A. Hatton, Industrial & Engineering Chemistry Research, 54 (2015) 4033-4042.

[6] K.P. Kuhl, E.R. Cave, D.N. Abram, T.F. Jaramillo, Energy & Environmental Science, 5 (2012) 7050-7059.

[7] C.S. Chen, A.D. Handoko, J.H. Wan, L. Ma, D. Ren, B.S. Yeo, Catalysis Science & Technology, 5 (2015) 161-168.

[8] D. Ren, Y. Deng, A.D. Handoko, C.S. Chen, S. Malkhandi, B.S. Yeo, Acs Catalysis, 5 (2015) 2814-2821.

[9] Y.i. Hori, Electrochemical $CO_2$ reduction on metal electrodes, Modern aspects of electrochemistry, Springer2008, pp. 89-189.

[10] L. Zhang, Z.J. Zhao, J. Gong, Angewandte Chemie International Edition, 56 (2017) 11326-11353.

[11] S. Liu, H. Yang, X. Huang, L. Liu, W. Cai, J. Gao, X. Li, T. Zhang, Y. Huang, B. Liu, Advanced Functional Materials, 28 (2018) 1800499.

[12] J.-P. Jones, G.K.S. Prakash, G.A. Olah, Israel Journal of Chemistry, 54 (2014) 1451-1466.

[13] M. Jouny, W. Luc, F. Jiao, Nature Catalysis, 1 (2018) 748-755.

[14] A. Loiudice, P. Lobaccaro, E.A. Kamali, T. Thao, B.H. Huang, J.W. Ager, R. Buonsanti, Angewandte Chemie International Edition, 55 (2016) 5789-5792.

[15] Q. Fan, M. Zhang, M. Jia, S. Liu, J. Qiu, Z. Sun, Materials today energy, 10 (2018) 280-301.

[16] S. Nellaiappan, N.K. Katiyar, R. Kumar, A. Parui, K.D. Malviya, K. Pradeep, A.K. Singh, S. Sharma, C.S. Tiwary, K. Biswas, ACS Catalysis, 10 (2020) 3658-3663.

[17] H. Lv, L. Lin, X. Zhang, Y. Song, H. Matsumoto, C. Zeng, N. Ta, W. Liu, D. Gao, G. Wang, Advanced Materials, 32 (2020) 1906193.

[18] M. Li, H. Wang, W. Luo, P.C. Sherrell, J. Chen, J. Yang, Advanced Materials, 32 (2020) 2001848.

[19] T. Wang, Q. Zhao, Y. Fu, C. Lei, B. Yang, Z. Li, L. Lei, G. Wu, Y. Hou, Small Methods, 3 (2019) 1900210.

[20] H. Zhong, F. Meng, Q. Zhang, K. Liu, X. Zhang, Nano Research, 12 (2019) 2318-2323.

[21] H.B. Yang, S.-F. Hung, S. Liu, K. Yuan, S. Miao, L. Zhang, X. Huang, H.-Y. Wang, W. Cai, R. Chen, Nature Energy, 3 (2018) 140-147.

[22] H. Shang, T. Wang, J. Pei, Z. Jiang, D. Zhou, Y. Wang, H. Li, J. Dong, Z. Zhuang, W. Chen, Angewandte Chemie International Edition, (2020).

[23] Y. Jiao, Y. Zheng, P. Chen, M. Jaroniec, S.Z. Qiao, Journal of the American Chemical Society, 139 (2017) 18093-18100.

[24] S. Fu, X. Liu, J. Ran, Y. Jiao, S.-Z. Qiao, Applied Surface Science, 540 (2021) 148293.

[25] X. Liu, Y. Jiao, Y. Zheng, M. Jaroniec, S.-Z. Qiao, Journal of the American Chemical Society, 141 (2019) 9664-9672.

[26] G. Kresse, J. Hafner, Physical Review B, 47 (1993) 558-561.

[27] G. Kresse, J. Furthmüller, Physical Review B, 54 (1996) 11169-11186.

[28] G. Kresse, D. Joubert, Physical Review B, 59 (1999) 1758-1775.

[29] J.P. Perdew, K. Burke, M. Ernzerhof, Physical Review Letters, 77 (1996) 3865-3868.

[30] J.P. Perdew, K. Burke, M. Ernzerhof, Physical Review Letters, 78 (1997) 1396-1396.

[31] A. Tkatchenko, M. Scheffler, Physical Review Letters, 102 (2009) 073005.

[32] J.K. Nørskov, T. Bligaard, A. Logadottir, J. Kitchin, J.G. Chen, S. Pandelov, U. Stimming, Journal of The Electrochemical Society, 152 (2005) J23.

[33] W.M. Haynes, CRC handbook of chemistry and physics, CRC press2014.

[34] K. Mathew, R. Sundararaman, K. Letchworth-Weaver, T. Arias, R.G. Hennig, The Journal of chemical physics, 140 (2014) 084106.

[35] K. Mathew, V.C. Kolluru, S. Mula, S.N. Steinmann, R.G. Hennig, The Journal of Chemical Physics, 151 (2019) 234101.

[36] A.A. Peterson, F. Abild-Pedersen, F. Studt, J. Rossmeisl, J.K. Norskov, Energy & Environmental Science, 3 (2010) 1311-1315.

[37] J.K. Nørskov, J. Rossmeisl, A. Logadottir, L. Lindqvist, J.R. Kitchin, T. Bligaard, H. Jonsson, The Journal of Physical Chemistry B, 108 (2004) 17886-17892.

[38] Y. Zheng, Y. Jiao, Y. Zhu, Q. Cai, A. Vasileff, L.H. Li, Y. Han, Y. Chen, S.-Z. Qiao, Journal of the American Chemical Society, 139 (2017) 3336-3339.

[39] Q. Zhang, J. Guan, Advanced Functional Materials, 30 (2020) 2000768.

[40] N. Han, P. Ding, L. He, Y. Li, Y. Li, Advanced Energy Materials, 10 (2020) 1902338.

[41] A.A. Peterson, J.K. Nørskov, The Journal of Physical Chemistry Letters, 3 (2012) 251-258.

[42] X. Liu, Y. Jiao, Y. Zheng, K. Davey, S.-Z. Qiao, Journal of Materials Chemistry A, 7 (2019) 3648-3654.

[43] A. Bagger, W. Ju, A.S. Varela, P. Strasser, J. Rossmeisl, Catalysis Today, 288 (2017) 74-78.

[44] A. Bagger, W. Ju, A.S. Varela, P. Strasser, J. Rossmeisl, ChemPhysChem, 18 (2017) 3266-3273.

[45] F. Abild-Pedersen, J. Greeley, F. Studt, J. Rossmeisl, T. Munter, P.G. Moses, E. Skulason, T. Bligaard, J.K. Nørskov, Physical review letters, 99 (2007) 016105.

# Supporting Information

# Theoretical Considerations on Activity of the Electrochemical $CO_2$ Reduction on Metal Single-Atom Catalysts with Asymmetrical Active Sites

Sijia Fu, Xin Liu, Jingrun Ran, Yan Jiao*

Center for Materials in Energy and Catalysis, School of Chemical Engineering and Advanced Materials, The University of Adelaide, South Australia 5005, Australia. yan.jiao@adelaide.edu.au

**This PDF file includes:**

Reaction free energy diagrams

Charge density diagram

Computed gas phase properties

Detailed free energy changes of every step after ($H^+ + e^-$) transfer for Ru-$C_3N_4$ and Cu-$C_3N_4$

Structures for key intermediates

**Note S1**

**Figure S1 to S9**

**Table S1 to S5**

**Note S1 Metal Bind energy calculation**

The binding energy ($E_b$) of a series of metals (Fe, Co, Ni, Cu, Zn, Ru, Pd, Ag, In, Sn, Pt, Au, Pb, Bi) with that of g-$C_3N_4$ ligand was evaluated as:

$$E_b = E_{M-C3N4} - E_{g-C3N4} - E_M$$

where $E_{M\text{-}C3N4}$ is the total energy of the metal embedded in g-$C_3N_4$, $E_{g\text{-}C3N4}$ is the energy for the g-$C_3N_4$ and $E_M$ is the energy for the isolated metal atom.

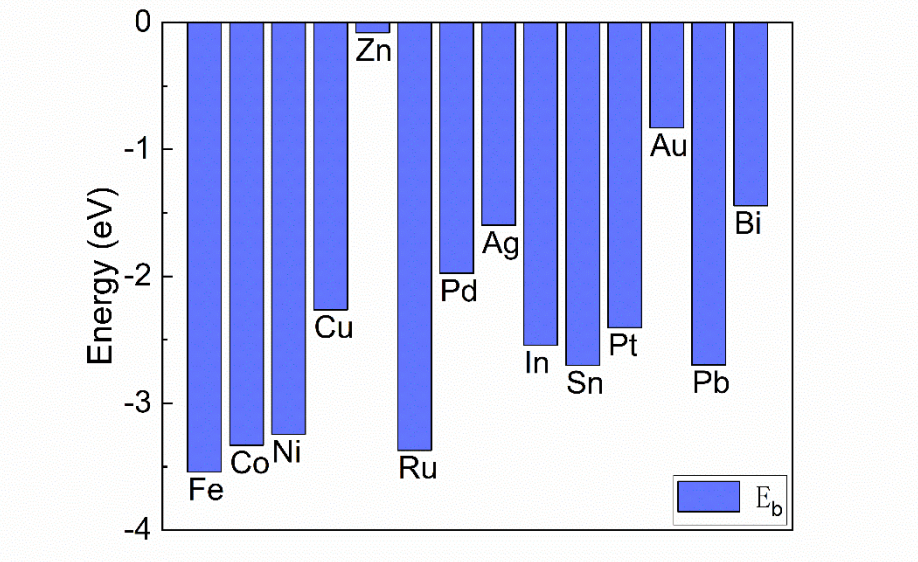


**Figure S1** The binding energy of M embedded into g-$C_3N_4$ ligands.

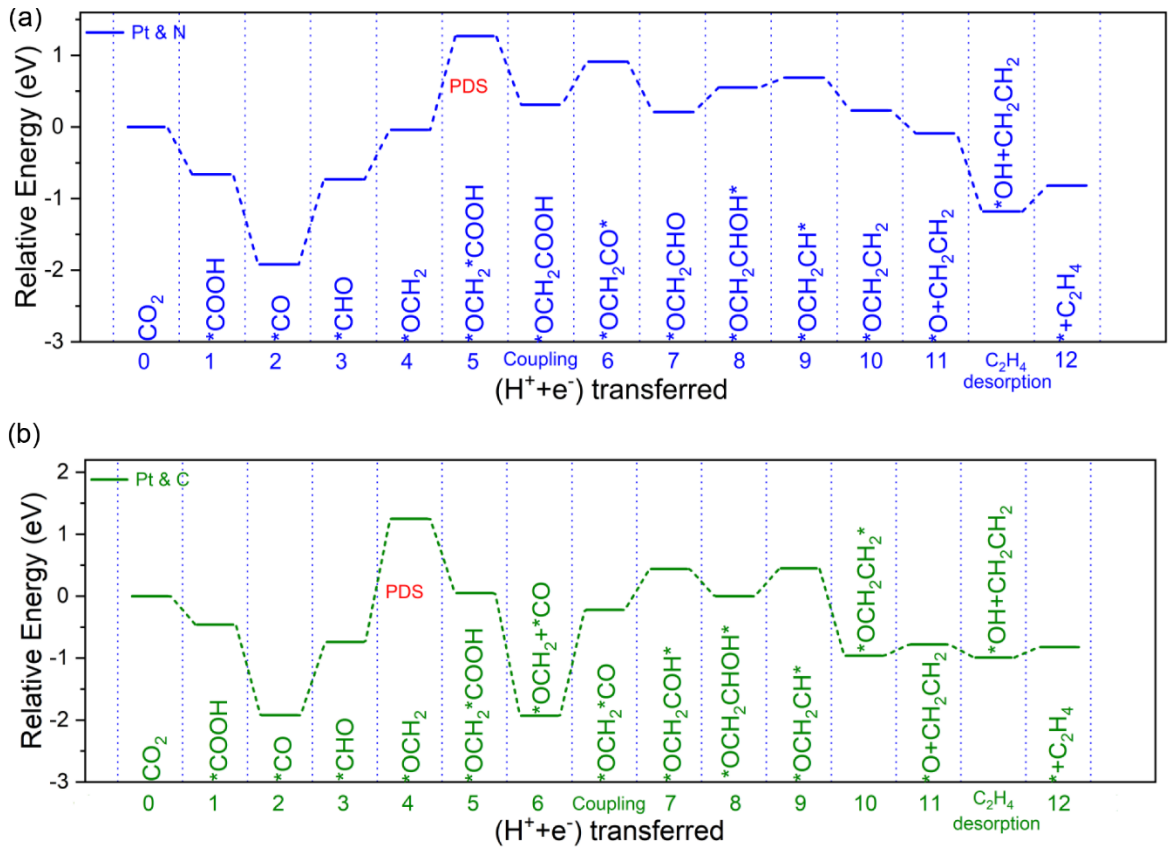


**Figure S2** Free energy diagram of $CO_2$ reduction to $C_2H_4$ on Pt-$C_3N_4$, using (a) Pt &N and (b) Pt & C as active sites.

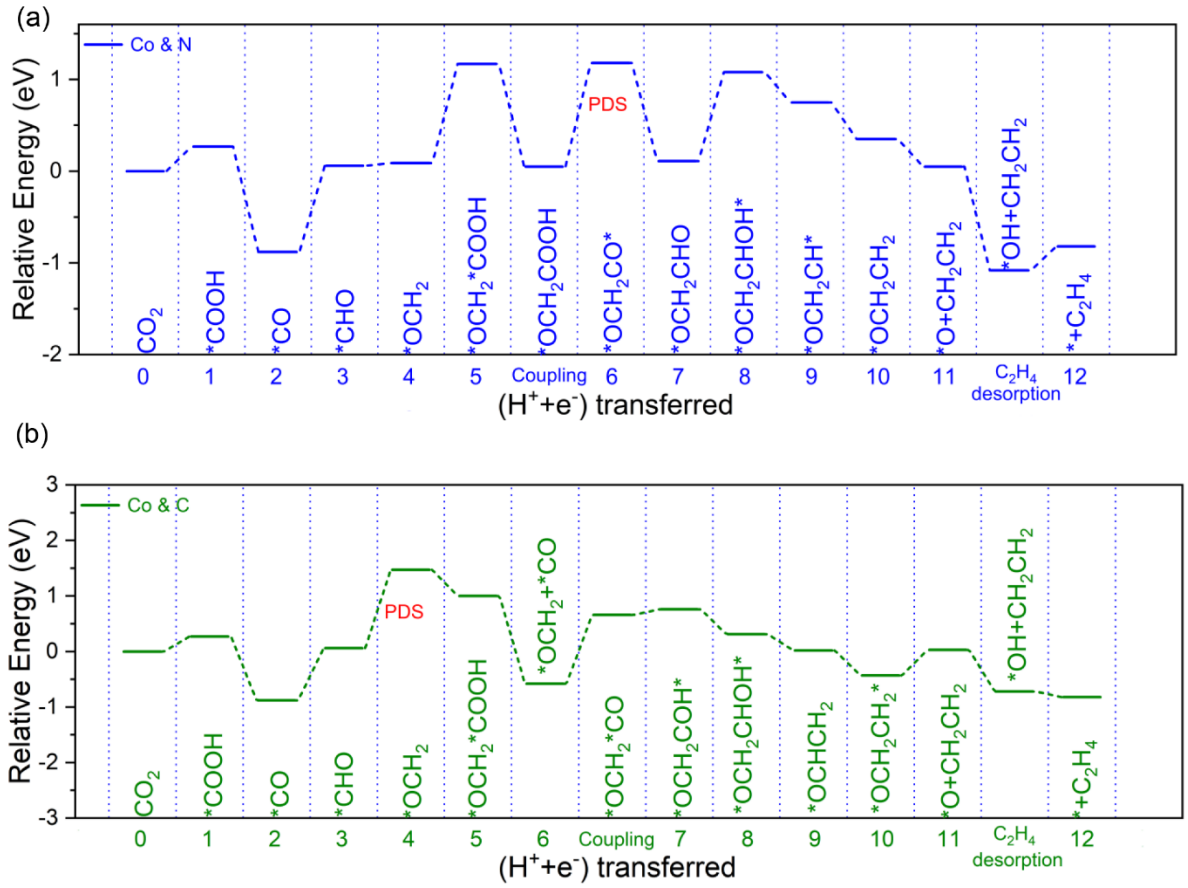


**Figure S3** Free energy diagram of $CO_2$ reduction to $C_2H_4$ on Co-$C_3N_4$, using (a) Co &N and (b) Co & C as active sites.

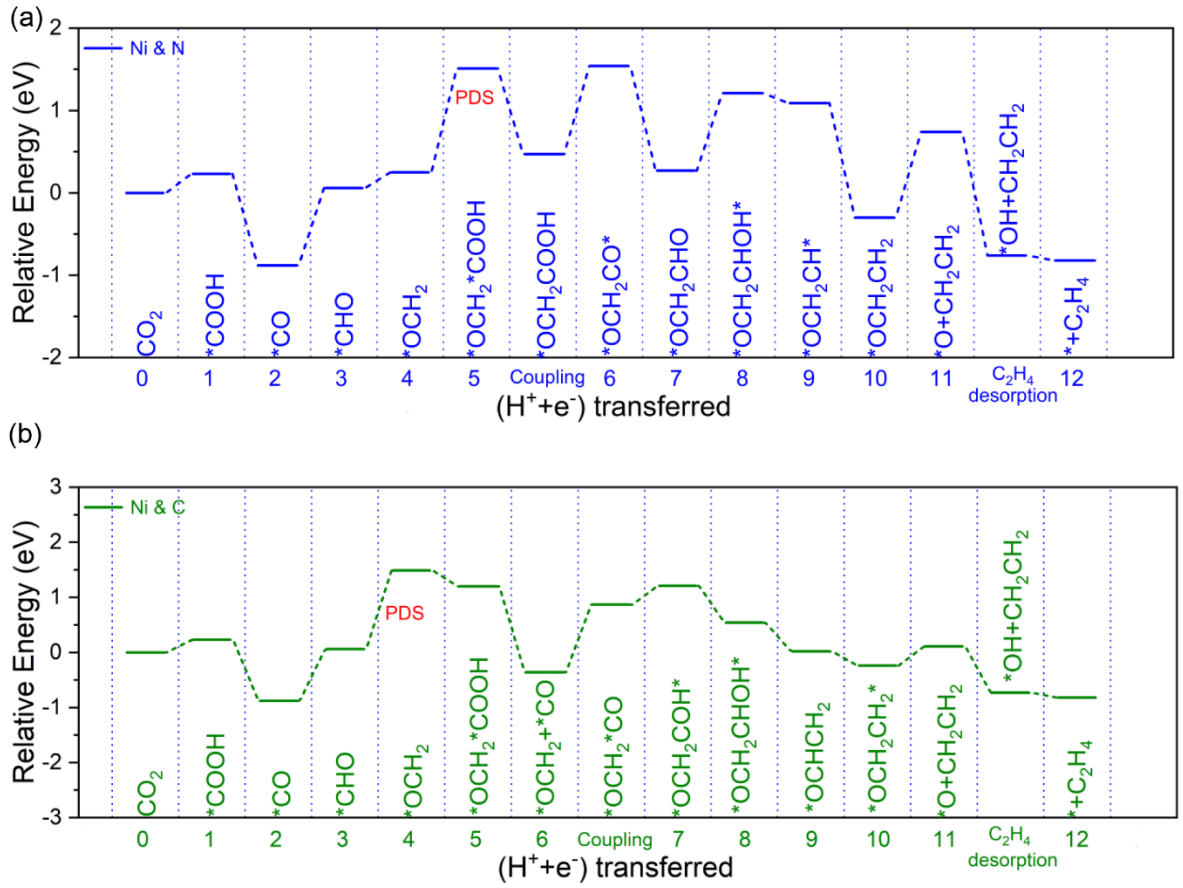


**Figure S4** Free energy diagram of $CO_2$ reduction to $C_2H_4$ on Ni-$C_3N_4$, using (a) Ni &N and (b) Ni & C as active sites.

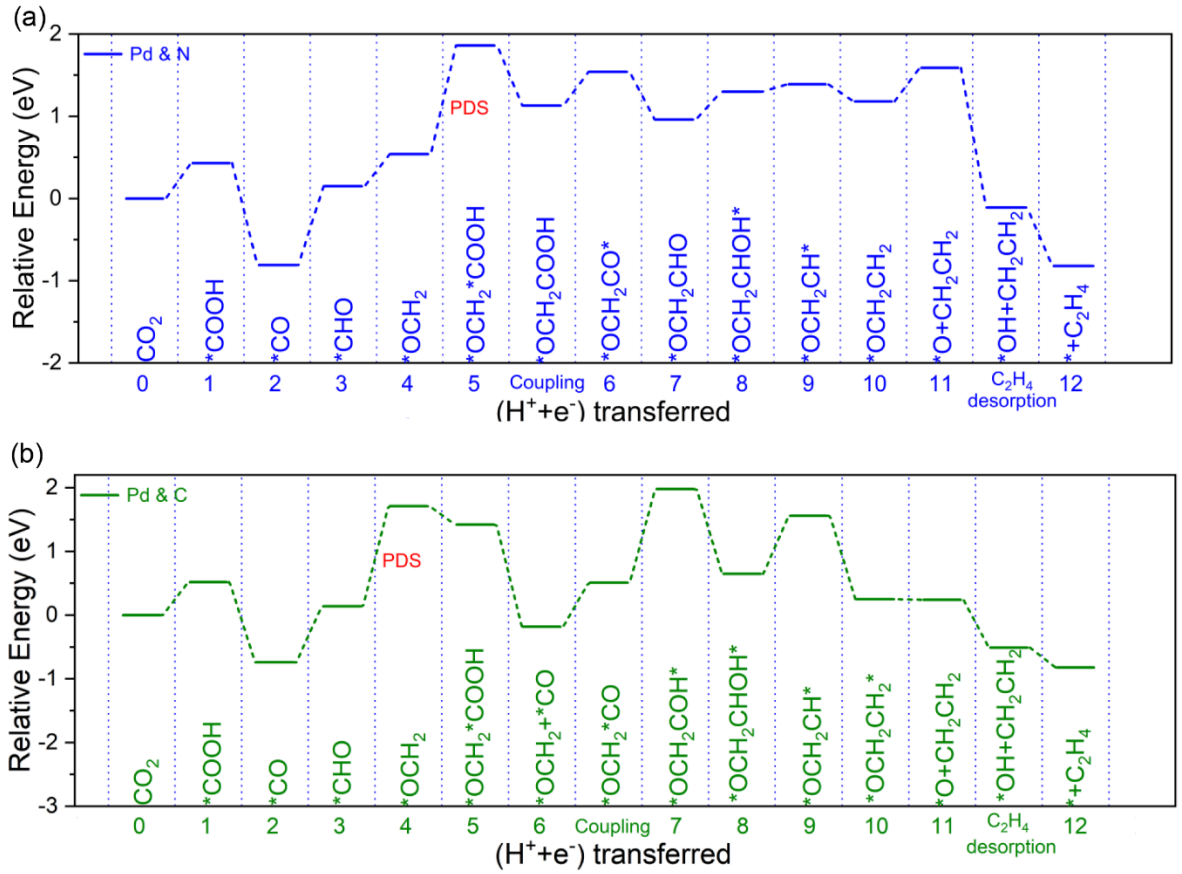


**Figure S5** Free energy diagram of $CO_2$ reduction to $C_2H_4$ on Pd-$C_3N_4$, using (a) Pd &N and (b) Pd & C as active sites.

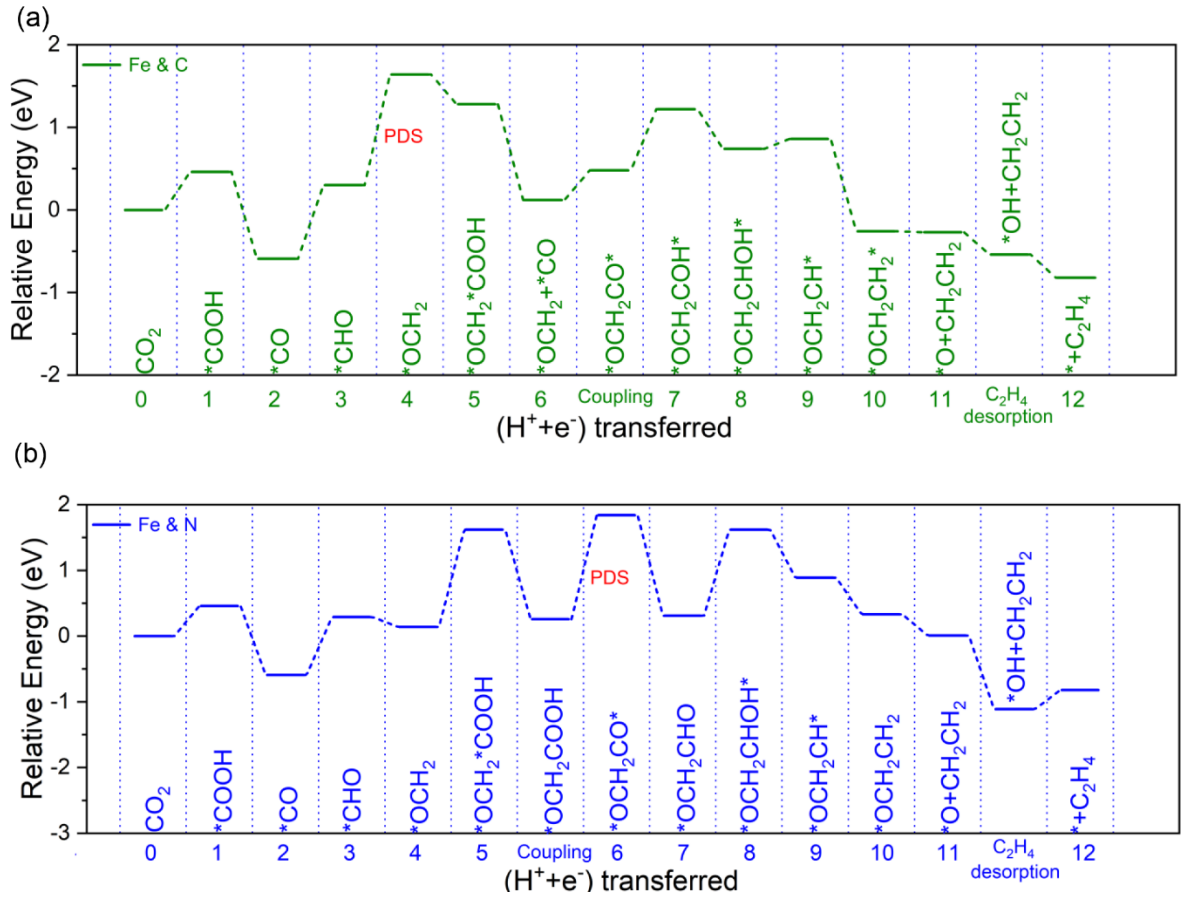


**Figure S6** Free energy diagram of $CO_2$ reduction to $C_2H_4$ on Fe-$C_3N_4$, using (a) Fe &C and (b) Fe & N as active sites.

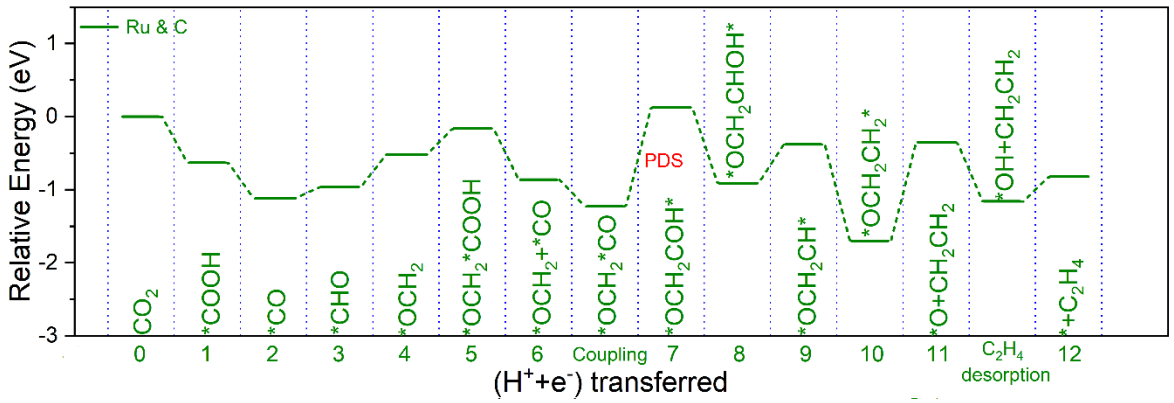


**Figure S7** Free energy diagram of $CO_2$ reduction to $C_2H_4$ on Ru-$C_3N_4$, using Ru and C as active sites.

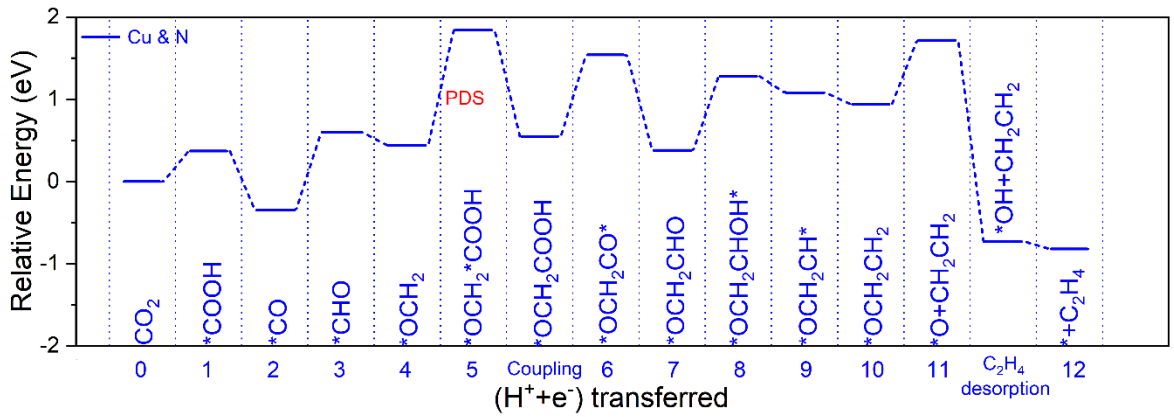


**Figure S8** Free energy diagram of $CO_2$ reduction to $C_2H_4$ on Cu-$C_3N_4$, using Cu and N as active sites.

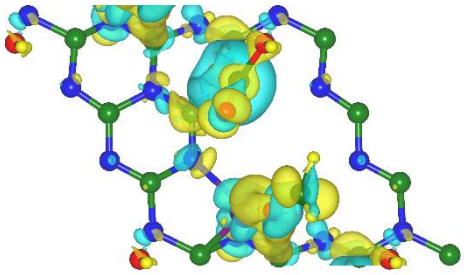

**Figure S9** The electron density difference for the intermediates (*$OCH_2$+*COOH) adsorbed on the surface of Ru-$C_3N_4$ in the structure of Ru*$OCH_2$+N*COOH. Yellow represents electron accumulation, and cyan denotes electron depletion. Color code: C green, N blue, H yellow, O red, Ru purple. Isosurface value is $4\times10^{-3}$ e/$Bohr^3$.

**Table S1.** Computed gas phase properties in eV.

| Gas molecule | ZPE | $\int C_p dT$ | $-TS$ |
|---|---|---|---|
| CO(g) | 0.14 | 0.10 | -0.61 |
| $CO_2$(g) | 0.31 | 0.11 | -0.66 |
| HCHO(g) | 0.72 | 0.17 | -0.68 |
| $C_2H_4$(g) | 1.37 | 0.11 | -0.17 |
| $H_2$(g) | 0.27 | 0.10 | -0.20 |
| $H_2O$(g) | 0.58 | 0.10 | -0.25 |

**Table S2.** The free energy change for every step after ($H^+$+$e^-$) transfer for Ru-$C_3N_4$.

| ($H^+$+$e^-$) transfer | status | Free energy change (eV) |
|---|---|---|
| 0(Initial Stage) | *+2$CO_2$+12($H^+$+$e^-$) | |
| 1 | Ru*COOH+$CO_2$+11($H^+$+$e^-$) | -0.63 |
| 2 | Ru*CO+$CO_2$+10($H^+$+$e^-$) +$H_2O$ | -0.92 |
| 3 | Ru*CHO+$CO_2$+9($H^+$+$e^-$) +$H_2O$ | 0.59 |
| 4 | Ru*$OCH_2$+$CO_2$+8($H^+$+$e^-$) +$H_2O$ | 0.90 |
| Coupling | Ru*$OCH_2$+N*COOH+7($H^+$+$e^-$) +$H_2O$ | 0.88 |
| 5 | Ru*$OCH_2$COOH+7($H^+$+$e^-$) +$H_2O$ | -1.36 |
| 6 | Ru*$OCH_2$CO*N+6($H^+$+$e^-$) +2$H_2O$ | 0.85 |
| 7 | Ru*$OCH_2$CHO+5($H^+$+$e^-$) +2$H_2O$ | -0.26 |
| 8 | Ru*$OCH_2$CHOH*N+4($H^+$+$e^-$) +2$H_2O$ | -0.01 |
| 9 | Ru*$OCH_2$CH*N+3($H^+$+$e^-$) +3$H_2O$ | 0.31 |
| 10 | Ru*$OCH_2CH_2$+2($H^+$+$e^-$) +3$H_2O$ | -0.23 |
| $C_2H_4$ desorption | Ru*O+$C_2H_4$+2($H^+$+$e^-$) +3$H_2O$ | -1.07 |
| 11 | Ru*OH+$C_2H_4$+($H^+$+$e^-$) +3$H_2O$ | -0.29 |
| 12(Final Stage) | *+$C_2H_4$+4$H_2O$ | 0.41 |

**Table S3.** The free energy change for every step after ($H^+$+$e^-$) transfer for Cu-$C_3N_4$.

| ($H^+$+$e^-$) transfer | status | Free energy change (eV) |
|---|---|---|
| 0(Initial Stage) | *+2$CO_2$+12($H^+$+$e^-$) | |
| 1 | Cu*COOH+$CO_2$+11($H^+$+$e^-$) | 0.37 |
| 2 | Cu*CO+$CO_2$+10($H^+$+$e^-$) +$H_2O$ | -0.88 |
| 3 | Cu*CHO+$CO_2$+9($H^+$+$e^-$) +$H_2O$ | 1.01 |
| 4 | C*$OCH_2$+$CO_2$+8($H^+$+$e^-$) +$H_2O$ | 1.02 |
| 5 | C*$OCH_2$*Cu*COOH+7($H^+$+$e^-$) +$H_2O$ | -0.33 |
| 6 | C*$OCH_2$+Cu*CO+6($H^+$+$e^-$) +2$H_2O$ | 0.21 |
| Coupling | C*OCH2*Cu*CO+6($H^+$+$e^-$) +2$H_2O$ | 0.01 |
| 7 | C*$OCH_2$COH*Cu+5($H^+$+$e^-$) +2$H_2O$ | 0.09 |
| 8 | C*$OCH_2$CHOH*Cu+4($H^+$+$e^-$) +2$H_2O$ | -0.10 |
| 9 | C*$OCH_2$CH*Cu+3($H^+$+$e^-$) +3$H_2O$ | 0.04 |
| 10 | C*$OCH_2CH_2$*Cu+2($H^+$+$e^-$) +3$H_2O$ | -0.99 |
| $C_2H_4$ desorption | C*O+$C_2H_4$+2($H^+$+$e^-$) +3$H_2O$ | 0.04 |
| 11 | C*OH+$C_2H_4$+($H^+$+$e^-$) +3$H_2O$ | -1.21 |
| 12(Final Stage) | *+$C_2H_4$+4$H_2O$ | -0.11 |

**Table S4.** Structures of M@$C_3N_4$ and the key reaction intermediates.

| Metal Center | SACs | M*COOH | M*CO | M*CHO | C*OCH2 | M*OCH2 | N*COOH |
|---|---|---|---|---|---|---|---|
| Pt | 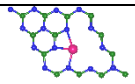 | 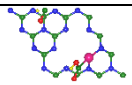 | 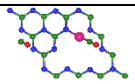 | 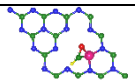 | 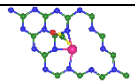 | 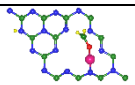 | 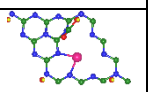 |
| Ru | 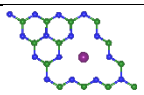 | 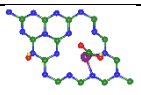 | 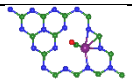 | 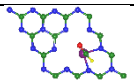 | 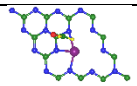 | 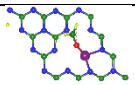 | 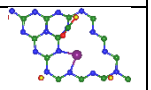 |
| Co | 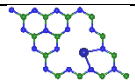 | 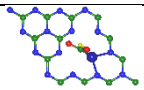 | 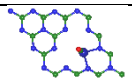 | 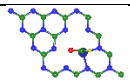 | 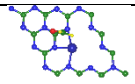 | 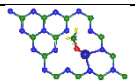 | 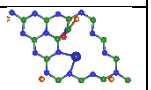 |
| Ni | 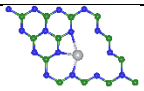 | 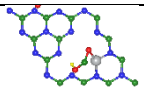 | 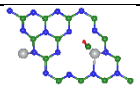 | 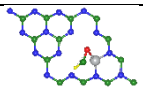 | 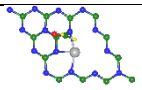 | 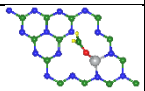 | 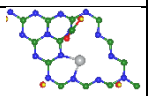 |
| Pd | 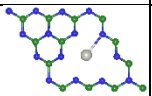 | 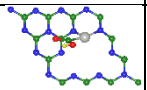 | 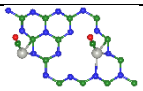 | 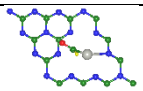 | 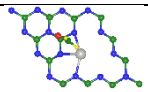 | 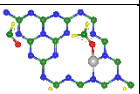 | 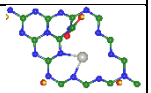 |
| Fe | 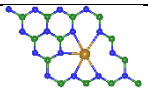 | 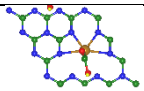 | 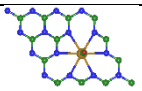 | 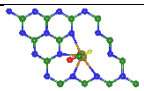 | 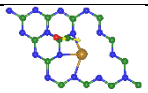 | 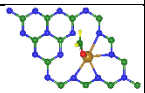 | 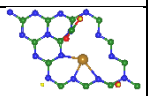 |
| Cu | 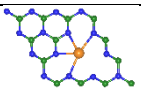 | 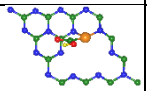 | 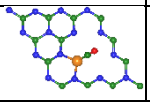 | 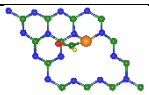 | 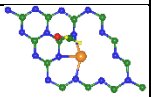 | 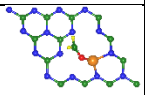 | 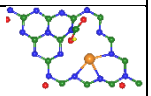 |

**Table S5.** Computed intermediates properties in eV.

| Intermediate | ZPE | $\int C_p dT$ | $-TS$ |
|---|---|---|---|
| Pt | | | |
| Pt*COOH | -149.40 | 0.20 | -03.20 |
| Pt*CO | -139.41 | 0.17 | -0.17 |
| Pt*CHO | -142.16 | 0.17 | -0.14 |
| C*$OCH_2$ | -143.56 | 0.19 | -0.19 |
| Pt*$OCH_2$ | -145.14 | 0.19 | -0.18 |
| N*COOH | -147.71 | 0.19 | -0.19 |
| Ru | | | |
| Ru*COOH | -152.07 | 0.21 | -0.22 |
| Ru*CO | -141.35 | 0.17 | -0.16 |
| Ru*CHO | -144.86 | 0.18 | -0.18 |
| C*$OCH_2$ | -146.51 | 0.19 | -0.18 |
| Ru*$OCH_2$ | -147.68 | 0.19 | -0.17 |
| N*COOH | -150.59 | 0.19 | -0.19 |
| Co | | | |
| Co*COOH | -150.58 | 0.19 | -0.22 |
| Co*CO | -140.54 | 0.17 | -0.18 |
| Co*CHO | -142.81 | 0.19 | -0.20 |
| C*$OCH_2$ | -145.54 | 0.20 | -0.17 |
| Co*$OCH_2$ | -146.18 | 0.20 | -0.22 |
| N*COOH | -149.59 | 0.19 | -0.19 |
| Ni | | | |
| Ni*COOH | -149.63 | 0.20 | -0.20 |
| Ni*CO | -139.45 | 0.17 | -0.16 |
| Ni*CHO | -142.25 | 0.18 | -0.17 |
| C*$OCH_2$ | -144.50 | 0.19 | -0.16 |
| Ni*$OCH_2$ | -145.78 | 0.18 | -0.15 |
| N*COOH | -148.53 | 0.19 | -0.19 |
| Pd | | | |
| Pd*COOH | -148.78 | 0.21 | -0.21 |
| Pd*CO | -138.82 | 0.17 | -0.16 |
| Pd*CHO | -141.61 | 0.18 | -0.15 |
| C*$OCH_2$ | -143.72 | 0.19 | -0.17 |
| Pd*$OCH_2$ | -144.84 | 0.20 | -0.26 |
| N*COOH | -148.06 | 0.19 | -0.21 |
| Fe | | | |
| Fe*COOH | -152.04 | 0.22 | -0.26 |
| Fe*CO | -141.73 | 0.17 | -0.16 |
| Fe*CHO | -144.69 | 0.19 | -0.18 |
| C*$OCH_2$ | -147.04 | 0.19 | -0.17 |
| Fe*$OCH_2$ | -148.53 | 0.20 | -0.22 |
| N*COOH | -150.91 | 0.19 | -0.19 |
| Cu | | | |
| Cu*COOH | -147.97 | 0.20 | -0.22 |
| Cu*CO | -137.49 | 0.17 | -0.16 |
| Cu*CHO | -140.20 | 0.18 | -0.16 |
| C*$OCH_2$ | -142.98 | 0.19 | -0.16 |
| Cu*$OCH_2$ | -144.08 | 0.20 | -0.18 |
| N*COOH | -146.95 | 0.19 | -0.19 |

# Chapter 5: Conclusions and Perspectives

## 5.1 Conclusions

This thesis focuses on designing electrocatalysts for $CO_2$ reduction to $C_2$ products by molecular modelling and gaining insights into the reaction mechanisms of these processes. In this thesis, various single metal atom supported on graphitic carbon nitride (M-$C_3N_4$) are studied as catalysts for $CO_2$ reduction to $C_2H_4$ via DFT calculations. In Chapter 3, objective 1.2.1 and 1.2.2 for this thesis are achieved. The whole reaction networks on this asymmetric framework of Cu-$C_3N_4$ were built up systematically and in total 17 pathways were established on the three active sites of Cu-$C_3N_4$ (Cu, C, and N). Two reaction mechanisms were found for Cu-$C_3N_4$, either using Cu/C or Cu/N as active sites. The most probable reaction pathway toward $C_2H_4$ production is 1.08 eV at open circuit conditions, which is benefited by the synergetic effect of both Cu and C active sites. The carbon atom provides a perfect settling center for the first $CO_2$ after reduction by Cu, leaving Cu atom free for the reduction of the second $CO_2$. In Chapter 4, objective 1.2.1 and 1.2.3 for this thesis are achieved. 14 different metals were chosen as metal centers for single atom metal supported on carbon nitride (M-$C_3N_4$) as $CO_2$ reduction electrocatalysts. Seven out of 14 metal centers were predicted to generate beyond CO product based on the analysis of bi-descriptors, the adsorption energies of CO* on the metal site and that of H* on the nitrogen site. The $CO_2$ reduction activity for these metal centers was studied by establishing reaction pathways towards ethylene through M/N or M/C. Ru has the best performance (the limiting potential is - 0.90 V) by taking M/N as active sites. Moreover, a dual volcano-shaped plot is built up based on the CO adsorption energies on metal sites, which can be used to indicate whether M/C or M/N shows better performance for a specific metal center.

In summary, the structure of metal supported on carbon nitride as electrocatalyst for $CO_2$ reduction were studied systematically and all of the objectives are achieved. The understanding of the reaction mechanisms, synergetic effect between metals and supported framework, and

reaction activity for reduction to $C_2H_4$ helps guide the design of other electrocatalyst materials involving dual active sites.

### 5.2 Perspectives

Although through molecular modelling, the structure of M-$C_3N_4$ has been studied in detail as a possible electrocatalyst for $CO_2$ reduction to beyond CO product, additional actions are still required to improve the performance of electrocatalysts with dual active sites. These include:

1. There lacks $C_2$ product selectivity analysis for $CO_2$ reduction on M-$C_3N_4$, which needs to be considered in the future to identify the possibility leading to high selectivity. Hence, it can further guide the design of dual active sites catalysts with high selectivity to $C_2$ products.
2. Current computational results on M-$C_3N_4$ have not been validated through experiments. Ru-$C_3N_4$ is expected to have the best performance in producing $C_2H_4$. Therefore, further experiments can be conducted base on it in order to verify the reaction mechanisms.
3. M-$C_3N_4$ as an electrocatalyst for $CO_2$RR is still not a satisfactory material for commercial usage. Current reaction mechanisms based on the dual sites in M-$C_3N_4$ may be extended to other graphene supported materials in order to find out the suitable candidates for commercial usage.